GLASILO SLOVENSKIH TEKSTILCEV • SLOVENE JOURNAL FOR TEXTILE AND CLOTHING TECHNOLOGY, DESIGN AND MARKETING

tekstilec

2/2020 • vol. 63 • 77–162
ISSN 0351-3386 (tiskano/printed)
ISSN 2350 - 3696 (elektronsko/online)
UDK 677 + 687 (05)

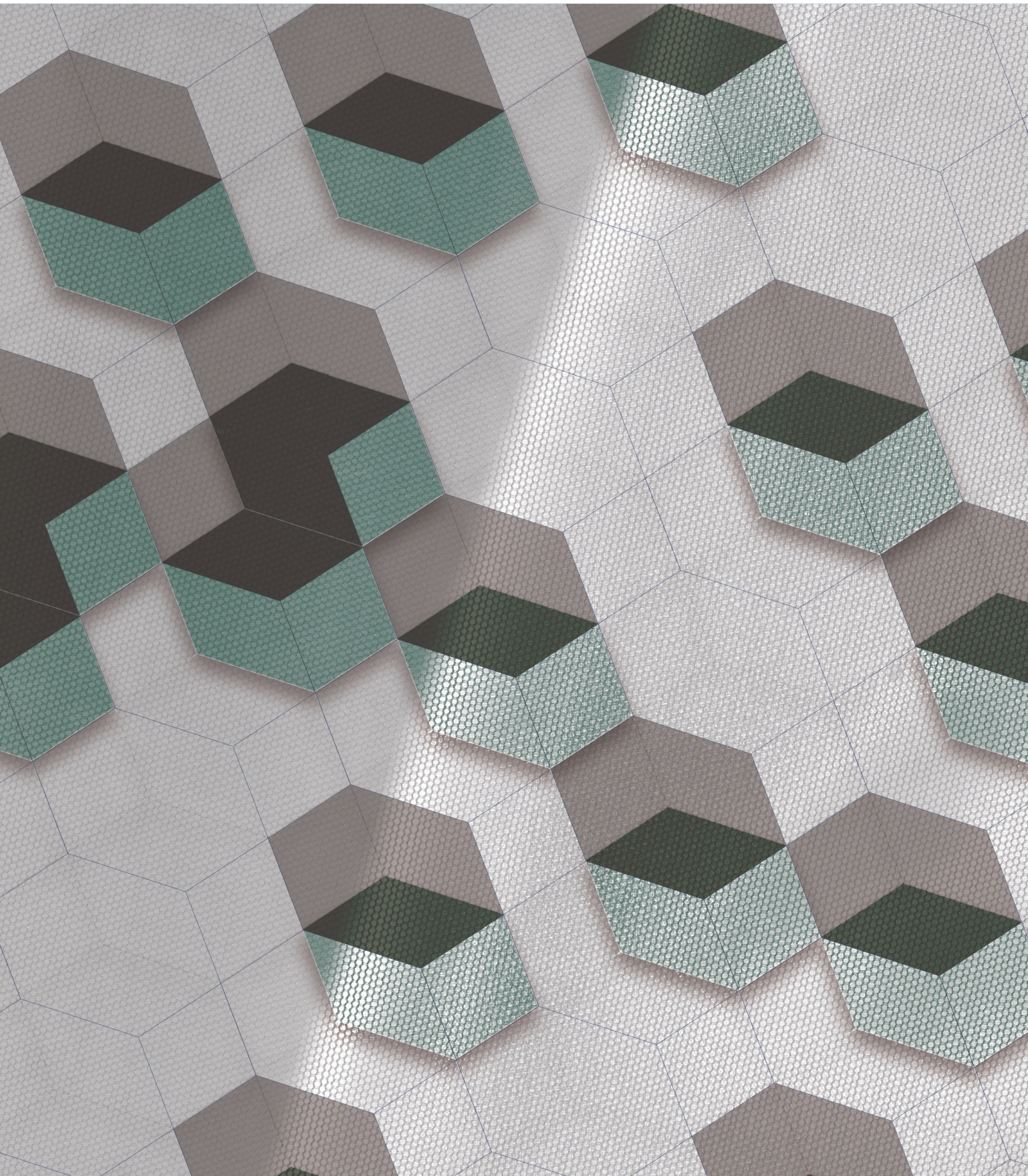

http://www.tekstilec.si

tekstilec (ISSN: 0351-3386 tiskano, 2350-3696 elektronsko) je znanstvena revija, ki podaja temeljne in aplikativne znanstvene informacije v fizikalni, kemijski in tehnološki znanosti, vezani na tekstilno in oblačilno tehnologijo, oblikovanje in trženje tekstilij in oblačil. V prilogah so v slovenskem jeziku objavljeni strokovni članki in prispevki o novostih v tekstilni tehnologiji iz Slovenije in sveta, prispevki s področja oblikovanja tekstilij in oblačil, informacije o raziskovalnih projektih ipd.

tekstilec *(ISSN: 0351-3386 printed, 2350-3696 online) the scientific journal gives fundamental and applied scientific information in the physical, chemical and engineering sciences related to the textile and clothing industry, design and marketing. In the appendices written in Slovene language, are published technical and short articles about the textile-technology novelties from Slovenia and the world, articles on textile and clothing design, information about research projects etc.*

Dosegljivo na svetovnem spletu/*Available Online at*
www.tekstilec.si

Tekstilec je indeksiran v naslednjih bazah/*Tekstilec is indexed in*
Emerging Sources Citation Index – ESCI/Clarivate Analytics
SCOPUS/Elsevier (2018: Q3, SJR 0.16, Cite Score 0.45, SNIP 0.612 – v sodelovanju z/*in cooperation with* Leiden University's Center for Science & Technology Studies)
Ei Compendex
DOAJ
WTI Frankfurt/TEMA® Technology and Management/TOGA® Textile Database
World Textiles/EBSCO Information Services
Textile Technology Complete/EBSCO Information Services
Textile Technology Index/EBSCO Information Services
Chemical Abstracts/ACS
ULRICHWEB – global serials directory
LIBRARY OF THE TECHNICAL UNIVERSITY OF LODZ
dLIB
SICRIS: 1A3 (Z, A', A1/2)

tekstilec

Ustanovitelja / *Founded by*
• Zveza inženirjev in tehnikov tekstilcev Slovenije /
Association of Slovene Textile Engineers and Technicians
• Gospodarska zbornica Slovenije – Združenje za tekstilno,
oblačilno in usnjarsko predelovalno industrijo /
Chamber of Commerce and Industry of Slovenia – Textiles, Clothing and Leather Processing Association

Revijo sofinancirajo / *Journal is Financially Supported*
• Univerza v Ljubljani, Naravoslovnotehniška fakulteta / *University of Ljubljana, Faculty of Natural Sciences and Engineering*
• Univerza v Mariboru, Fakulteta za strojništvo /
University of Maribor, Faculty for Mechanical Engineering
• Javna agencija za raziskovalno dejavnost Republike Slovenije /
Slovenian Research Agency

Izdajatelj / *Publisher*
Univerza v Ljubljani, Naravoslovnotehniška fakulteta /
University of Ljubljana, Faculty of Natural Sciences and Engineering

Sponzor / *Sponsor*
Predilnica Litija, d. o. o.

Naslov uredništva/*Editorial Office Address*
Uredništvo Tekstilec, Snežniška 5, SI–1000 Ljubljana
Tel./*Tel.*: + 386 1 200 32 00, +386 1 200 32 24
Faks/*Fax*: + 386 1 200 32 70
E–pošta/*E–mail*: tekstilec@ntf.uni–lj.si
Spletni naslov/*Internet page*: http://www.tekstilec.si

Lektor za slovenščino / *Slovenian Language Editor* Barbara Luštek Preskar
Lektor za angleščino / *English Language Editor* Barbara Luštek Preskar, Tina Kočevar Donkov, Glen David Champaigne

Oblikovanje platnice / *Design of the Cover* Tanja Nuša Kočevar
Oblikovanje / *Design* Vilma Zupan
Oblikovanje spletnih strani / *Website Design* Jure Ahtik

Tisk / *Printed by* PRIMITUS, d. o. o.

Revija Tekstilec izhaja štirikrat letno / *Journal Tekstilec appears quarterly*
Revija je pri Ministrstvu za kulturo vpisana v razvid medijev pod številko 583.
Letna naročnina za člane Društev inženirjev in tehnikov tekstilcev je vključena v članarino.
Letna naročnina za posameznike 38 € za študente 22 €
za mala podjetja 90 € za velika podjetja 180 €
za tujino 110 €
Cena posamezne številke 10 €

Na podlagi Zakona o davku na dodano vrednost sodi revija Tekstilec med proizvode, od katerih se obračunava DDV po stopnji 5 %.

Transakcijski račun 01100–6030708186
Bank Account No. SI56 01100–6030708186
Nova Ljubljanska banka d.d.,
Trg Republike 2, SI–1000 Ljubljana,
Slovenija, SWIFT Code: LJBA SI 2X.

tekstilec VOLUME 63 • TEKSTILEC 2 • 2020 ISSN 0351-3386 (tiskano/printed)
UDK 677 + 687 (05)

SCIENTIFIC ARTICLES/
Znanstveni članki

Ekrem Gulsevincler[1], Mustafa Resit Usal[2], Demet Yilmaz[3]
[1] Kastamonu University, Electric and Energy Department, Abana Sabahat Mesut Yilmaz Vocational School, 37970 Kastamonu, Turkey
[2] Suleyman Demirel University, Department of Mechanical Engineering, Faculty of Engineering, 32260 Isparta, Turkey
[3] Suleyman Demirel University, Department of Textile Engineering, Faculty of Engineering, 32260 Isparta, Turkey

Modular Jet-Ring Yarn Spinning System

Modularni sistem za izdelavo curkovne prstanske preje

Original scientific article/*Izvirni znanstveni članek*
Received/*Prispelo* 2-2020 • Accepted/*Sprejeto* 4-2020

Abstract

In this study, a modular nozzle design was developed in which the twist chamber diameter, injector diameter, injector angle and the number of injectors of the nozzle can be optionally changed without the need of conventional manufacturing methods. The developed modular nozzle was compared with conventional nozzles taking into account both experimental and numerical analysis results. Experimental performance tests were conducted on the yarn quality achieved using air twist, which is the subject of the application of the nozzle. In the experimental study, conventional nozzles with the same structural configurations were produced to determine modular nozzle performance. In all jet-ring yarn productions, the air pressure was set at two different values: 75 kPa and 125 kPa (gauge). Yarn hairiness, irregularity and imperfection tests were carried out using an Uster Tester 3. Tensile properties (percentage of elongation and tenacity measured as cN/tex) tests were carried out using an Uster Tensorapid. In the numerical analysis, an Ansys CFX 18.0 computational fluid dynamics program was used for both conventional nozzle and modular nozzle configurations. All parametric study configurations were set separately using an SST turbulence model. Comparing the flow parameters of yarn hairiness (CFD analysis), it was found that increasing vorticity or helicity real eigen values reduced yarn hairiness.
Keywords SST, swirling flow, swirl number, jet-ring, nozzle-ring, air nozzle

Izvleček

V študiji je bila razvita modularno zasnovana šoba za curkovno predenje prstanske preje, v kateri se lahko poljubno spreminjajo premer vijne komore, premer in kot injektorja. Število injektorjev v šobi se lahko spreminja brez potrebe po običajnih proizvodnih metodah. Razvita modularna šoba je primerjana z običajnimi šobami z upoštevanjem rezultatov eksperimentalne in numerične analize. Izvedeni so bili eksperimentalni preizkusi kakovosti preje, vitih z uporabo modularno zasnovane šobe. Za določitev uporabnosti modularne šobe so bile izdelane običajne šobe z enakimi strukturnimi konfiguracijami. V vseh primerih izdelave curkovne prstanske preje sta bili uporabljeni dve vrednosti zračnega tlaka, in sicer 75 kPa ter 125 kPa. Na Uster Testerju 3 so bile izvedene meritve kosmatosti in neenakomernosti preje ter količine napak v preji. Natezne lastnosti (pretržna napetost in pretržni raztezek) so bile določene na aparatu Uster Tensorapid. Za numerično analizo običajne konfiguracije šobe in modularne šobe je bil uporabljen računalniški program za računalniško dinamiko tekočin, Ansys CFX 18.0. Vse študije konfiguracijskih parametrov so bile izvedene ločeno z uporabo SST turbulentnega modela. Z analizo CFD, ki omogoča računalniško primerjavo parametrov dinamike tekočin, je bilo ugotovljeno, da povečanje vrtinčenja ali vijačenja realno zmanjša vrednosti kosmatost preje.
Ključne besede: SST, vrtinčasti tok, vrtinčna številka, curek-prstan, obroč šobe, zračna šoba

Corresponding author/*Korespondenčna avtorica:*
Dr. Ekrem Gulsevincler
E-mail: egulsevincler@kastamonu.edu.tr
ORCID: 0000-0002-4787-6275

Tekstilec, 2020, ***63****(2), 80-93*
DOI: 10.14502/Tekstilec2020.63.80-93

1 Introduction

Swirling flows are found in many areas of our lives and engineering. 'Swirling flow' [1] is defined as the rotating helical flow and can be seen in natural events, e.g. tornadoes, hurricanes, water vents, etc. Another example of swirling flows are the air-jet nozzles used in the textile industry on spinning machines. Swirling air flow is produced in an air nozzle depending on nozzle geometry and compressed air [2, 3]. The helical rotating flow in turbulent jets results in an increase in jet growth, drift speed and the decay rate of the jet. These effects also increase when helical rotation density increases. Swirling flows depend on different parameters, most of which were formulated and found as a result of studies. The most important parameter is the swirling number (*Sn*). The integral definition of the swirling number is expressed as the ratio of the axial flux of the angular momentum to the axial momentum flux and radius multiplication [1].

$$S_n = \frac{Angular\ Momentum}{R \cdot Axial\ Momentum} = \frac{G_{Ang}}{RG_{Ax}} = \\ = \frac{\int_0^{2\pi}\int_0^R u_z u_\phi r^2 dr d\phi}{R\int_0^{2\pi}\int_0^R u_z^2 r dr d\phi} \quad (1)$$

where R represents the twisting chamber radius, u_z represents the axial velocity component, u_ϕ represents the tangential velocity component, and r and ϕ represent the radial and angular coordinates taken according to the main hole (twisting chamber) centre. Since these values cannot be known in advance, a geometric swirling number (S_g) can also be defined based on the ratio of mass flows in the twisting chamber and in the entrance cross-sectional areas. These values can also be defined in a geometric swirling number (S_g) based on the ratio of mass flows in the twisting chamber and in the air inlet entrance (injectors) cross-sectional areas, as it is not known before the CFD (computational fluid dynamics) analysis or experimental studies are performed [1].

$$S_g = \left(\frac{m_t}{m_T}\right)^2 \left(\frac{D_{tc}}{d}\right)^2 \frac{sin\theta}{N} \quad (2)$$

where m_t and m_T represent mass flows in the injectors (total) and in the test section (twisting chamber). According to equation 2, the geometric swirling number (i.e. the swirl density) depends on the diameter of the twist chamber D_{tc}, injector diameter d, injector angle θ and the number of injectors N [1].

1.1 CFD turbulence model used

The calculation of the turbulent helical rotating flow by computational fluid dynamics is the determining factor for the appropriate turbulence model. The swirling number is a decisive factor for the turbulence model of the turbulent helical rotating flow in the analysis of computational fluid dynamics. Literature suggests that if the swirling number is less than 0.5, there is a weak or medium swirling flow that is sufficient for the flow analysis, and the k-ε turbulence model can be used (with realisable k-ε, RNG k-ε selections). Guo [1] reported that the Reynolds Stress Model (RSM) is generally more reliable than two-equation models, but the RSM model needs a large memory and high processor time, and convergence is more difficult. As an alternative, the realisable k-ε turbulence model closes the turbulent Navier-Stokes equations. The realisable k-ε model is a revised k-ε turbulence model. Compared to the standard k-ε turbulence model, the realisable k-ε model exhibits superior performance for flows involving boundary layers, flow separations and rotation under strong reverse pressure gradients. In another turbulent swirling flow study, turbulence models were compared using a steady flow analysis, and an SST (Shear Stress Transport) turbulence model was found to be closest to the experimental study.

The SST includes a collation function to add a cross-diffusion term in the ω equation in the turbulence model and to ensure that model equations behave appropriately in the near-wall and far area regions [4].

The SST turbulence model basically has the same definition as the k-ω model [4–6]:

$$\frac{\partial}{\partial t}(\rho k) + \frac{\partial}{\partial x_i}(\rho k u_i) = \frac{\partial}{\partial x_j}\left(\Gamma k \frac{\partial k}{\partial x_j}\right) + G_k - Y_k + S_k \quad (3)$$

and

$$\frac{\partial}{\partial t}(\rho\omega) + \frac{\partial}{\partial x_i}(\rho\omega u_i) = \\ = \frac{\partial}{\partial x_j}\left(\Gamma\omega \frac{\partial \omega}{\partial x_j}\right) + G_\omega - Y_\omega + D_\omega + S_\omega \quad (4)$$

where G_k represents the production of turbulence kinetic energy due to average velocity gradients. G_ω represents the production of ω. Γ_k and Γ_ω represent the effective diffusivity of k and ω. Y_k and Y_ω represent the dissipation of k and ω owing to turbulence. D_ω is the cross-diffusion term formulised in equation 21. S_k and S_ω are user-defined resource terms [4–11].

1.2 Jet-ring (nozzle-ring) spinning system

This system is based on the placement of air nozzles used in the air-jet spinning system between the output system of the conventional ring spinning system and the yarn guide system, called jet-ring or nozzle-ring (Figure 1). Air is fed into the air nozzle used in the jet-ring system at a certain pressure value. Compressed air leads to a rotating air vortex in the nozzle. The air vortex ensures that the fibre ends that protrude outward from the yarn body are wound up in the yarn body, thereby reducing yarn hairiness [12]. In addition to low yarn hairiness, fabrics made from the aforementioned yarns are smoother and more resistant to pilling than the fabrics made from conventional ring spun yarns [3]. Air nozzles thus provide improved yarn properties and long-term advantages due to the improvements in fabric performance.

The first experiments with the jet-ring or nozzle-ring spinning system were carried out towards the end of the 1990s by Wang et al. [3]. Recently, many researchers have been working on yarn properties, in particular on the improvement of yarn hairiness over the use of air nozzles in a conventional ring spinning system [2, 3, 11–16].

Figure 1: Application of an air nozzle on a jet-ring spinning system

2 Materials and methods

2.1 Conventional jet-ring air nozzle

Conventional jet-ring (nozzle-ring) systems have a similar construction to compact-jet systems [2, 12], while siro-jet [13, 14] spinning systems are composed of three basic components as follows: compressed air, nozzle and yarn. Compressed air with a certain value from the air compressor is transported to the level and passed through the thread. The nozzle assembly (Figure 2c) has a very simple structure and consists of a nozzle housing (Figure 2a) and nozzle body (Figure 2b). The nozzle body part has a circular cross-section consisting of the main hole (twisting chamber) (1), injectors (2), connecting screw for the nozzle housing (3) and the nozzle outlet (4) (Figure 2b). The main hole extends from the nozzle entrance to the nozzle outlet. The injectors are positioned to be tangential to the twisting chamber. The nozzle housing conveys the compressed air from the air compressor to the twisting chamber section of the device via the injectors.

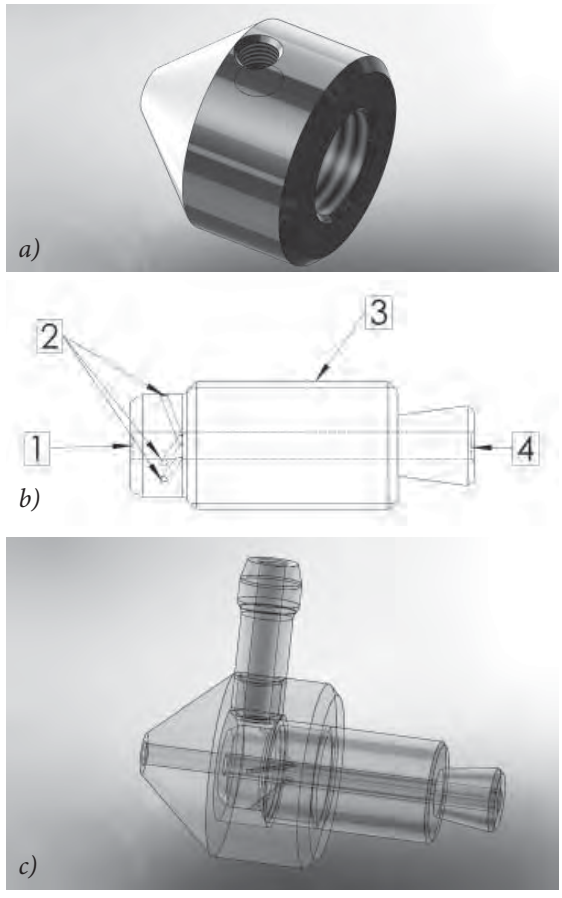

Figure 2: Nozzle (a) housing, (b) body and (c) assembly

Flow volume is illustrated in Figure 3. As shown in Figure 3, the design parameters of the air nozzles are composed of twist chamber diameter (D_{tc}), injector diameter (D_i) and injector angle (θ). The conventional jet-ring nozzle length is 27 mm, injector diameter is ϕ = 0.5 mm, injector quantity is 3 and twisting chamber diameter is ϕ = 3 mm. Those measurements were maintained for all samples.

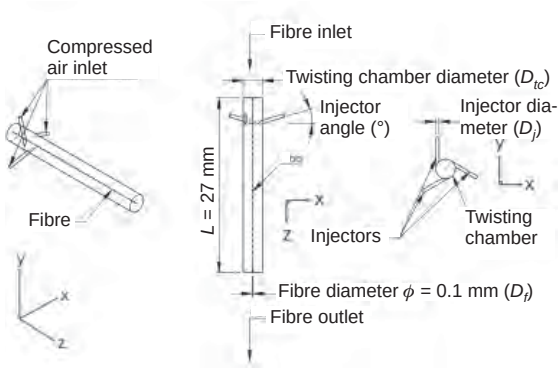

Figure 3: 3D model drawing of a conventional nozzle flow volume with 3 injectors

2.2 Modular jet-ring air nozzle

In the event of any structural parameter change in the conventional jet-ring air nozzle, a nozzle specific to that parameter must be produced and the existing nozzle removed and reassembled. This leads to costs for new nozzle parts, additional labour and labour costs. In the light of these shortcomings, a design was developed in this study, in which the twist chamber diameter, injector diameter, injector angle and number of nozzle injectors can be optionally changed without the need of conventional manufacturing methods. Angles can be adjusted for air nozzles with a high structural configuration type, instead of producing different nozzles. An air nozzle whose parts can be changed modularly and take on a new shape will make the spinning process much easier. Such a system consists of a modular air nozzle, a modular top and bottom twisting chamber, a modular injector, a tangential adjustment bracket and a modular body (Figure 4).

Figure 4: 3D model drawing of a modular jet-ring nozzle with 3 injectors

2.3 Experimental setup

In the experimental study, conventional nozzles with the same structural configurations were produced to determine modular nozzle performance. Conventional nozzles were prepared for the same conditions as the modular nozzle, while the yarn production system was prepared simultaneously. The structural configurations of the developed modular nozzle were adjusted to result in a twist chamber diameter ϕ = 3 mm and an injector diameter ϕ = 0.5 mm, with three circumferential injectors. The only difference was the nozzle length. Since the modular jet-ring nozzle consisted of a mechanism, it had a length of 81 mm, i.e. three times the length of the conventional nozzle. According to the study by Guo et al., when other structural parameters of the nozzle are kept constant, the effects of injector position and nozzle length, respectively, on flow velocities, the axial velocities near the injection location and tangential velocities in all flow-regions do not change significantly due to the same initial swirl intensity [1]. Because the nozzle length did not affect the swirling flow, we concluded that the difference in the length of conventional and modular nozzles would not pose a problem. The structural configurations of the developed modular nozzle were adjusted to result in a twist chamber diameter ϕ = 3 mm and an injector diameter ϕ = 0.5 mm,

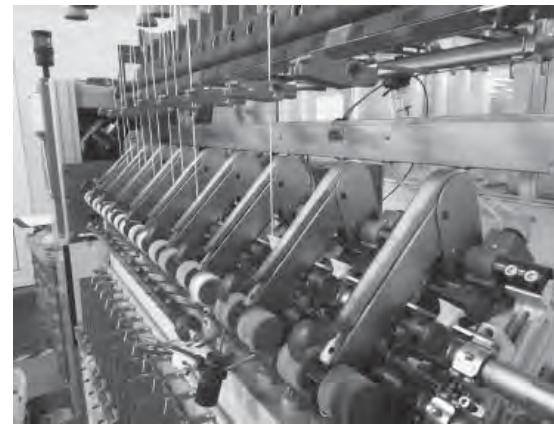

Figure 5: Jet-ring air nozzles mounted on conventional ring spinning machine

Table 1: Structural parameters of the conventional jet-ring nozzles and modular jet-ring nozzles

Nozzle type	Nozzle name	Twisting chamber diameter (mm)	Injector diameter (mm)	No. of injectors	Injector angle (°)
Conventional	C1	3	0.5	3	20
	C2	3	0.5	3	25
	C3	3	0.5	3	30
	C4	3	0.5	3	35
	C5	3	0.5	3	40
Modular	M1	3	0.5	3	20
	M2	3	0.5	3	25
	M3	3	0.5	3	30
	M4	3	0.5	3	35
	M5	3	0.5	3	40

with three circumferential injectors. The structural parameters of the jet-ring nozzles and modular jet-ring nozzle are shown in Table 1. Yarn production was performed on a Merlin SP43 conventional ring spinning machine made by the Pinter Group with a capacity of 16 spindles. The jet-ring air nozzles and modular jet-ring air nozzles mounted on the conventional ring spinning machine are illustrated in Figure 5.

2.4 Yarn production

One-hundred percent cotton yarns were produced in this experiment. We produced cotton jet-ring yarns of 19.6 tex (Table 2). In all the yarn productions, importance was given to working with the same spinning parameters, e.g., the same twist multiplier, draft, spindle speed and traveller type (Table 3). In all jet-ring yarn productions, air pressure was set at two different values: 75 kPa (gauge) and 125 kPa (gauge). Z-twisted carded cotton yarns were produced on a conventional ring spinning machine with and without nozzle placement. The false-twist air vortex direction of the jet-ring nozzles also resulted in a Z-twist.

Table 2: Fibre properties

Fibre properties	19.6 tex (Ne 30)
Staple length (mm)	30.53
Micronaire	4.52
U.I. (uniformity index)	85.7
Strength (cN/tex)	34.5
Breaking elongation (%)	6.4
SFI (short fibre index)	6.9
+b (yellowness)	7.9
Rd (reflectance degree)	72.1
CG (colour grade)	41–2
SCI (spinning count index)	160

Table 3: Spinning particulars

Parameters	19.6 tex
Roving count (tex)	472
Twist (1/m)	830
α_e	3.7
Mean spindle speed (rpm)	13.000
Take up speed (m/min)	15.7
Traveller type	SFB 2.8 PM udr
Traveller ISO No.	31.5–50
Ring diameter (mm)	38
Draft/Break draft	1.181
Total draft	50.4

2.5 Yarn tests

Yarn hairiness, irregularity and imperfections tests were carried out using an Uster Tester 3. Tensile properties (percentage of elongation and tenacity measured as cN/tex) tests were carried out using an Uster Tensorapid. The cops and bobbins of each system were fed in the same order to the testers. Yarn test details are given in Table 4. The tests were carried out under the same atmospheric conditions

Table 4: Test particulars for each yarn sample

Yarn properties	Test device	Test length (m)	Test number	Total length (m)
Yarn irregularity and imperfections	Uster Tester 3	400	1	400
Yarn hairiness	Uster Tester 3	400	1	400
Tensile properties	Uster Tensorapid	0.5	10	5

(75 ± 5% RH and 25 ± 2 °C), and we conditioned samples for a minimum of seventy-two hours before the tests. All the tests were carried out on the same testers and test results were analysed statistically to determine any significant differences.

2.6 CFD study

In this part of the study, which is the numerical analysis section, an Ansys CFX 18.0 computational fluid dynamics program was used for both conventional nozzle and modular nozzle configurations. In his study, Yilmaz noted that the number of elements of around 400,000, depending on the nozzle geometry, produced sufficiently accurate results [17]. Approximately 2,500,000 tetrahedral elements are used for any geometry (conventional and modular nozzle type) in the mesh prepared for a parametric study (the number of elements varies according to structural parameters). Using an ICEM CFD mesher in the Ansys CFX 18.0, the body of influence and the thin mesh of size 0.07 mm element were assigned to the cylindrical control volume,. For the twisting chamber boundary layer, the size of the element was assigned a face sizing of 0.1 mm. A detail view of the conventional nozzle mesh topology is given in Figure 6, while modular nozzle mesh topology is given in Figure 7. After the parameters and mesh topology were determined, using the Ansys CFX 18.0 software, the inlet boundary condition was defined as 225 kPa (absolute) total pressure from the air inlet (injectors) (125 kPa gauge). The relative pressure value was defined as "0 kPa" by selecting static pressure in the outlet boundary condition. The opening boundary condition was defined in the fibre inlet opening and, similar to the outlet boundary condition, the relative pressure value was defined as "0 kPa". Air at 25° was selected as fluid and the reference pressure was defined as 100 kPa. All parametric study configurations were solved separately using an SST turbulence model.

Figure 6: Conventional nozzle mesh topology

Figure 7: Modular nozzle mesh topology

3 Results and discussion

3.1 Yarn hairiness results

The effect of conventional jet-ring nozzles and modular jet-ring nozzles on yarn hairiness (*H*) is shown in Figure 8. According to the yarn hairiness graph, the yarn hairiness value in conventional jet-ring nozzles was measured at the lowest 35° injector angle configuration at both pressure values. The second yarn hairiness value is followed by a 40° injector

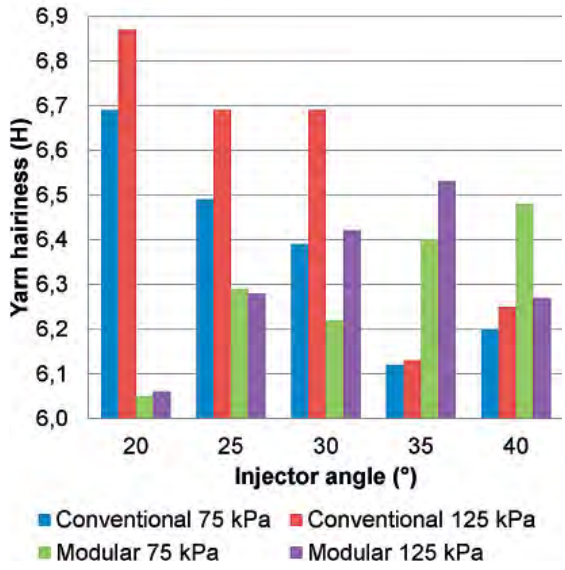

Figure 8: Comparison of conventional jet-ring nozzle and modular jet-ring nozzle yarn hairiness value

angle structural configuration. The worst yarn hairiness value in conventional jet-ring nozzles was obtained in the nozzle with a 20° injector angle configuration. Unlike conventional jet-ring nozzles, modular jet-ring nozzles achieved the best result when the yarn hairiness value was set to a 20° injector angle configuration. The worst yarn hairiness value achieved by modular jet-ring nozzles was obtained at a 35° injector angle configuration, which gives the best value for conventional jet-ring nozzles. When the hairiness value is considered, conventional jet-ring nozzles and modular jet-ring nozzles form an antithesis relative to one another in terms of the injector angle structural parameter. Comparing conventional jet-ring nozzles with modular jet-ring nozzles, it can be said that modular jet-ring nozzles are more successful in reducing hairiness. In modular and conventional nozzles with generally known structural configurations, an increase in pressure leads to an increase in yarn hairiness.

3.2 Yarn irregularity results

The effect of conventional jet-ring nozzles and modular jet-ring nozzles on yarn irregularity (% Cv m) is shown in Figure 9. An increase in pressure in conventional jet-ring nozzles with the tested structural configurations resulted in an increase in yarn irregularity. In modular jet-ring nozzles, an increase in pressure caused an increase in the yarn irregularity at the 20° and 35° injector angle values, while the other angle values showed an opposite decrease in yarn irregularity. In general, it is understood that the yarn irregularity values of the yarns produced in modular jet-ring nozzles are higher than those produced with conventional jet-ring nozzles.

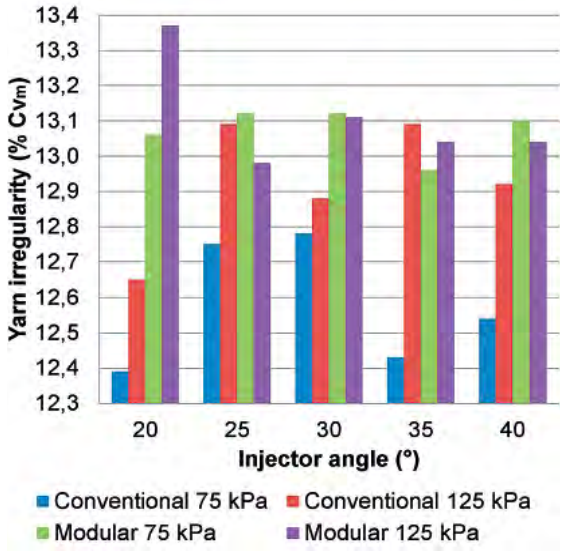

Figure 9: Comparison of conventional jet-ring nozzle and modular jet-ring nozzle yarn irregularity value

3.3 Yarn elongation results

The effect of conventional jet-ring nozzles and modular jet-ring nozzles on yarn elongation (%) is shown in Figure 10. In conventional jet-ring nozzles with the tested structural configurations, there is a significant decrease in yarn elongation, except in the context of a pressure increase at the 40° injector angle. In modular jet-ring nozzles, an increase in pressure increased the yarn elongation value at the 20° and 25° injector angle values and decreased at other injector angle values. In general, it is understood that the yarn elongation values of the yarns produced using modular jet-ring nozzles are lower than those produced using conventional jet-ring nozzles.

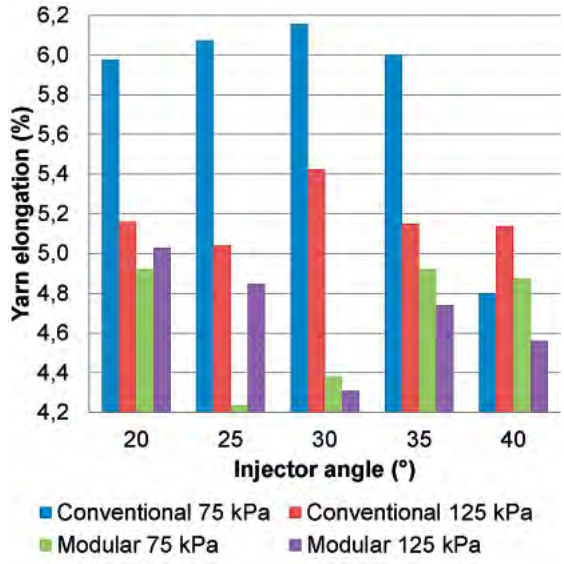

Figure 10: Comparison of conventional jet-ring nozzle and modular jet-ring nozzle yarn elongation value

3.4 Yarn tenacity results

The effect of conventional jet-ring nozzles and modular jet-ring nozzles on yarn tenacity (cN/tex) is shown in Figure 11. Increasing the pressure value in conventional jet-ring nozzles with the tested structural configurations showed a significant decrease in the yarn tenacity value as well as yarn elongation, except when the nozzle was set at a 40° injector angle. In

modular jet-ring nozzles, an increase in pressure increased yarn tenacity at 20°, 25° and 35° injector angle values and decreased at other injector angle values. When the air pressure was set to 75 kPa, the yarn tenacity values were higher in the yarns produced in conventional jet-ring nozzles, and higher in the yarns produced in modular jet-ring nozzles when it was set to 125 kPa. It was understood that modular jet-ring nozzles are less affected by a change in pressure in terms of the yarn tenacity value. This result showed that higher air pressure values can be achieved by using modular jet-ring nozzles without yarn breakage.

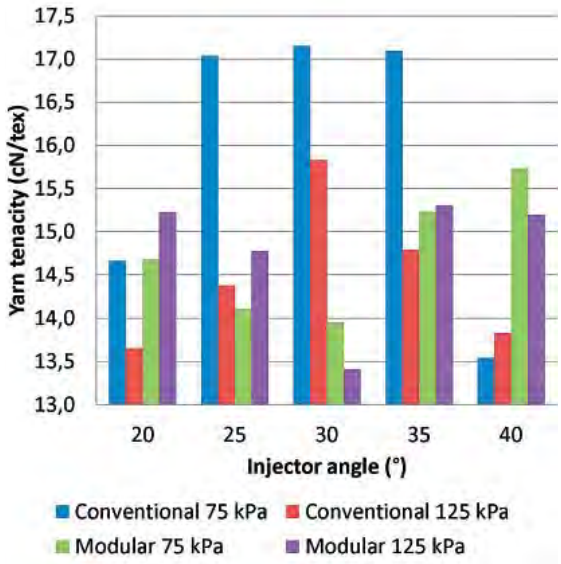

Figure 11: Comparison of conventional jet-ring nozzle and modular jet-ring nozzle yarn tenacity value

3.5 CFD result comparison

A CFD parameter comparison of conventional nozzles in five different injector angle configurations is given in Table 5, while a CFD parameter comparison of modular nozzles is given in Table 6. The swirl number, total pressure, flow pressure, Reynolds number, velocity, velocity in z axis, vorticity (curl of velocity) and helicity real eigen values of conventional and modular nozzles given in Table 5 and Table 6 are calculated in the plane where the injectors are opened to the twist chamber. The total pressure CFD result in the YZ plane of the five different conventional nozzle configurations given in Table 5 is shown in Figure 12. Similarly, the velocity CFD result is shown in Figure 13, the z-axis velocity CFD result is shown in Figure 14, the vorticity CFD result is shown in Figure 15, and the helicity real eigen CFD result is shown in Figure 17. Also, vorticity flow trajectories are shown in Figure 16 and helicity real eigen flow trajectories are shown in Figure 18. Similarly, the total pressure CFD result in the YZ plane of the five different modular nozzle configurations given in Table 6 is shown in Figure 19, while the velocity CFD result is shown in Figure 20, the z-axis velocity CFD result is shown in Figure 21, the vorticity CFD result is shown in Figure 22, and the helicity real eigen CFD result is shown in Figure 24. Also, vorticity flow trajectories are shown in Figure 23 and helicity real eigen flow trajectories are shown in Figure 25.

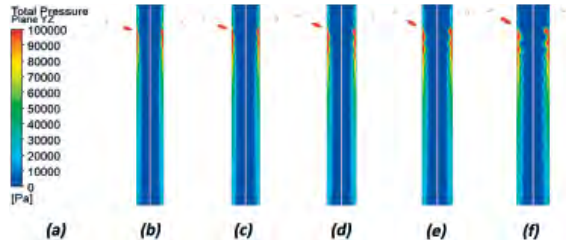

Figure 12: Conventional nozzle YZ plane total pressure CFD result: a) colour scale, b) injector angle 20°, c) injector angle 25°, d) injector angle 30°, e) injector angle 35°, f) injector angle 40°

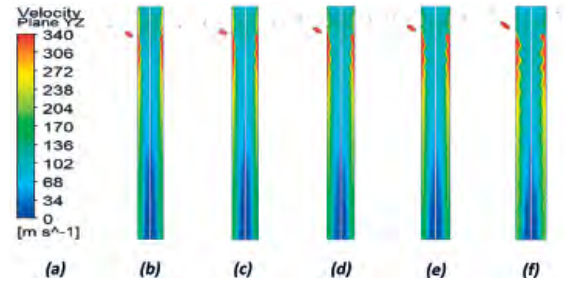

Figure 13: Conventional nozzle YZ plane velocity CFD result: a) colour scale, b) injector angle 20°, c) injector angle 25°, d) injector angle 30°, e) injector angle 35°, f) injector angle 40°

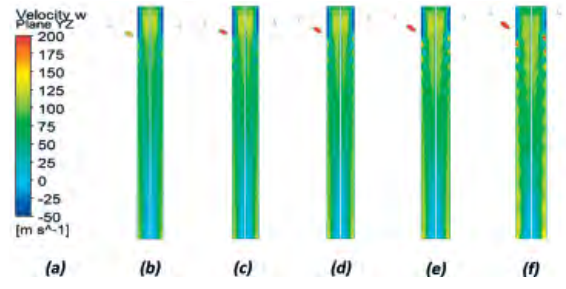

Figure 14: Conventional nozzle YZ plane velocity w (z axis) CFD result: a) colour scale, b) injector angle 20°, c) injector angle 25°, d) injector angle 30°, e) injector angle 35°, f) injector angle 40°

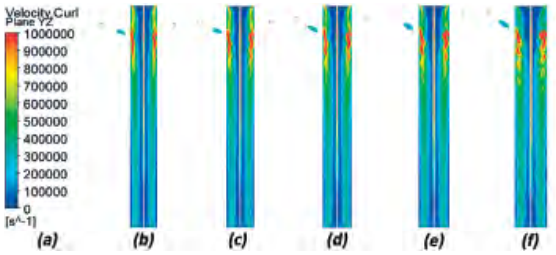

Figure 15: Conventional nozzle YZ plane vorticity (velocity curl) CFD result: a) colour scale, b) injector angle 20°, c) injector angle 25°, d) injector angle 30°, e) injector angle 35°, f) injector angle 40°

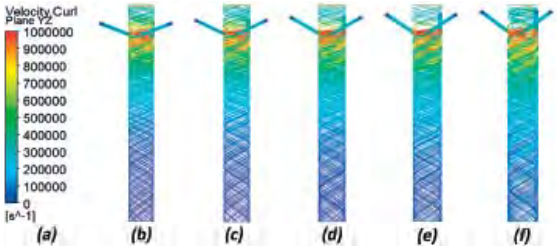

Figure 16: Conventional nozzle YZ plane vorticity (velocity curl) CFD result (flow trajectories): a) colour scale, b) injector angle 20°, c) injector angle 25°, d) injector angle 30°, e) injector angle 35°, f) injector angle 40°

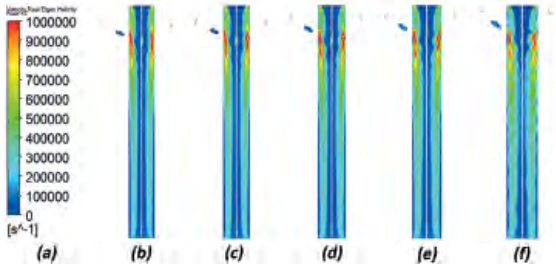

Figure 17: Conventional nozzle YZ plane helicity real eigen CFD result: a) colour scale, b) injector angle 20°, c) injector angle 25°, d) injector angle 30°, e) injector angle 35°, f) injector angle 40°

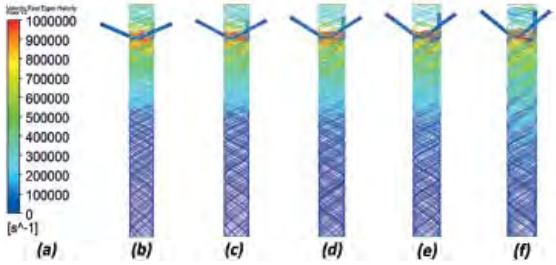

Figure 18: Conventional nozzle YZ plane helicity real eigen CFD result (flow trajectories): a) colour scale, b) injector angle 20°, c) injector angle 25°, d) injector angle 30°, e) injector angle 35°, f) injector angle 40°

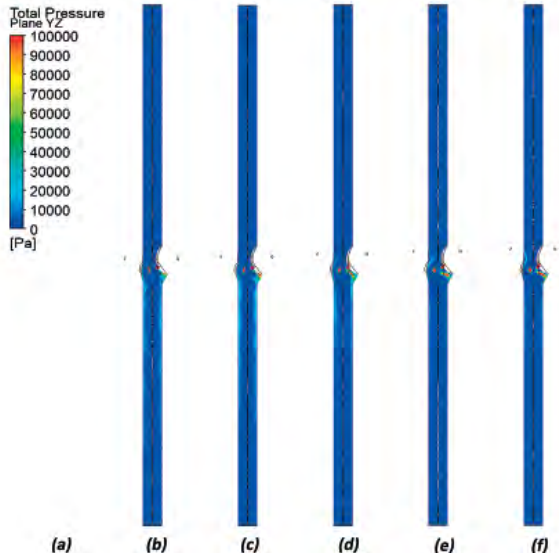

Figure 19: Modular nozzle YZ plane total pressure CFD result: a) colour scale, b) injector angle 20°, c) injector angle 25°, d) injector angle 30°, e) injector angle 35°, f) injector angle 40°

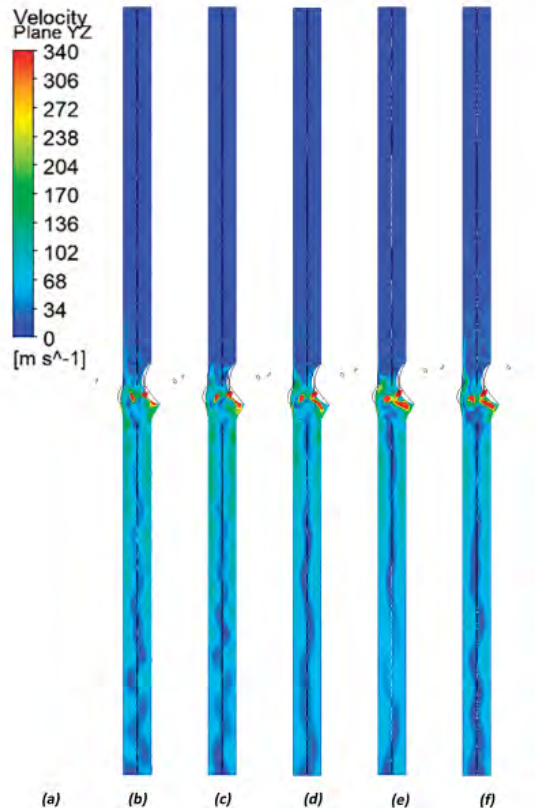

Figure 20: Modular nozzle YZ plane velocity CFD result: a) colour scale, b) injector angle 20°, c) injector angle 25°, d) injector angle 30°, e) injector angle 35°, f) injector angle 40°

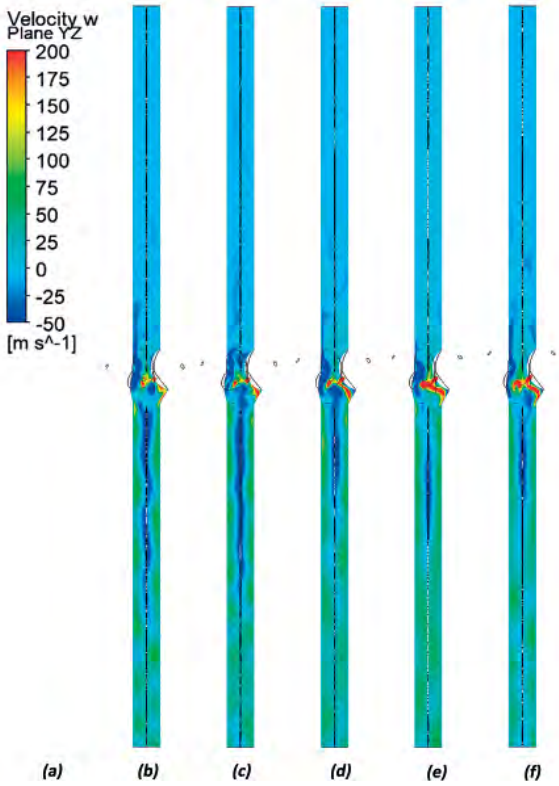

Figure 21: Modular nozzle YZ plane velocity w (z axis) CFD result: a) colour scale, b) injector angle 20°, c) injector angle 25°, d) injector angle 30°, e) injector angle 35°, f) injector angle 40°

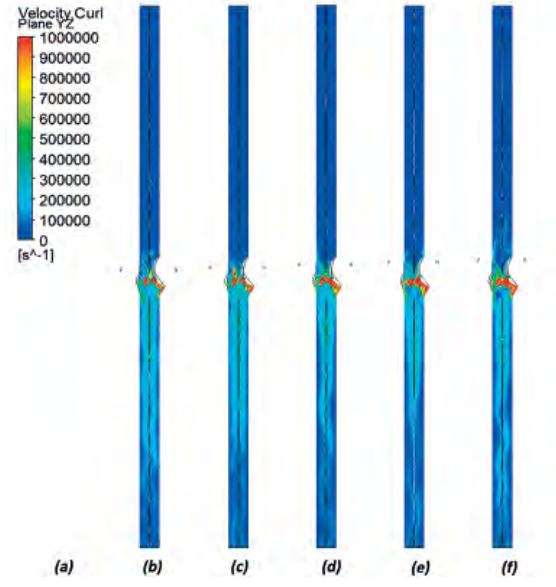

Figure 22: Modular nozzle YZ plane vorticity (velocity curl) CFD result: a) colour scale, b) injector angle 20°, c) injector angle 25°, d) injector angle 30°, e) injector angle 35°, f) injector angle 40°

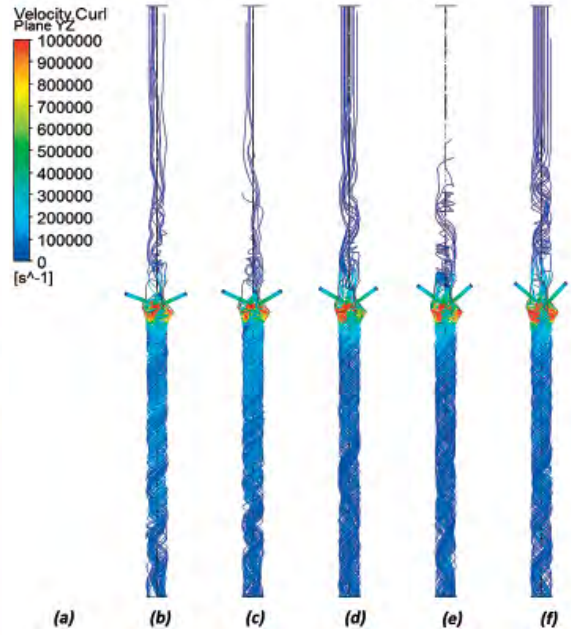

Figure 23: Modular nozzle YZ plane vorticity (velocity curl) CFD result: (flow trajectories) a) colour scale, b) injector angle 20°, c) injector angle 25°, d) injector angle 30°, e) injector angle 35°, f) injector angle 40°

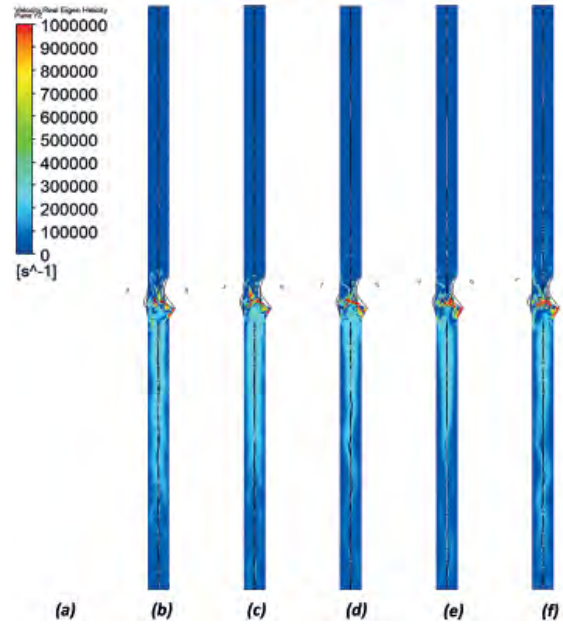

Figure 24: Modular nozzle YZ plane helicity real eigen CFD result: a) colour scale, b) injector angle 20°, c) injector angle 25°, d) injector angle 30°, e) injector angle 35°, f) injector angle 40°

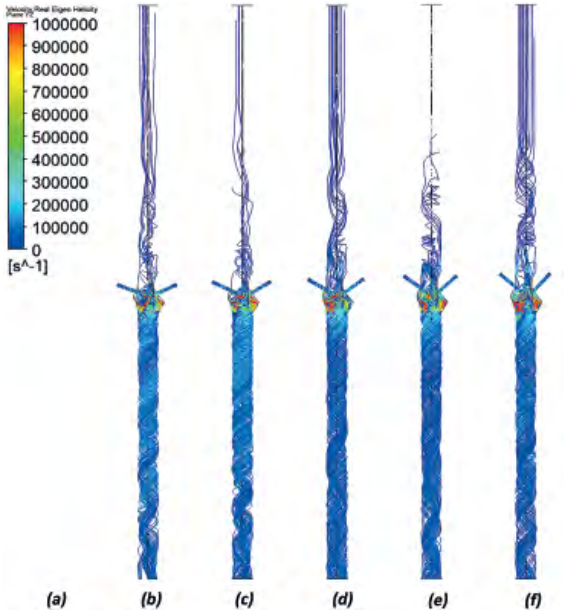

Figure 25: Modular nozzle YZ plane helicity real eigen CFD result (flow trajectories): a) colour scale, b) injector angle 20°, c) injector angle 25°, d) injector angle 30°, e) injector angle 35°, f) injector angle 40°

Considering injector air inlet mass flow values, the modular nozzles with the same structural configurations and analysed at the same pressure (225 kPa absolute) consumed an average of 11.5% more air than conventional nozzles. Considering fibre inlet mass flow values, an average suction in the fibre inlet opening of 0.77 times (minimum 0.65 – maximum 0.88) the injector air inlet mass flow value was achieved from the fibre inlets of conventional nozzles. In modular nozzles, this coefficient was -0.05. In other words, in modular nozzles of the same structural configurations, air cannot be sucked in from the fibre inlet. Conversely, air is released the outside from this opening.

According to the principle of mass conservation, the mass flow rates of the fiber and the air outlet are the difference between the mass flow of air from the injectors and the mass absorbed from the fibers, if any, or the amount of air ejected from the fiber inlet.

In the conventional nozzle fiber inlet mass flow value is positive. In other words, air is discharged through this opening. In the modular nozzle, fiber inlet mass flow value is a negative. In this case, we understand that there is air suction from the environment to the twisting chamber.

The air flow velocity value of the modular nozzle configurations and the velocity-dependent z-axis velocity, Reynolds number, vorticity and helical real eigen values were approximately one third of that of conventional nozzles. Although the swirl numbers (*Sn*) of the modular nozzle configurations given in Table 6 are lower than the conventional nozzles, the geometric swirl numbers (*Sg*) are relatively high compared to the conventional nozzles (Table 5).

According to the calculations made in the plane in which the injectors are opened to the twisting chamber in the comparative structural configurations, the total pressure values of conventional nozzles are

Table 5: CFD analysis results of conventional nozzles with twisting chamber diameter ϕ = 3 mm, injector diameter ϕ = 0.5 mm and three circumferential injectors (225 kPa absolute)

Injector angle (degree)	20	25	30	35	40
Injector air inlet mass flow rate (kg/s)	0.000336	0.000343	0.000349	0.000358	0.000376
Fibre inlet mass flow rate (kg/s)	0.000217	0.000241	0.000267	0.000301	0.000332
Fibre and air outlet mass flow rate (kg/s)	–0.000553	–0.000584	–0.000616	–0.000659	–0.000708
Swirl number (S_n)	3.38	3.175	2.908	2.626	2.308
Geometric swirl number (S_g)	4.166	3.746	3.333	2.903	2.597
Total pressure (Pa)	44161	42443	41943	41793	41972
Flow pressure (Pa)	6375	7625	8576	9075	9399
Reynolds number (Re)	39820	39047	39543	40456	41238
Velocity (m/s)	202.9	201.1	203.7	208.4	212.4
Velocity w (fibre axis) (m/s)	64.7	68.6	72.5	77.6	84.4
Vorticity	708257	687890	675408	675006	682107
Helicity real eigen	599981	574558	541261	537100	522006

Table 6: CFD analysis results of modular nozzle's with twisting chamber diameter ϕ = 3 mm, injector diameter ϕ = 0.5 mm and three circumferential injectors (225 kPa absolute)

Injector angle (°)	20	25	30	35	40
Injector air inlet mass flow rate (kg/s)	0.000375	0.000394	0.000397	0.000397	0.000399
Fibre inlet mass flow rate (kg/s)	–0.000049	–0.000018	–0.000011	–0.000024	0.000010
Fibre and air outlet mass flow rate (kg/s)	–0.000326	–0.000375	–0.000386	–0.000374	–0.000410
Swirl number (S_n)	0.433	0.395	0.306	0.343	0.348
Geometric swirl number (S_g)	14.92	11.968	10.972	11.114	8.71
Total pressure (Pa)	–493	1026	–428	–650	143
Flow pressure (Pa)	–1036	72	–1934	–2539	–1390
Reynolds number (Re)	12552	14671	9359	11246	9666
Velocity (m/s)	64.6	75.6	48.2	57.9	49.8
Velocity w (fibre axis) (m/s)	14.2	10.1	21	16.6	24.2
Vorticity	225448	223036	197273	233608	230605
Helicity real eigen	172484	156333	138241	171569	171734

above 40 kPa, while the total pressure value in modular nozzles is just below or just above 0 kPa. Similarly, the flow pressure value of conventional nozzles is above 6 kPa, while the flow pressure value of modular nozzles is below 0 kPa.

According to the graphical comparison of yarn hairiness of the modular nozzles and conventional nozzles in Figure 8, modular nozzles with a pressure of 125 kPa (225 kPa absolute) demonstrated the lowest yarn hairiness at injector angle configurations of 20°, 40°, 25° , 30° and 35°. According to the modular nozzle YZ plane vorticity CFD result in Figure 22, the order of vorticity from highest value to lowest value is seen at injector angle configurations of 20°, 25°, 30°, 35° and 40°. If the measurement at 40° in Figure 8 is not taken into account, the increase in the amount of vorticity resulted in a decrease in yarn hairiness. A similar situation was seen in the helicity real eigen CFD results in the YZ plane (Figure 24).

According to the graphical comparison of yarn hairiness of the modular nozzles and conventional nozzles in Figure 8, conventional nozzles with a pressure of 125 kPa (gauge) demonstrated the lowest yarn hairiness at injector angle configurations of 20°, 40°, 25° , 30° and 35°. According to the modular nozzle YZ plane vorticity CFD result in Figure 15, the order of vorticity from highest value to lowest value is seen at injector angle configurations 40°, 35°, 30°, 25° and 20°. A similar situation was seen in the helicity real eigen CFD results in the YZ plane (Figure 17).

3.6 CFD verification

The CFD validation process was addressed and validated in a study similar to this one [11].

4 Conclusion and outlook

- Comparing conventional jet-ring nozzles with modular jet-ring nozzles in terms of yarn hairiness value, modular jet-ring nozzles proved to be more successful in reducing yarn hairiness values. The main objective of jet-ring nozzles is to reduce yarn hairiness values.
- When hairiness values are considered, conventional jet-ring nozzles and modular jet-ring nozzles form an antithesis relative to one another in terms of the injector angle structural parameter. In the 20° injector angle structural configuration, conventional jet-ring nozzles gave the best yarn hairiness values, while modular jet-ring nozzles gave the worst yarn hairiness values. In the 35° injector angle structural configuration, hairiness values were reversed. In other words, modular and conventional nozzles formed an antithesis with respect to one another in terms of yarn hairiness values according to their injector angle structural configurations.
- In modular and conventional nozzles with generally known structural configurations, an increase in pressure led to an increase in yarn hairiness.
- It is generally understood that the irregularity values of yarns produced using modular jet-ring

nozzles are higher than those produced using conventional jet-ring nozzles.
- It is generally understood that the elongation values of the yarns produced using modular jet-ring nozzles are lower than those produced using conventional jet-ring nozzles.
- When the air pressure was set to 75 kPa (gauge), yarn tenacity values were higher in the yarns produced using conventional jet-ring nozzles, and higher in the yarns produced in modular jet-ring nozzle when it was set to 125 kPa (gauge).
- Comparing the flow parameters of yarn hairiness (CFD analysis), it was found that increasing vorticity or helicity real eigen values reduced yarn hairiness. Yarn hairiness can be minimised if both conventional nozzles and modular nozzles concentrate on structural configurations that can maximise vorticity or helicity real eigen values to reduce yarn hairiness.
- According to the structural configurations that maximise vorticity or helicity real eigen values in conventional nozzles, the twisting chamber diameter should be at the lowest value (ϕ = 2 mm).
- No significant correlation was found between other structural parameters and vorticity or helical real eigen values in conventional nozzles. However, in conventional nozzles, vorticity or helical real eigen values were high in the 35–40° injector angle configurations.
- In modular nozzles, on the contrary, vorticity or helical real eigen values were high in the 20–25° injector angle configurations and low in the 35–40° injector angle configurations.
- It is precisely for this reason that the yarn produced using modular nozzles demonstrated a low hairiness value when a low injector angle was set and a high hairiness value when a high injector angle was set, which can be explained logically when comparing vorticity or helicity real eigen values.

Acknowledgement

This work was supported by grants from the Unit of Scientific Research Projects of Isparta (Suleyman Demirel University) in Turkey [Project 4995-D1-17]. We would like to thank H. Husnu Isik, the owner of Adim Textile Industry and Trade Inc. (Isparta, Turkey), and Ayse Korkut, the production manager at Adim Textile Industry and Trade Inc., for support in yarn production and yarn hairiness testing. The authors also wish to express their thanks to Umit Tasdeler for his collaboration.

References

1. GUO, Hui-Fen, YU, Chong-Wen, XU, Bin-Gang, LI, Sheng-Yan. Effect of the geometric parameters on a flexible fibre motion in a tangentially injected divergent swirling tube flow. *International Journal of Engineering Science,* 2011, **49**(10), 1033–1046, doi: 10.1016/j.ijengsci.2011.06.002.
2. YILMAZ, Demet, USAL, Mustafa Resit. A comparison of compact-jet, compact, and conventional ring-spun yarns. *Textile Research Journal*, 2011, **81**(5), 459–470, doi: 10.1177/0040517510385174.
3. WANG, Xungai, MIAO, Menghe, HOW, Yanlai. Studies of JetRing spinning. Part I: reducing yarn hairiness with the JetRing. *Textile Research Journal,* 1997, **67**(4), 253–258, doi: 10.1177/004051759706700403.
4. *Ansys fluent theory guide*. Canonsburg : Ansys, 2001, p. 868.
5. AKANSU, Selahaddin Orhan. Heat transfers and pressure drops for porous-ring turbulators in a circular pipe. *Applied Energy*, 2006, **83**(3), 280–298, doi: 10.1016/j.apenergy.2005.02.003.
6. EBERLINC, Matjaž, ŠIROK, Brane, HOČEVAR, Marko, DULAR, Matevž. Numerical and experimental investigation of axial fan with trailing edge self-induced blowing. *Forsch im Ingenieurwesen / Engineering Research*, 2009, **73**(3), 129–138, doi: 10.1007/s10010-008-0086-8.
7. MANI, Sivabalan, SANAL, Kumar V.R. 3D flow visualization and geometry optimization of cavity based scramjet combustors using k-ω model. In *51st AIAA/SAE/ASEE Joint Propulsion Conference.* (AIAA Propulsion and Energy Forum). Reston : American Institute of Aeronautics and Astronautics, 2015, doi: 10.2514/6.2015-3946.
8. SHAHİD, Mahmood, HUANG, De-Bo. Resistance calculations of trimaran hull form using computational fluid dynamics. In *Proceedings : Fourth International Joint Conference on Computational Sciences and Optimization, CSO 2011.* Los Alamitos : CPS, 2011, 81–85, doi: 10.1109/CSO.2011.225.
9. ŠIMIC, Marko, HERAKOVIČ, Niko. Reduction of the flow forces in a small hydraulic seat valve as alternative approach to improve the valve characteristics. *Energy Conversion and Management*, 2015, **89**, 708–718, doi: 10.1016/j.enconman.2014.10.037.

10. DENG, Ruoyu, JIN, Yingzi, KIM, Heuy Dong. Numerical simulation of the unstart process of dual-mode scramjet. *International Journal of Heat and Mass Transfer,* 2017, **105**, 394–400, doi: 10.1016/j.ijheatmasstransfer.2016.10.004.
11. GULSEVINCLER, Ekrem, USAL, Mustafa Resit, YILMAZ, Demet. The effects of structural parameters on tangentially injected highly swirling turbulent tube air flow. *SN Applied Sciences*, 2019, **1**(8), 1–26, doi: 10.1007/s42452-019-0850-4.
12. YILMAZ, Demet, USAL, Mustafa Resit. Effect of nozzle structural parameters on hairiness of compact-jet yarns. *Journal of Engineered Fibers and Fabrics*, 2012, **7**(2), 56–65, doi: 10.1177/155892501200700209.
13. YILMAZ, Demet, USAL, Mustafa Resit. A study on siro-jet spinning system. *Fibres and Polymers*, 2012, **13**(10), 1359–1367, doi: 10.1007/s12221-012-1359-2.
14. YILMAZ, Demet, USAL, Mustafa Resit. Improvement in yarn hairiness by the siro-jet spinning method. *Textile Research Journal,* 2013, **83**(10), 1081–1100, doi: 10.1177/0040517512471748.
15. SU, Xuzhong, LIU, Xinjin, LIU, Xiaoyan. Numerical simulation of flow field in the pneumatic compact spinning systems using finite element method. *International Journal of Clothing Science and Technology,* 2018, **30**(3), 363–379, doi: 10.1108/IJCST-11-2017-0180.
16. GULSEVINCLER, Ekrem, USAL, Mustafa Resit, YILMAZ, Demet. Effects of nozzle structural parameters on yarn hairiness in jet-ring spinning system. *The Journal of the Textile Institute,* 2020 (in press), 1–11, doi: 10.1080/00405000.2020.1716527.
17. YILMAZ, Demet. Development and numerical modelling of plied yarn production process based on the usage of high velocity air. *Ph.D. thesis*. Isparta : Suleyman Demirel University, 2011.

Akhtarul Islam Amjad, Rajiv Kumar
M L V Textile and Engineering College, Bhilwara, Department of Textile Engineering, Rajasthan, 311001, India

Evaluation of Mechanical and Physical Characteristics of Eco blended Melange Yarns

Vrednotenje mehanskih in fizikalnih lastnosti ekomelanžne preje

Original scientific article/*Izvirni znanstveni članek*
Received/*Prispelo* 2-2020 • Accepted/*Sprejeto* 5-2020

Abstract

The production and consumption of melange yarns are gradually increasing due to natural multi-colours and strong 3D fashionable effects. The raw material and chemical processing influence the environmental and textile values of the melange yarn. Organic cotton and regenerated cellulose fibres are basic raw materials for eco-friendly production of yarns. In this study three different regenerated fibres are blended with organic cotton in three different ratios to manufacture the blended melange yarns of two different shade depths. Therefore, cotton-bamboo viscose, cotton-lyocell and cotton-SeaCell™ blended melange yarns with three blend combination 30/70, 50/50 and 70/30 are manufactured. All the dyed and grey components are mixed at the blow room. The aim of the study is to investigate impact of raw material and blend ratio on mechanical and physical characteristics of different shade depth blended melange yarns. Better yarn characteristics with respect to yarn evenness, imperfections, hairiness, tenacity, elongation, coefficient of friction and diameter are achieved for lower shade depth melange yarn. In cotton-rich blended melange yarns, elongation, hairiness, evenness, total imperfections and diameter are noticeably worse for all the combinations. Statistical analysis shows significant effect of blend type, blend ratio and shade depth on the all yarn properties.

Keywords: bamboo viscose, *Tencel™*, *SeaCell™*, shade depth, melange spinning

Izvleček

Proizvodnja in poraba melanžne preje se postopoma povečuje zaradi naravne večbarvnosti in zelo modnih 3D estetskih učinkov. Surovine in kemična obdelava vplivajo na okolje in tekstilne lastnosti melanžne preje. Organski bombaž in regenerirana celulozna vlakna so osnovne surovine za okolju prijazno proizvodnjo preje. Z namenom, da bi dosegli različne barvne nianse, so bile v študiji izdelane melanžne preje iz mešanic vlaken bombaž/bambusova viskoza, bombaž/liocel in bombaž/SeaCell™, v razmerjih 30/70, 50/50 in 70/30. Barvane in surove komponente vlaken so bile mešane v fazah priprave prediva. Namen študije je bil raziskati vpliv razmerja surovin v mešanicah na mehanske in fizikalne lastnosti melanžnih prej. Boljše lastnosti prej glede enakomernosti, količine napak, kosmatosti, trdnosti, raztezka, koeficienta trenja in premera so bile dosežene pri melanžnih prejah s svetlejšim barvnim tonom. V melanžnih prejah z večjim deležem bombaža so bile pri vseh mešanicah ugotovljene slabše vrednosti raztezka, kosmatosti, enakomernosti, količine napak in premera. Statistična analiza je pokazala pomemben vpliv vrste mešanice, razmerja mešanice in globine barvnega tona na vse lastnosti preje.

Ključne besede: bambusova viskoza, Tencel™, SeaCell™, barvne nianse, izdelava melanžne preje

Corresponding author/*Korespondenčni avtor:*
Akhtarul Islam Amjad
E-mail: akh.textile@gmail.com
ORCID: 0000-0002-9667-4012

Tekstilec, 2020, ***63****(2), 94-103*
DOI: 10.14502/Tekstilec2020.63.94-103

1 Introduction

The increase in global demand for clothing is expected to continue, not only due to an increase in the world's population, but also due to living standards, economic activities and developments. In the present era, clothing serves many purposes. It not only satisfies the basic needs of human beings, but is also used as a symbol to express wealth, status, occupation, leisure and eco-friendliness [1]. Fibre is one of the basic units for producing desirable clothes [2]. Biodegradable and sustainable fibres are being developed for environmental protection and providing a significant opportunity for sustainable textiles [3].

Cotton is considered the most eco-friendly, but the use of insecticides and pesticides in cultivation make it less sustainable. Organic cotton and regenerated cellulose fibres may serve as a substitute for polluted cotton [4]. Regenerated cellulose fibres, such as viscose rayon, bamboo rayon, modal rayon, lyocell and SeaCell™ are widely considered the most important for environmental aspects and often referred to as environmentally friendly [5]. Bamboo rayon is produced by wet spinning, while lyocell and SeaCell™ fibres are produced by solvent spinning. Bamboo rayon is naturally antibacterial, breathable, green, biodegradable, soft, flexible and strong, with a luxurious, shiny appearance [6]. Modal is a second generation regenerated cellulose fibre and is known for its softness [5]. Lyocell is a third-generation fibre. It is highly absorbent, soft, has a high wet or dry strength, and is wrinkle resistant [7]. SeaCell™ and smartcell are modified versions of third generation fibre. Their advantages include the environmental friendliness of processing, combined with their softness, drape and antibacterial properties [8-10].

In the production of SeaCell™ fibre, powdered seaweeds are firmly incorporated into a natural cellulose fibre. As a result, the positive properties of the seaweed are permanently preserved within the fibre, even after multiple washes [10, 11].

All regenerated cellulosic fibres have the same basic unit, but are quite different in degree of polymerisation, molecular arrangement, molecular mass, degree of orientation and crystallinity [12]. The lyocell and SeaCell™ have a circular cross section and a smooth longitudinal surface. On the other hand, bamboo rayon and viscose rayon possess an irregular and toothed cross section, micro-gaps and micro-holes with striated cracks distributed over the longitudinal surface [13, 14].

A single fibre yarn cannot offer all the desired characteristics. The blending of different types of fibres not only enhances the functional or mechanical performance, but also the aesthetic qualities of textile fabric. Blending is also practiced in industry for cost minimisation [15, 16]. Many researchers have investigated blended yarn properties and analysed their functional and mechanical attributes. Sowmya et al. [15] reported that yarn unevenness is affected by the blended ratio of cotton, polyester, and regenerated bamboo fibre. They also reported that the work of rupture and elongation at break of bamboo-cotton blended yarns are found to be lower than those of bamboo/polyester-blended yarns. Tyagi et al. [16] reported that Tencel™-polyester yarns yield more satisfactory results than Tencel™-cotton yarns in terms of tenacity, breaking elongation, mass regularity, imperfections and work of rupture for all spinning system. Increasing the Tencel™ content both in Tencel™-polyester and Tencel™-cotton fibre blends makes the yarn rigid and hairier. Kilic et al. [17] determined that yarn-to-yarn friction decreases, while yarn-to-metal and yarn-to-ceramic friction increases when the ratio of Tencel™ in Tencel™-cotton blended yarn is increased. Majumdar et al. [6] reported that yarn diameter reduces as the proportion of bamboo fibre is increased in the blend of bamboo cotton fibre. Kılıç and Okur [14] found that unevenness, imperfections, diameter and roughness values decrease when the regenerated cellulosic fibre content in cotton-Tencel™ and cotton-paramodal blended yarns is increased, while increasing breaking force, elongation, density and shape values. Avik et al. [11] worked on the functional properties of SeaCell™ sock and summarise that SeaCell™ socks may be a good choice for people with foot problems such as fungus. SeaCell™ fibre has a more homogenous pore distribution, which in turn facilitates improved water transport.

All of the above research was performed on the manufacturing of plain blended yarn. But there is another field where the blending/mixing of different colours or the dye affinities of fibres are performed for the production of fancy or melange yarns [18–19]. Melange yarns are fancy yarns consisting of a wavy effect, a wide range of colour tones and unique colour effects. They are manufactured to achieve higher rates due to the aesthetics and obsolescence of fashion [20]. Researchers reported that cotton fibres suffer from a decrease in strength

and change in surface properties after being dyed due to the aggressive nature of chemicals and the removal of a large portion of the wax present on the surface of cotton fibres [21, 22]. The dyeing of fibres results in their greater entanglement and cohesion. The average length of dyed fibre decreases with a higher rate than that of undyed fibre after going through opening and mechanical processes. Various stages of spinning cause tip fibrillation, end rupture, transverse cracks, deep cracks, a saw-tooth effect and rippling damage. Dyed fibres are more prone to damage than undyed fibres [22, 23]. Fibre damage not only affects the efficiency of the spinning process, but also the mechanical properties of the final yarn and fabric. The quality of cotton melange yarn is affected significantly by the applied blending method [24, 25].

Conventional approaches used in the manufacturing of melange yarn are entirely dependent on cotton fibre in the melange yarn industry. None of the researchers mentioned above have focused on the properties of eco-friendly blended melange yarns. In this study, two different shade depth cotton blended melange yarns were produced using bamboo viscose, lyocell and SeaCell™ fibres in three different proportions that might be useful for the textile melange yarn industry in terms of exploring new applications for melange products.

2 Materials and methods

2.1 Materials for melange yarn production

Dyed and grey H-4 organic combed cotton, bamboo viscose, lyocell and SeaCell™ fibres were used to produce 19.68 tex (30s Ne) melange yarns. The properties of the fibres that were used to produce the yarns are summarised in Tables 1a and 1b.

The results presented in Tables 1a and 1b show that dyeing and opening have an adverse effect on the tensile and length properties of fibres. It was also observed that cotton fibres show incremental changes in short fibre content and neps/g after dyeing and opening.

2.2 Melange yarn production

The mixing or blending of dyed and un-dyed (grey) fibres in predefined ratios results in melange yarns. Shade depth (%) is a common term used in melange yarn spinning to illustrate the percentage contribution of dyed fibre in a blend. In this study, the blending of fibres (dyed/un-dyed, cotton or regenerated cellulose) was performed in a blow room to achieve the perfect regularity of colour and structure. Figure 1 depicts the process flow of melange yarn spinning. Grey fibres for dyeing or mixing are prepared in the first stage. A predefined amount of grey fibres is dyed in the second stage, while the third stage involves the stack blending of grey and dyed fibres in the required ratio in the blow room. Cotton fibres

Table 1a: Properties of combed grey and dyed cotton fibres

Fibre quality	Instruments					
	HVI (HVI mode)				AFIS	
	Fineness (mic.)	Length (mm)	Strength (g/tex)	Elongation (%)	Short fibre content (%)	Fibre neps (neps/g)
Grey combed	4.23	29.3	29.37	6.14	18.02	14
Dyed combed	4.2	29.0	28.12	5.9	19.32	18
Dyed combed (after opening)	4.2	28.7	27.24	5.97	21.57	24

Table 1b: Properties of grey and dyed regenerated cellulose fibres

Type of fibre	Bamboo viscose (BV)		Lyocell (L)		SeaCell™ (S)	
	Grey	Dyed	Grey	Dyed	Grey	Dyed
Fineness (dtex)	1.56	1.56	1.56	1.56	1.67	1.67
Length (mm)	37.90 (38)	37.65 (38)	37.92 (38)	37.81(38)	37.9(38)	37.7(38)
Strength (g/tex)	23.2	21.0	36.23	35.0	29.00	28.1
Elongation (%)	11.8	11.5	9.7	9.5	11.2	10.9

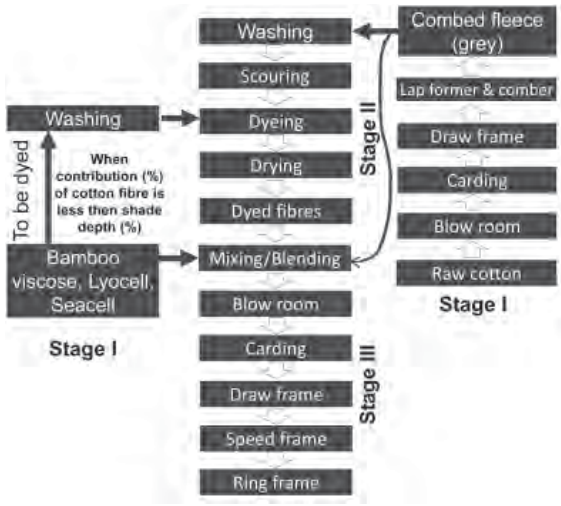

Figure 1: Process flow of melange yarn manufacturing

are preferred over the regenerated cellulose fibres for dyeing to achieve the proper shade depth (%).

2.3 Design of experiment

Light and dark melange yarns were produced on a short staple spinning machine by blending three different fibres and blend compositions with cotton. All the process variables were kept constant. The aim of varying the factors was to investigate the interaction effect of fibre properties and composition with different shade depths. The design plan of the experiment is presented in Table 2. A total of 18 yarn samples were manufactured according to full factorial design.

2.4 Methods

The yarn samples were conditioned at a standard tropical atmospheric condition of 65 ± 2% RH and 27 ± 2 °C temperatures for 24 hours.

2.4.1 Tensile testing of yarn

An Instron universal testing machine was used to measure the breaking load and extension properties. The yarn samples were tested at 120 mm/min extension rate using a gauge length of 500 mm (ASTM D 2256). A total of 50 readings were taken for each sample.

2.4.2 Unevenness, thin, thick, neps and hairiness

The unevenness, thin, thick, neps and hairiness were measured using an Uster Evenness Tester-5. Thin places (-50%), thick places (+50%) and neps (+200%) were considered to measure total imperfection in the melange yarn.

2.4.3 Yarn diameter

The diameter of yarn was measured by an optical method using a Leica image analyser. At least 100 readings were taken for each sample.

2.4.4 Coefficient of friction

An Uster Zweigle Friction Tester 5 was used to measure fibre to metal friction. The friction coefficient (μ) was calculated using the formula $F_2 = \mu F_1$, where F_1 is constant force applied to produce a defined force on the yarn in a vertical direction and F_2 is the force required to pull the yarn.

3 Results and discussion

This paper includes an analysis of cotton blended melange yarn with varying parameters. In this study, parameters were assessed in terms of unevenness, total imperfections, hairiness, tenacity, elongation, yarn diameter and coefficient of friction of the melange yarns. An analysis of variance was carried out to determine the effect of different parameters on yarn properties. The ANOVA of the parameters is presented in Table 3.

It is evident from Table 3 that the blend ratio has a significant impact on all the properties of the yarn, while blend type has a significant effect on all properties except unevenness.

Table 2: Experiment design plan

Sr. No.	Factors	Levels		
1	Blend type	Cotton/Bamboo viscose (C/BV)	Cotton/Lyocell (C/L)	Cotton/SeaCell™ (C/S)
2	Blend ratio	30/70	50/50	70/30
3	Shade depth (%)	20 (light); 70 (dark)	20 (light); 70 (dark)	20 (light); 70 (dark)

Table 3: ANOVA results for yarn characteristics

Factors	Unevenness	IPI	Hairiness	Tenacity	Breaking Extension	Diameter	Coefficient of friction
BT	NS (0.19)	S (0.000)	S (0.0009)	S (0.000)	S (0.000)	S (0.014)	S (0.001)
BR	S (0.0003)	S (0.000)	S (0.0001)	S (0.0001)	S (0.0000)	S (0.034))	S (0.0000)
SD	S (0.0001)	S (0.000)	S (0.001)	S (0.029)	S (0.0004)	NS (0.450)	S (0.006)
BT×BR	NS (0.5757)	NS (0.172)	NS (0.163)	S (0.0004)	S (0.0001)	NS (0.283)	NS (0.216)
BT×SD	NS (0.2813)	S (0.0001)	NS (0.792)	S (0.002)	S (0.013)	NS (0.146)	NS (0.444)
BR×SD	S (0.0226)	S (0.045)	NS (0.664)	S (0.027)	NS (0.18)	NS (0.683)	NS (0.500)

BT – blend type, BR – blend ratio, SD – shade depth. Values in parenthesis are p-values, calculated at 95% statistical probability: $p \leq 0.05$ – result is statistically significant (S), $p > 0.05$ – result is not statistically significant (NS)

3.1 Tensile characteristics of melange yarn

The tensile attributes of a staple fibre melange yarn are influenced by fibre characteristics. Tenacity and breaking extension are important properties for assessing the tensile behaviour of melange yarn. Blend type, blend ratio and shade depth have a significant impact on the tenacity and breaking extension of blended melange yarn (Table 3). Tenacity is the applied load with respect to fineness at which a specimen breaks. The effect of blend type and blend ratio on tenacity for different shade depth blended melange yarns is presented in Figure 2.

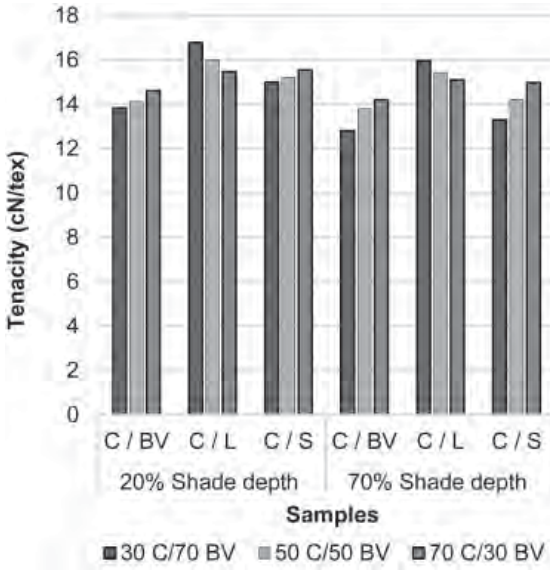

Figure 2: Effect of blend type and blend ratio on tenacity

It is evident from Figure 2 that:

- cotton-lyocell blended yarn shows the highest tenacity, followed by cotton-SeaCell™ and cotton-bamboo viscose blended yarns for both shade depths;
- melange yarn tenacity increases with an increase in the cotton component in the case of bamboo viscose and SeaCell™-blended yarns, and decreases in lyocell-blended yarn; and
- tenacity of melange yarn decreases with an increase in shade depth.

Lyocell fibres have a high degree of polymerisation compared to bamboo viscose and SeaCell™ fibres due to their long molecular chains [13], so that the strength of the yarns produced from lyocell fibre showed a higher tenacity, followed by cotton-SeaCell™ and cotton-bamboo viscose blended yarn for both shade depths.

The bamboo viscose fibre has a lower strength and higher amorphous region in the macromolecular structure than cotton fibre. Blended yarn with rich bamboo viscose fibre demonstrates a lower tenacity. SeaCell™ fibre possesses much higher elongation than cotton fibre. During the loading of cotton-SeaCell™ blended yarn, cotton fibres will resist further elongation and are expected to reach the breaking point earlier. The difference is marginal.

Dyed fibres are weaker than undyed fibre (Table 1), while 70% shade depth melange yarn consists of more dyed fibre. Simultaneously dyeing causes entanglement, causes difficulties during opening and drafting, and ultimately leads to rupture. For these reasons, the load bearing capacity of survival fibres decreases and stress increases during tensile testing, causing a rupture to propagate faster across the cross section in high shade depth yarn.

The effect of blend type and blend ratio on the percentage of elongation for different shade depth blended melange yarns is illustrated in Figure 3.

It is evident from Figure 3 that:

- cotton-bamboo viscose blended yarn shows the highest percentage of elongation, followed by cotton

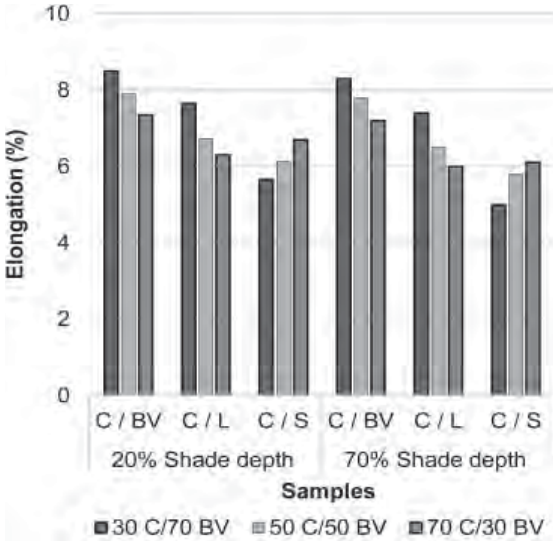

Figure 3: Effect of blend type and blend ratio on breaking extension

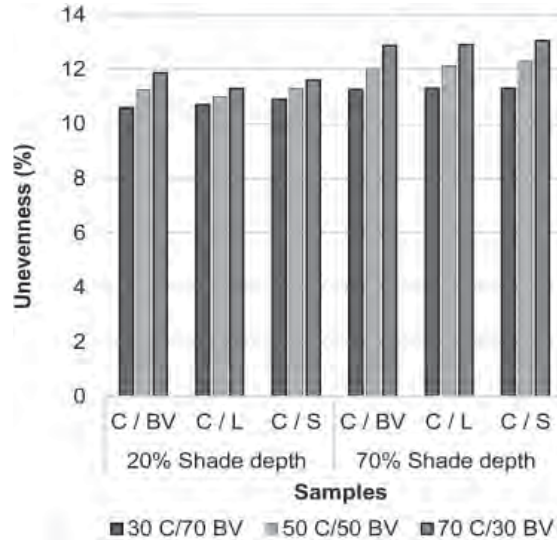

Figure 4: Effect of blend type and blend ratio on unevenness

lyocell and cotton-SeaCell™ blended yarns for all type of samples;
- the percentage of elongation decreases as the ratio of cotton increased; and
- 70% shade depth melange yarn demonstrates the lowest percentage of elongation.

Because fibre elongation properties directly affect yarn elongation, higher elongation values of regenerated fibres result in high elongation values in all 30/70 blended melange yarns. Cotton- lyocell blend yarns demonstrated the lowest percentage of elongation, while it is also evident from Table 1 that lyocell fibre showed a lower elongation than all regenerated fibres. It is evident that a high number of dyed fibres are present in the yarn cross section for high depth melange yarn and, similar to tenacity, they will reduce the percentage of elongation.

3.2 Unevenness of melange yarn

Unevenness (U expressed in %) shows the mass irregularity per unit length in the yarn. No significant difference in unevenness is observed for the type of blend. This may be due to the almost identical production process and the dimensional properties of all three regenerated fibres. Blend ratio and shade depth had a significant impact on the unevenness of melange yarns (Table 3). Figure 4 illustrates in graphical form the effect of blend type and blend ratio on the unevenness of different shade depth blended melange yarns.

It is evident from Figure 4 that:
- an increase of the cotton fibre contribution leads to the high unevenness of the yarn irrespective of other factors; and
- unevenness of darker melange yarns is higher than that of low depth melange yarns.

The arrangement of fibres and fibre properties influence yarn characteristics. Cotton is a naturally grown fibre, and is highly variable in terms of length and fineness relative to regenerated fibres. Cotton fibres are shorter in length than regenerated fibres (Table 1). Any variation in the fibres negatively affects the mechanical and physical properties of yarn. As the percentage of cotton increases, the availability of shorter fibres increases in the spinning system and decreases mean fibre length in the yarn structure, so that consolidation at the nip point during yarn manufacturing is lesser, which generates a greater amplitude of drafting waves. Mass irregularity thus increases.

Opening difficulties are seen more in high shade depth melange blends, as they consist of more dyed fibres. These difficulties cause the uncontrolled and erratic movement of fibres in the drafting area and eventually result in increased yarn mass variation.

3.3 Total imperfection of melange yarn

The imperfection index (IPI) consists of thin, thick and neps per unit length of yarn. Blend type, blend ratio and shade depth had a significant impact on

the total imperfection of blended melange yarn (Table 3). Figure 5 illustrates in graphical form the effect of fibre blend type and blend ratio on total imperfection.

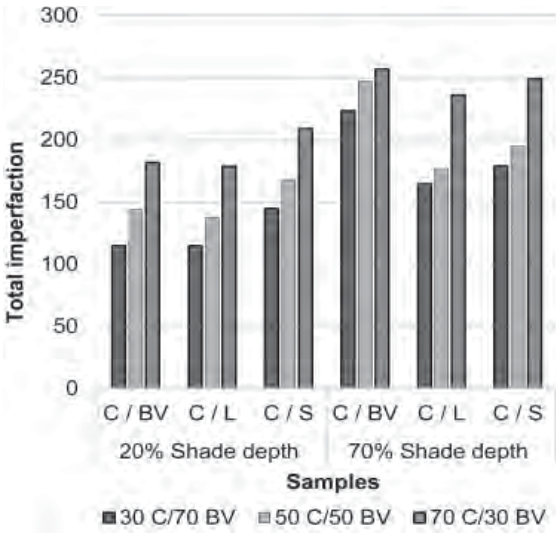

Figure 5: Effect of blend type and blend ratio on total imperfection

It is evident from Figure 5 that:

- a higher percentage of cotton leads to an increase in the total imperfection level in blended melange yarn;
- cotton-bamboo blend yarn demonstrates the highest and cotton-lyocell blended yarn the lowest total imperfection; and
- total imperfection increases with an increase in shade depth irrespective of blend type and blend ratio.

Regenerated fibres are known to have more a uniform shape and size in their longitudinal direction, while cotton fibres show a twisted structure. Simultaneously blended yarn with higher regenerated fibres consists of fewer shorter fibres and a higher mean fibre length, so that control over the movement of fibres is easy and imparts better association and orientation in yarn structure. Hence, higher cotton contribution leads to an increase in the total imperfection level in blended melange yarn.

The proportions of dyed fibres are higher in the high shade depth melange yarns. Dyeing changes the surface properties of the fibres, damages the fibres and increases fibre-to-fibre friction due to the removal of natural wax [23]. High fibre-to-fibre friction causes difficulties in the opening and drafting of fibres, which ultimately leads to the poor arrangement and distribution of fibre in yarn. Thus, higher yarn imperfections are seen for darker shades.

3.4 Hairiness of melange yarn

The hairiness of a yarn is the result of fibre protrusion from the yarn surface. Hairiness in spun yarn depends primarily on fibre properties such as the length, shape and bending rigidity of fibres. The effect of blend type, blend ratio and shade depth on the hairiness of melange yarn is significant (Table 3).

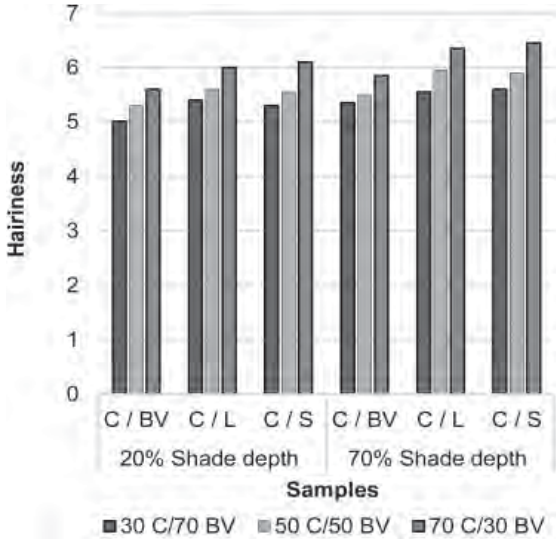

Figure 6: Effect of blend type and blend ratio on hairiness

It is evident from Figure 6 that:

- hairiness of melange yarn increases with an increase in the percentage of cotton in blended melange yarn;
- cotton-lyocell and cotton-SeaCell™ blended yarns demonstrate a marginal difference, while cotton-bamboo viscose blended yarn shows the lowest hairiness; and
- hairiness of melange yarn increases with an increase in shade depth.

Bamboo viscose, lyocell and SeaCell™ fibres have a longer length than the cotton fibres. Moreover, short fibres are totally absent in the all three fibres. The flexural and torsional rigidity of all three fibres are also lower than that of cotton fibre. Regenerated fibres are thus wrapped and adhered with the internal structure of melange yarn in the twisting triangle. As a result, hairiness decreases with an increase in the proportion of regenerated fibres.

The cross-section of lyocell and SeaCell™ fibre is round and the surface is smooth, while bamboo viscose fibre has an irregular and toothed shape [13]. On the other hand, bamboo viscose fibre shows a lower torsional rigidity than lyocell and SeaCell™ fibre. These properties of bamboo viscose fibres cause higher inter-fibre friction, while a better consolidation of surface hair in the main yarn structure ensures low hairiness.

The chemical and mechanical processing of fibres in melange yarn manufacturing causes rupture and high short fibre generation. Short fibres have a tendency to come out from the yarn body and do not wrap with the main body of melange yarn during twisting. Moreover, control over the short fibres is also difficult during drafting. High depth melange yarn consists of more such fibre, which results in a high level of hairiness.

3.5 Diameter of melange yarn

The surface characteristics and appearance of a yarn influence the appearance of products made from that yarn. No significant difference in the diameter is observed for the shade depth. The type of fibre and blend ratio have a significant impact (see Table 3). Figure 7 illustrates in graphical form the effect of blend type and blend ratio on diameter for different shade depth blended melange yarns.

It is evident from Figure 6 that:

- diameter of melange yarn increases with an increase in the percentage of cotton in blended melange yarn; and
- cotton-lyocell blended yarn shows the lowest diameter, followed by cotton-SeaCell™ and cotton-bamboo viscose blended yarn.

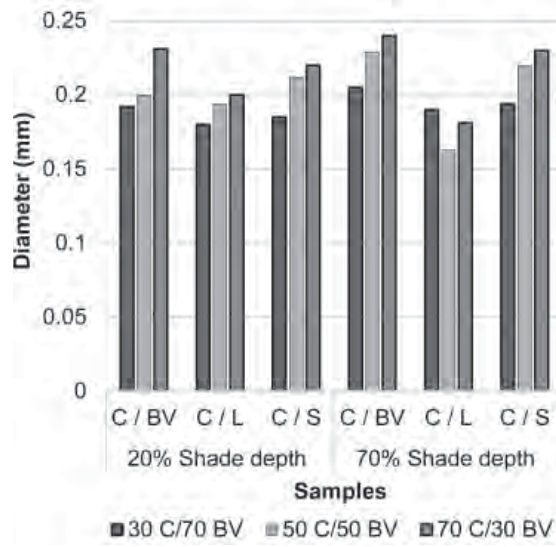

Figure 7: Effect of blend type and blend ratio on diameter

Yarn diameter steadily increases with an increase in the percentage of cotton in the yarn composition. As discussed, all of the regenerated fibres have a longer length (38 mm) than that of cotton fibres. Moreover, they have lower bending and torsional rigidity than cotton fibre. On the other hand, the non-circular cross-section of cotton does not allow close association. Thus, fewer cotton fibres in the cross section lead to closed packing in the melange yarn structure and high diameter in cotton-rich blends.

Figure 8 is a microscopic image of blended melange yarns, which shows that lyocell-blended yarn has a compact internal structure and better integrity and thus a lower diameter. On the other hand,

Blend type; shade depth	Blend ratio		
	30/70	50/50	70/30
C/BV; 20%			
C/BV; 70%			
C/L; 20%			
C/S; 20%			

Figure 8: Microscopic image of blended melange yarn

bamboo-blended melange yarn has a more uniform surface and lesser protruding fibres from the main body, while the fibres are rather protruded on the surface in the case of lyocell- and SeaCell™-blended yarns. Bamboo viscose blended yarn thus shows low hairiness.

3.6 Surface friction

Basic yarn properties such as linear density, evenness and strength do not fully account for processing performance and/or fabric quality. Friction plays vital role in expressing interactive behaviour for fibre-to-yarn and yarn-to-fabric modelling. The resistance to movement, characterised by the coefficient of friction, is dependent on the nature of the two contacting surfaces and their actual area of contact. Figure 9 illustrates in graphical form the effect of blend type and blend ratio on the coefficient of friction for different shade depth blended melange yarns.

It is evident from Figure 9 that:

- increase in the percentage of cotton leads to lower value of coefficient of friction;
- cotton-bamboo viscose blended melange yarn shows the highest coefficient of friction, while the differences between cotton-SeaCell™ and cotton-lyocell blended yarns are not significant; and
- the value of the coefficient of friction is marginally higher for high depth melange yarn.

As discussed, increasing the percentage of cotton in the blended melange yarn structure leads to high hairiness values. The same is also evident from Figure 8. On the other hand, cotton fibres have a natural wax that serves as a lubricant when they come in contact with other surfaces. Hence, cotton-rich blended varn shows a lower coefficient of friction.

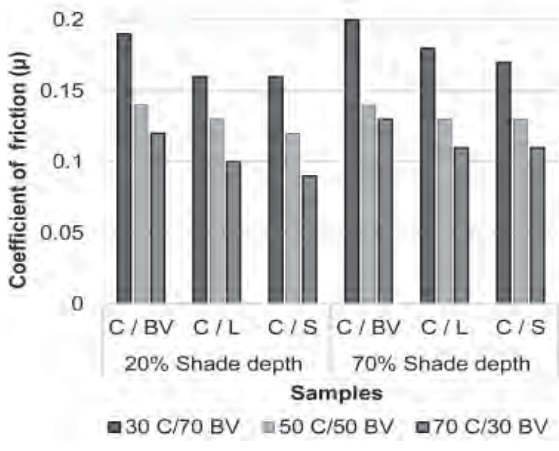

Figure 9: Effect of blend type and blend ratio on coefficient of friction

The frictional characteristics of parent fibres have an impact on the frictional characteristics of blended yarn. Microscopic images show that the surface of bamboo-blended yarn is more uniform and less hairy than SeaCell™- and lyocell-blended yarns (Figure 8). Due to their yarn structure, bamboo-blended yarns show a high coefficient of friction.

In dyeing process, cotton fibre is subject to a scouring process that removes the lubricating layer. The removal of cotton wax increases the coefficient of friction due to underlying rough surface of the layer. On the other hand, the presence of short fibres increases the voluminous of the high depth melange yarn, making the yarn bulkier, which is also evident from Figure 8. Bulkier yarn is more compressible and flattens easier, so the scope of flattening increases when passed over any surface. Hence, higher coefficient of friction values are demonstrated by darker melange yarn.

4 Conclusion

The analysis of the study presents an overview of cotton-bamboo viscose, cotton-lyocell and cotton-SeaCell™ blended melange yarn characteristics, such as strength, elongation, unevenness, hairiness, diameter and friction.

The following conclusion can be reached from the experiments:

- Type of blend, blend ratio and shade depth have a significant affect on blended melange yarn quality. An evaluation of the effect of shade depth on blended melange yarns shows a reduction in strength and elongation. The dyeing and opening of bamboo viscose fibres causes a reduction in strength of up to 9.48%. The lower depth melange yarn contributes to the production of good quality yarns with significantly reduced hairiness and improved mechanical and frictional characteristics.
- Cotton-rich blended yarns show lower friction and elongation, and higher hairiness, total imperfection and unevenness, irrespective of the type of blend. Increasing the cotton content in bamboo- and SeaCell™-blended melange yarns increased tenacity. However, lyocell-blended yarns show the opposite trend.
- Cotton-bamboo blended yarns show the highest diameter and lowest hairiness in all the combination of yarn samples. Cotton-lyocell 30/70 blended yarn gives the strongest blended melange yarn among the studied yarn samples.

References

1. ERYURUK, S. H. Greening of the textile and clothing industry. *Fibres and Textiles in Eastern Europe*, 2012, **95**(6), 22–27.
2. SHABBIR M., MOHAMMAD, F. Sustainable production of regenerated cellulosic fibres. In *Sustainable Fibres and Textiles*. Edited by Subramanian Senthilkannan Muthu. Cambridge : Woodhead Publishing, 2017, 171–189.
3. BLACKBURN, R. S. Introduction. In *Biodegradable and Sustainable Fibres*. Cambridge : Woodhead Publishing, 2005, pp. xiv–xxii.
4. YU, M., WAN, J. Environmental friendly development of regenerated cellulose fiber production. In *Asia-Pacific Engineering and Technology Conference (APETC 2017)*, 2017, 760–765.
5. MARWAHA, S. V. Eco-friendly fibres. Asian Textile Journal, 2006, **15**(5), 58–62.
6. MAJUMDAR, A. MUKHOPADHYAY, S. YADAV, R., MONDAL, A. K. Properties of ring-spun yarns made from cotton and regenerated bamboo fibres. *Indian Journal of Fibre & Textile Research,* 2011, **36**(1), 18–23.
7. BASIT, A. LATIF, W. BAIG, S. A. AFZAL, A. The mechanical and comfort properties of sustainable blended fabrics of bamboo with cotton and regenerated fibres. *Clothing and Textile Research Journal*, 2018, **36**(4), 267–280, doi: 10.1177/0887302X18782778.
8. RIJAVEC, Tatjana, BUKOŠEK, Vili. Novel fibres for the 21st. century. *Tekstilec,* 2009*,* **52**(10-12), 312–27.
9. KILIC G. B. SÜLAR, V. Frictional properties of cotton-Tencel yarns spun in different spinning systems. *Textile Research Journal*, 2012, **82**(8), 755–765, doi: 10.1177/0040517511429610.
10. Smartfiber – the power of seaweed in a fiber [online]. SeaCell [cited 22.01.2020]. Available on: https://www.smartfiber.de/en/fibers/seacelltm/.
11. AVCI, H. ÖZDEMIR, M. İRIDAĞ, B. Y. DURU C. S. CANDAN, C. Comfort properties of socks from seacell fibres. *The Journal of The Textile Institute,* 2017, **109**(3), 419–425, doi: 10.1080/00405000.2017.1351065.
12. KIVRAK, OZDIL, N. MENGÜÇ. G. S. Characteristics of the yarns spun from regenerated cellulosic fibres. *Tekstil ve Konfeksiyon*, 2018, **28**(3), 107–117.
13. XU, Y. LU, Z. TANG, R. Structure and thermal properties of bamboo viscose, Tencel™ and conventional viscose fiber. *Journal of Thermal Analysis and Calorimetry*, 2007, **89**(1), 197–201, doi: 10.1007/s10973-005-7539-1.
14. KILIÇ, M. OKUR, A. The properties of cotton-Tencel and cotton-promodal blended yarns spun in different spinning systems. *Textile Research Journal,* 2011, **81**(2) 156–172, doi: 10.1177/0040517510377828.
15. SOWMYA, R. VASUGI RAAJA N., PRAKASH C. Investigation of relationship between blend ratio and yarn twist on yarn properties of bamboo, cotton,polyester, and its blends. *Journal of Natural Fibres,* 2016, **14**(2), 228–238, doi: 10.1080/15440478.2016.1193087.
16. TYAGI G. K. GOYAL A., CHATTOPADHYAY, R. Physical characteristics of tencel-polyester and tencel-cotton yarns produced on ring, rotor and air-jet spinning machines. *Indian Journal of Fibre & Textile Research*, 2013, **38**(3), 230–236.
17. KILIC, G.B., VILDAN, S. Frictional properties of cotton-Tencel yarns spun in different spinning systems, *Textile Research Journal.* 2012, **82**(8), 755–765, doi: 10.1177/0040517511429610.
18. ERDUMLU, N. OZIPEK, B. Investigation of regenerated bamboo fiber and yarn characteristics. *Fibres & Textiles in Eastern Europe,* 2008, **16**(4), 43–47.
19. REGAR, M. L. AMJAD, A.I. AIKAT, N. Studies on the properties of ring and compact spun melange yarn. *International Journal of Advance Research and Innovative Ideas in Education*, 2017, **3**(2), 476–483.
20. LIU, Y. ZHU, L. ZHANG, C. REN, F. HUANG, H, LIU, Z. Life cycle assessment of melange yarns from the manufacturer perspective. *The International Journal of Life Cycle Assessment,* 2019, **25**(3), 588-599, doi: 10.1007/s11367-019-01705-8.
21. MEMON, H. KHOSO, A. N. MEMON, S. Effect of dyeing parameters on physical properties of fibres. *International Journal of Applied Sciences and Engineering Research,* 2015, **4**(4), 401–407.
22. MOGHASSEM, Abdolrasool. Damaging of dyed cotton fibres with direct dye in spinning processes and its effect on the properties of cotton mélange yarn. *International Journal of Engineering – Transactions B: Applications,* 2007, **20**(2), 203–210.
23. KARBALAIKARIM, S. Karim, GHAREHAGHAJI, A.A., TAVANAIE, H. A study of the damage caused to dyed cotton fibres and its effects on the properties of rotor- and ring-spun melange yarns. *Fibres and Textiles in Eastern Europe*, 2007, 15, **3**(62), 63–67.
24. RAY, S., GHOSH, A., BANERJEE, D. Effect of blending methodologies on cotton mélange yarn quality. *Fibres and Textiles in Eastern Europe,* 2018, **26**(5), 41–46, doi: 10.5604/01.3001. 0012.2529.
25. HABIBA H. GONG, T., KALEEM, K. Real-time quality assessment of neppy mélange yarn manufacturing using macropixel analysis. *Tekstilec,* 2019, **62**(4), 242–247, doi: 10.14502/Tekstilec2019.62.242-247.

Tomasz Blachowicz[1], Tobias Böhm[2], Jacek Grzybowski[1], Krzysztof Domino[3], Andrea Ehrmann[2]
[1] Silesian University of Technology, Institute of Physics – Centre for Science and Education, 44-100 Gliwice, Poland
[2] Bielefeld University of Applied Sciences, Faculty of Engineering and Mathematics, 33619 Bielefeld, Germany
[3] Institute of Theoretical and Applied Informatics, Polish Academy of Sciences, 44-100 Gliwice, Poland

Analysis of AFM images of Nanofibre Mats for Automated Processing

Analiza slik AFM nanovlaknatih kopren za samodejno obdelavo

Original scientific article/*Izvirni znanstveni članek*
Received/*Prispelo* 4-2020 • Accepted/*Sprejeto* 5-2020

Abstract

The image processing of pictures from fibres and fibrous materials facilitates the investigation of diverse geometrical properties, such as yarn hairiness, fibre bifurcations or fibre lengths and diameters. Such irregular sample sets are naturally suitable to the statistical examination of images, using a random-walk algorithm. This results in the calculation of the so-called Hurst exponent, which is the asymptotic scaling exponent of the mean squared displacement of the walker's position. Previous investigations have proven the appropriateness of this method for examinations of different fibres, yarns and textile fabrics. In a recent study, we used AFM (atomic force microscopy) images, split into different greyscales, to analyse and quantify differences between various nanofibre mats created from polyacrylonitrile. In addition to the strong influence of the nanofibre diameters, a certain impact of the AFM settings was also seen and must be taken into account in future research.
Keywords: electrospinning, polyacrylonitrile (PAN), nanofibrous mat, atomic force microscopy (AFM), Hurst exponent, random walk

Izvleček

Obdelava slik vlaken in vlaknastih materialov omogoča raziskovanje različnih geometrijskih lastnosti, kot so kosmatost preje, bifurkacija vlaken ali dolžine in premera vlaken. Takšni vzorčni seti z nepravilnostmi so naravno primerni za statistični pregled slik z algoritmom slučajnega hoda. Pri tem izračunamo ti. Hurstov eksponent, ki je asimptotični skalirni eksponent srednjega kvadratnega premika položaja sprehajalca. Dosedanje raziskave so dokazale ustreznost metode za oceno različnih vlaken, prej in ploskovnih tekstilij. V nedavni študiji smo uporabili slike AFM (mikroskopije na atomsko silo), razdeljene glede na različne sive odtenke, za analizo in količinsko določitev razlik med različnimi nanovlaknatimi koprenami iz poliakrilonitrila. Poleg močnega vpliva premera nanovlaken je bil viden tudi določen vpliv nastavitev AFM, ki jih je potrebno upoštevati v prihodnjih raziskavah.
Ključne besede: elektropredenje, poliakrilonitril (PAN), nanovlaknata koprena, mikroskop na atomsko silo (AFM), Hurstov eksponent, slučajni hod

Corresponding author/*Korespondenčna avtorica:*
Prof. Dr. Dr. Andrea Ehrmann
E-mail: andrea.ehrmann@fh-bielefeld
ORCID: 0000-0003-0695-3905

Tekstilec, 2020, ***63****(2), 104-112*
DOI: 10.14502/Tekstilec2020.63.104-112

1 Introduction

Electrospinning can be used to prepare nanofibres or nanofibrous mats from diverse polymers or polymer blends [1–5], even in combination with metallic [6–8], semiconducting [9–11] or other nanoparticles. Subsequent thermal treatment can be used to stabilise the nanofibrous mats chemically [12–14], followed by carbonisation [15–17], or to use a calcination step instead to evaporate the polymer and sinter the residual inorganic material [9, 14, 18].

To describe such electrospun nanofibres or nanofibrous mats quantitatively, usually the fibre diameter distribution is given [19, 20], as well as the fibre orientation [21, 22]. There are, however, many more interesting parameters, e.g. the pore size or general porosity, which is sometimes measured by sophisticated instruments [23, 24], but hard to define from a microscopic image, even if the resolution is high enough. Such questions are also important, particularly for the application of such nanofibrous mats as filters [25, 26].

Using only high-resolution images as the basis for a quantitative description of a nanofibre mat may be possible by different mathematical methods. Some of them are the fractal dimension, which is often used as an indicator of the roughness of surface coatings or finishings [27] or for the detection of irregularities in the form of fabric defects [28–31], including the topothesy fractal dimension, which is less affected by scale variations and thus assumed to be a good instrument to measure surface roughness [32–34]. Other methods are calculations of the lacunarity, which describes spatial features of multifractal or non-fractal surfaces [35–37], or sometimes the succolarity, which measures the degree of percolation of an image [38, 39]. Another parameter that can be used is the so-called Hurst exponent. This value is calculated by performing random walks on the parts of an image where the sample is visible. This is how spatially adjacent areas of a sample in a certain image are defined. Hurst exponent evaluations of textile fabrics were performed by our group [40–42] and several other researchers [43].

In our previous investigations, we concentrated on microscopic images of knitted fabrics to evaluate fabric hairiness. This article presents a study of atomic force microscopy (AFM) images taken on different electrospun nanofibre mats, focusing mainly on the influence of the AFM control parameters on the resulting image and the corresponding Hurst exponents.

2 Materials and methods

Sample preparation

A needleless Nanospider Lab electrospinning machine (Elmarco Ltd., Liberec, Czech Republic) was used for sample preparation. The following spinning parameters were chosen: voltage of 80 kV (or 65 kV), nozzle diameter of 0.9 mm (or 1.5 mm), carriage speed of 200 mm/s, bottom electrode/substrate distance of 240 mm, ground electrode/substrate distance of 50 mm, chamber temperature of 22 °C, and relative humidity in the chamber of 32%. Electrospinning was performed using a polypropylene (PP) nonwoven as a substrate. The spinning solution contained 16% (or 20%) PAN (X-PAN, Dralon GmbH, Lingen, Germany), dissolved in dimethyl sulfoxide (DMSO, min. 99.9%, S3 Chemicals, Bad Oeynhausen, Germany).

Measurements

Investigations of the sample morphology were performed with an atomic force microscope (AFM, FlexAFM by Nanosurf, Liestal, Switzerland), using SHR 300 and TAP190Al-G AFM probes as cantilevers, which work in dynamic mode and have tip diameters of 1 nm and 20 nm, respectively. The AFM settings (proportional (P), integral (I), differential (D) control and setpoint) were either optimised to get a sharp image or, in the second part of the study, varied around the optimum. While P, I and D describe the values of a common PID controller, the setpoint defines the oscillation amplitude of the cantilever in the dynamic mode.

Random walk and Hurst exponent

In the simplest case, a colour image or, in the case of an AFM image, a greyscale image has to be transferred into a black-and-white image. Often the black parts define the sample area, while the white parts define the pores or the open areas between sample parts, e.g. between the yarns of a knitted fabric [40–42]. The black area can be more or less connected, depending on the sample under examination, starting from a completely black square as one extremum to tiny black spots as another extremum.

Next, a so-called random walk is performed on the black parts of the sample only. A random walk can be described as follows: an arbitrary pixel inside the black part of the sample is chosen. Then, a step in an arbitrary direction – one pixel left, right, up or

down – is performed, followed by another arbitrary step, etc. Finally, after a defined number of steps – e.g. 100, 1,000 or 10,000 – the distance between the original pixel and the final pixel (the displacement vector) is calculated.

If this process is repeated several times, the average displacement vector vanishes, since the final pixel will sometimes be located on the upper left of the original pixel, sometimes on the lower right, etc. What does not vanish, however, is the squared displacement vector. For a completely black square, i.e. a large area without any restrictions of the random walk path, the squared average displacement vector can be assumed to be proportional to the number of experiments n:

$$<\Delta r^2> = Cn \quad (1)$$

with the displacement r and a constant C, which is only necessary for mathematical reasons and has no physical relevance.

This formula must be modified as follows for a not completely black area, but rather a complex image with partly black areas, on which the random walk can be performed, and white areas that limit the possible walk directions, especially in fine black structures whose border must not be crossed:

$$<\Delta r^2> = Cn^{2h} \quad (2)$$

where h represents the aforementioned Hurst exponent (see for example [46] for some mathematical justifications).

Comparing both formulas, we see that for a completely black area h can be expected to be approximately 0.5 to make both formulas identical. For a fractured black area, the possible ways of the random walk are limited by the white areas in between, making the possible distance between the starting and ending points smaller and thus reducing h. Indeed, the values of h are reduced for smaller structures, especially for the aforementioned small black dots in a white matrix that do not allow for moving from one black dot to another, thus strongly limiting possible movements.

Such a random walk would result in a single value of the Hurst exponent. Since this is a statistical method, it makes sense to use more than one test. Typically, approximately 100–1,000 starting points on a given image are chosen on which random walks with 100, 10,000 or 1,000,000 steps are performed. In this way, a large number of Hurst exponents is calculated, resulting in a Hurst exponent distribution being characteristic for an image, as will be shown in the next section.

It should be mentioned that in this description we started by transforming an original image into a single black-and-white representation. This may, however, not always be sufficient. Here we will also discuss the possibility of splitting one original image into several grey-channel sub-images, for example, labelled with numbers between 0 (black) and 31 (white) representing 256 grey channels. Importantly, this is analogous to the analysis of multi-colour (multi-spectral) or hyper-spectral images, where various wavelengths are split into spectral channels.

It is worth mentioning that other image processing methods were not used as pretreatments of the AFM images. To exclude the possible influence of typical AFM image processing routines, using dedicated optimisation software, the original AFM images with line fit applied were used as the basis of this study. The influence of image processing with specific AFM software, especially for sharpening purposes, will be investigated in a future study.

3 Results and discussion

Figure 1 depicts an exemplary Hurst exponent distribution measured for a PAN nanofibre mat electrospun with a voltage of 65 kV. The area of investigation, as depicted in the orange inset, has a dimension of 25 μm × 25 μm. The second image shows the corresponding black-and-white image.

The relatively large Hurst exponent of $h \sim 0.43$ can be attributed to relatively large fibre areas, here defined as the *white* areas, while the black areas are correlated with borders between neighbouring fibres so that their evaluation would not be related to a physically meaningful property.

This number alone is not very meaningful, so we next tested how strongly Hurst exponents vary for completely different treatments. Figure 2 illustrates a surface showing broken polishing lines on a metallic coating (Figure 2a), as well as a lithography resist (Figure 2b) on atomically smooth substrates. The Hurst exponent distribution on the dark features in Figure 2a results in a smaller Hurst exponent due to the much narrower and additionally

fractured lines, but only with a small difference to the nanofibre image (Figure 1).

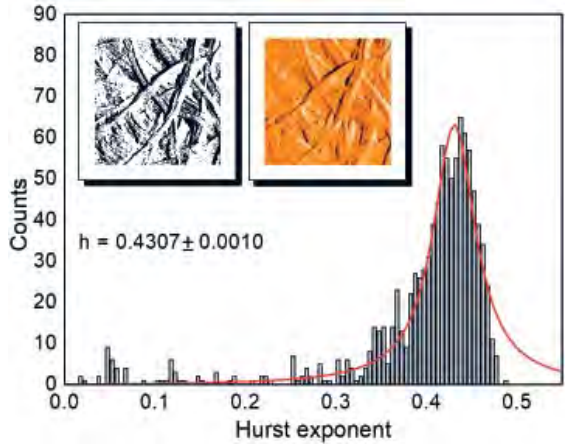

Figure 1: Hurst exponent distribution measured for a PAN nanofibre mat electrospun with a voltage of 65 kV, using a nozzle diameter of 0.9 mm and a polymer solution with 16% PAN. The insets show the original AFM amplitude image with line fit applied (orange), as well as the corresponding black-and-white image on whose white areas the Hurst exponent evaluation was performed. The red line is the Lorentz line fit to the distribution.

The Hurst exponent distribution calculated for the lithography resist (Figure 2b), on the other hand, shows large connected areas and thus suggests a larger Hurst exponent, which is clearly the case.
The standard deviations (cf. insets in Figures 1 and 2) are very small, as derived from Lorentz line fits to the obtained histograms, which are not symmetrical (non-Gaussian), since cases h > 0.5 are not expected in image processing analysis of this type. Thus, the presented results differ and allow for a quantitative differentiation between the different images. Nevertheless, the differences, especially between the nanofibre mat depicted in Figure 1 and the scratched substrate in Figure 2a, are not very clear due to the non-Gaussian character of the distributed data.
Figure 3 shows the results of a Hurst evaluation of another PAN nanofibre mat, this time produced with 20% PAN dissolved in DMSO, electrospun with a nozzle diameter of 1.5 mm using a voltage of 65 kV to obtain significantly thicker fibres, as visible

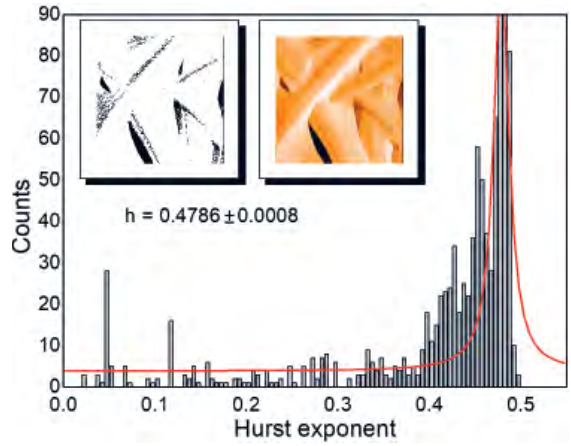

Figure 3: Hurst exponent distribution measured for a PAN nanofibre mat electrospun at 65 kV with 20% PAN through a nozzle of diameter 1.5 mm. The insets show the original AFM amplitude image with line fit applied (orange), as well as the corresponding black-and-white image on whose white areas the Hurst exponent evaluation was performed.

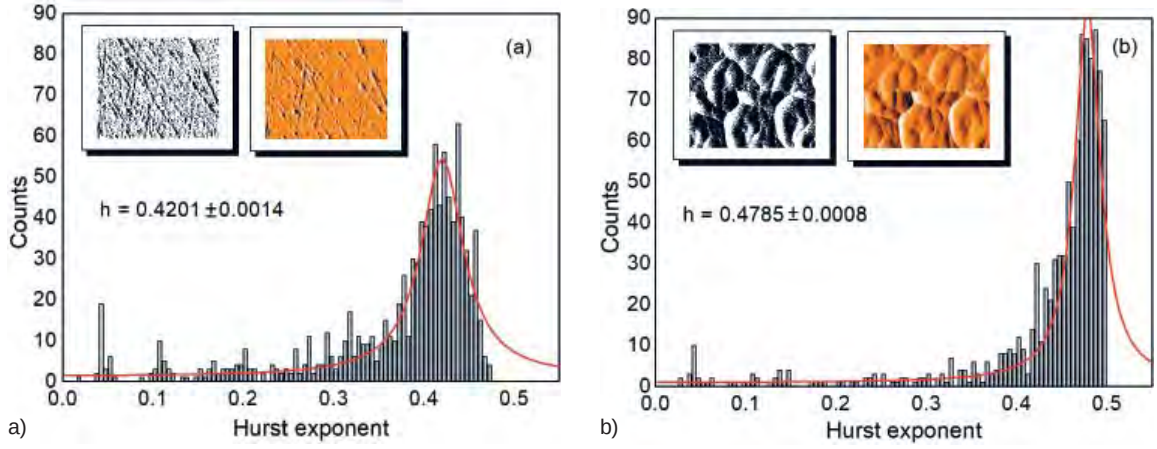

Figure 2: Hurst exponent distributions for (a) a substrate coated with Co and CoO thin films [44] and (b) positive lithography resist on a wafer [45]

Figure 4: Exemplary greyscale images in which black areas mark defined greyscale levels derived from the AFM image in Figure 3

in the inset image. Indeed, the Hurst exponent distribution of the *white* areas shows a clear difference to the one presented in Figure 1, which could be expected from the larger fibre areas. Nevertheless, the difference is less well visible than expected. In addition, the average Hurst exponent and standard deviation are nearly identical with those found in Figure 2b. This raises the question as to whether the Hurst exponent investigation can be expanded to obtain more information from a given image.

This is why in the next part of the study, the original AFM images were split into 32 sub-images, each containing eight grey levels, so that the whole greyscale from 0–255 was reduced to 32 sub-images. Figure 4 depicts a few of them, derived from the original AFM image given in Figure 3.

To depict the Hurst exponent distribution for a set of 32 sub-images, it would be necessary to show 32 histograms or alternatively one false-colour image. The false-colour images for the not empty greyscale channels of both nanofibre mat AFM images (Figure 1 and Figure 3, respectively) are shown in Figure 5. Here, white areas show zero counts; small numbers of counts are represented by pink/lilac/blue colours, while orange/red describes large counts.

Contrary to the previously shown single-scale Hurst exponent distributions, the differences between both multi-greyscale evaluations are clearly visible here. In both figures, there are areas with low Hurst exponents that seem to be separable and may represent some sort of small targets or artefacts on the original picture. Apparently, this method is also promising for providing a quantitative measure for AFM images of nanofibrous mats, as was shown earlier for knitted fabrics.

Here, however, we must address one problem that does not occur in common optical microscopic methods. As described in the section Materials and Methods, taking AFM images always necessitates the optimisation of typically four parameters, i.e. P, I, D and the setpoint. This optimisation is based on the experience and the personal preferences of the experimenter, i.e. it is to a large degree subjective.

Images were thus taken with P-values of 350, 450, 550, 650 and 750, I-values of 600, 900, 1,000, 1,100, and setpoints of 45% and 60%, while the D-value was kept constant here due to its small impact on the resulting images. Generally, changing the parameters resulted in shifting certain areas to other greyscale levels (not shown here), if evaluations

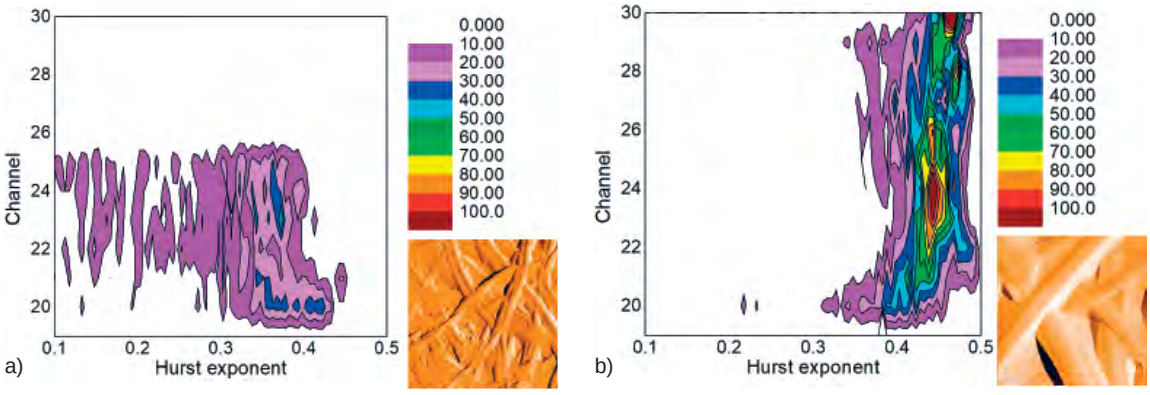

Figure 5: False-colour images of greyscale dependent Hurst exponent distributions obtained through the evaluation of inset AFM images

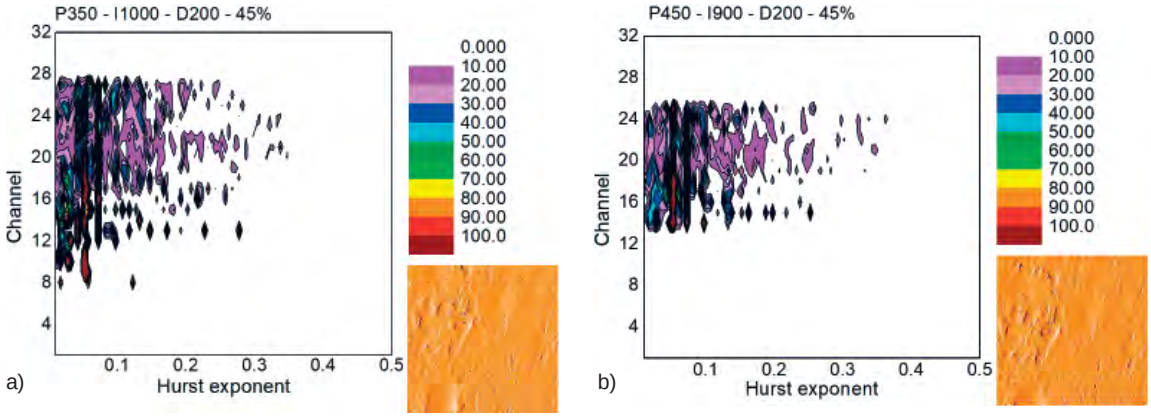

Figure 6: False-colour images of greyscale dependent Hurst exponent distributions obtained through the evaluation of inset AFM images taken with different parameters, as explained in the text. Electrospinning was performed at 80 kV, using a nozzle diameter of 0.9 mm and a polymer solution containing 16% PAN.

were performed on the amplitude (as used before), phase or z-axis. A comparison of two arbitrarily chosen images is presented in Figure 6.

As visible in this comparison, modifying the control parameters may extend or compress the greyscale range in which information about a sample surface can be found. While this must generally be taken into account, it is nevertheless in both cases possible to distinguish the new image clearly from both images shown in Figure 5 by comparing the greyscale dependent Hurst exponent distributions.

Next, a large set of samples and corresponding Hurst exponent evaluations is necessary to simplify this greyscale dependent evaluation, again without losing necessary information, with the ultimate aim of arriving at a quantitative description of an AFM image using a small set of numbers.

4 Conclusion and outlook

Atomic force microscopy images of electrospun nanofibre mats were evaluated for the first time by performing random walks on the fibre areas, as defined in black-and-white images, as well as on full sets of greyscale levels derived from the original images. While the first approach already showed differences between different nanofibre mats, it was insensitive to comparing fibrous and round structures. Much clearer differences between various AFM images were found in the greyscale dependent analysis.

Contrary to common optical microscopic images, AFM images always need settings applied by the user and are thus prone to subjective decisions of the experimenter. In the first tests applied here, Hurst exponent distributions calculated for different settings were found to be highly similar, while this point has to be taken into account during establishing an evaluation routine. In addition, future research is necessary on the impact of the common subsequent image processing step, which is also highly subjective and may cause additional deviations of the results, depending on the experimenter.

References

1. LIU, Yuyu, DENG, Lingli, ZHANG, Cen, FENG, Fengqin, ZHANG, Hui. Tunable physical properties of ethylcellulose/gelatin composite nanofibers by electrospinning. *Journal of Agricultural and Food Chemistry*, 2018, **66**(8), 1907–1915, doi: 10.1021/acs.jafc.7b06038.
2. BANNER, Jana, DAUTZENBERG, Maria, FELDHANS, Theresa, HOFMANN, Julia, PLÜMER, Pia, EHRMANN, Andrea. Water resistance and morphology of electrospun gelatin blended with citric acid and coconut oil. *Tekstilec,* 2018, **61**(2), 129–135, doi: 10.14502/Tekstilec2018.61.129-135.
3. DENG, Lingli, ZHANG, Xi, LI, Yang, QUE, Fei, KANG, Xuefan, LIU, Yuyu, FENG, Fengqin, ZHANG, Hui. Characterization of gelatin/zein nanofibers by hybrid electrospinning. *Food Hydrocolloids*, 2018, **75**, 72–80, doi: 10.1016/j.foodhyd.2017.09.011.

4. MAVER, Tina, KURECIC, Manja, PIVEC, Tanja, MAVER, Uros, GRADISNIK, Lidija, GASPARIC, Petra, KAKER, Barbara, BRATUSA, Ana, HRIBERNIK, Silvo, STANA KLEINSCHEK, Karin. Needleless electrospun carboxymethyl cellulose/polyethylene oxide mats with medicinal plant extracts for advanced wound care applications. *Cellulose*, 2020, **27**(8), 4487–4508, doi: 10.1007/s10570-020-03079-9.
5. SEDGHI, Roya, SHAABANI, Alireza, SAYYARI, Nastaran. Electrospun triazole-based chitosan nanofibers as a novel scaffold for bone tissue repair and regeneration. *Carbohydrate Polymers,* 2020, **230**, 115707, doi: 10.1016/j.carbpol.2019.115707.
6. SISAKOVA, K., ORINAK, A., ORINAKOVA, R., STRECKOVA, M., PATERA, J., WELLE, A.; KOSTECKA, Z., GIRMAN, V. Methane decomposition over modified carbon fibers as effective catalysts for hydrogen production. *Catalysis Letters,* 2020, **150**(3), 781–793, doi: 10.1007/s10562-019-02962-w.
7. FOKIN, Nadine, GROTHE, Timo, MAMUN, Al, TRABELSI, Marah, KLÖCKER, Michaela, SABANTINA, Lilia, DÖPKE, Christoph, BLACHOWICZ, Tomasz, HÜTTEN, Andreas, EHRMANN, Andrea. Magnetic properties of electrospun magnetic nanofiber mats after stabilization and carbonization. *Materials,* 2020, **13**(7), 1552, doi: 10.3390/ma13071552.
8. SHAN, Haoru, SI, Yang, YU, Jianyong, DING, Bin. Flexible, mesoporous, and monodispersed metallic cobalt-embedded inorganic nanofibrous membranes enable ultra-fast and high-efficiency killing of bacteria. *Chemical Engineering Journal,* 2020, **382**, 122909, doi: 10.1016/j.cej.2019.122909.
9. MEHRABI, Pouria, HUI, Justin, JANFAZA, Sajjad, O'BRIAN, Allen, TASNIM, Nishat, NAJJARAN, Homayoun, HOORFAR, Mina. Fabrication of SnO_2 composite nanofiber-based gas sensor using the electrospinning method for tetrahydrocannabinol (THC) detection. *Micromachines,* 2020, **11**(2), 190, doi: 10.3390/mi11020190.
10. BLACHOWICZ, Tomasz, EHRMANN, Andrea. Recent developments in electrospun ZnO nanofibers: a short review. *Journal of Engineered Fibers and Fabrics,* 2020, **15**, 1558925019899682, doi: 10.1177/1558925019899682.
11. SECUNDINO-SANCHEZ, O., DIAZ-REYES, J., SANCHEZ-RAMIREZ, J. F., MARTINEZ-JUAREZ, J. Stimulation of the photoluminescent properties of electrospinning TiO_2 nanofibres induced by structural modifications resulting from annealing at high temperatures. *Journal of Luminescence,* 2019, **215**, 116700, doi: 10.1016/j.jlumin.2019.116700.
12. LIU, Huichao, ZHANG, Shuo, YANG, Jinglong, JI, Muwei, YU, Jiali, WANG, Mingliang, CHAI, Xiaoyan, YANG, Bo, ZU, Caizhen, XU, Jian. Preparation, stabilization and carbonization of a novel polyacrylonitrile-based carbon fiber precursor. *Polymers,* 2019, **11**(7), 1150, doi: 10.3390/polym11071150.
13. SABANTINA, Lilia, BÖTTJER, Robin, WEHLAGE, Daria, GROTHE, Timo, KLÖCKER, Michaela, GARCÍA MATEOS, José, RODRÍGUEZ-MIRASOL, José, CORDERO, Tomás, EHRMANN, Andrea. Morphological study of stabilization and carbonization of polyacrylonitrile/TiO_2 nanofiber mats. *Journal of Engineered Fibers and Fabrics,* 2019, **14**, 1558925019862242, doi: 10.1177/1558925019862242.
14. GERGIN, Ilknur, ISMAR, Ezgi, SARAC, A. Sezai. Oxidative stabilization of polyacrylonitrile nanofibers and carbon nanofibers containing graphene oxide (GO): a spectroscopic and electrochemical study. *Beilstein Journal of Nanotechnology,* 2017, **8**, 1616–1628, doi: 10.3762/bjnano.8.161.
15. HECKOVA, M., STRECKOVA, M., ORINAKOVA, R., HOVANCOVA, J.L, GUBOOVA, A., SOPCAK, T., KOVALCIKOVA, A., PLESINGEROVA, B., MEDVED, D., SZABO, J., DUSZA, J. Porous carbon fibers for effective hydrogen evolution. *Applied Surface Science,* 2020, **506**, 144955, doi: 10.1016/j.apsusc.2019.144955.
16. DE OLIVEIRA, Juliana Bovi, MÜLLER GUERRINI, Lilia, CONEJO, Luiza dos Santos, REZENDE, Mirabel Cerqueira, BOTELHO, Edson Cocchieri. Viscoelastic evaluation of epoxy nanocomposite based on carbon nanofiber obtained from electrospinning processing. *Polymer Bulletin,* 2019, **76**(12), 6063–6076, doi: 10.1007/s00289-019-02707-0.
17. OJEDA-LOPEZ, Reyna, ESPARZA-SCHULZ, J. Marcos, Perez-Hermosillo, Isaac J., HERNANDEZ-GORDILLO, Armin, DOMINGUEZ-ORTIZ, Armando. Improve in CO_2 and CH_4

adsorption capacity on carbon microfibers synthesized by electrospinning of PAN. *Fibers*, 2019, **7**(10), 81, doi: 10.3390/fib7100081.
18. BLACHOWICZ, Tomasz, EHRMANN, Andrea. Conductive electrospun nanofiber mats. *Materials,* 2020, **13**(1), 152, doi: 10.3390/ma13010152.
19. NIKBAKHT, Mohammad, SALEHI, Majid, REZAYAT, Seyed Mahdi, MAJIDI, Reza Faridi. Various parameters in the preparation of chitosan/polyethylene oxide electrospun nanofibers containing Aloe vera extract for medical applications. *Nanomedicine Journal,* 2020, **7**(1), 21-28, doi: 10.22038/nmj.2020.07.03.
20. BIAN, Ye, WANG, Shijie, ZHANG, Li, CHEN, Chun. Influence of fiber diameter, filter thickness, and packing density on PM2.5 removal efficiency of electrospun nanofiber air filters for indoor applications. *Building and Environment,* 2020, **170**, 106628, doi: 10.1016/j.buildenv.2019.106628.
21. STORCK, Jan Lukas, GROTHE, Timo, MAMUN, Al, SABANTINA, Lilia, KLÖCKER, Michaela, BLACHOWICZ, Tomasz, EHRMANN, Andrea. Orientation of electrospun magnetic nanofibers near conductive areas. *Materials,* 2020, **13**(1), 47, doi: 10.3390/ma13010047.
22. BAZRAFSHAN, Zahra, STYLIOS, George K. Custom-built electrostatics and supplementary bonding in the design of reinforced Collagen-g-P (methyl methacrylate-co-ethyl acrylate)/nylon 66 core-shell fibers. *Journal of the Mechanical Behavior of Biomedial Materials*, 2018, **87**, 19-29, doi: 10.1016/j.jmbbm.2018.07.002.
23. CHEN, Yue, QIU, Linlin, MA, Xiangyu, DONG, Lika, JIN, Zhengfei, XIA, Guangbo, DU, Pingfan, XIONG, Jie. Electrospun cellulose polymer nanofiber membrane with flame resistance properties for lithium-ion batteries. *Carbohydrate Polymers,* 2020, **234**, 115907, doi: 10.1016/j.carbpol.2020.115907.
24. ZHENG, Gaofeng, JIANG, Jiaxin, WANG, Xiang, LI, Wenwang, LIU, Juan, FU, Gang, LIN, Liwei. Nanofiber membranes by multi-jet electrospinning arranged as arc-array with sheath gas for electrodialysis applications. *Materials & Design,* 2020, **189**, 108504, doi: 10.1016/j.matdes.2020.108504.
25. GAALOVA, Jana, YALCINKAYA, Fatma, CURINOVA, Petra, KOHOUT, Michal, YALCINKAYA, Baturalp, KOSTEJN, Martin, JIRSAK, Jan, STIBOR, Ivan, BARA, Jason E., VAN DER BRUGGEN, Bart, IZAK, Pavel. Separation of racemic compound by nanofibrous composite membranes with chiral selector. *Journal of Membrane Science,* 2020, **596**, 117728, doi: 10.1016/j.memsci.2019.117728.
26. YALCINKAYA, Fatma, BOYRAZ, Evren, MARYSKA, Jiri, KUCEROVA, Klara. A review on membrane technology and chemical surface modification for the oily wastewater treatment. *Materials,* 2020, **13**(2), 493, doi: 10.3390/ma13020493.
27. SRINIVASN, K., DASTOR, P. H., RADHAKRISHNAIAH, P., JAYARAMAN, S. FDAS: a knowledge-based frame detection work for analysis of defects in woven textile structures. *The Journal of the Textile Institute,* 1992, **83**(3), 431-448, doi: 10.1080/00405009208631217.
28. GIORGILLI, Antonio, CASATI, Danilo, SIRONI, Luisella, GALGANI, Luigi. An efficient procedure to compute fractal dimensions by box counting. *Physics Letters A,* 1986, **115**(5), 202-206, doi: 10.1016/0375-9601(86)90465-2.
29. CONCI, Aura, PROENCA, Claudia Belmiro. A fractal image analysis system for fabric inspection system based on box counting method. *Computer Networks and ISDN Systems,* 1998, **30**, 1887-1895, doi: 10.1016/S0169-7552(98)00211-6.
30. BU, Honggang, HUANG, Xiubao. A novel multiple fractal features extraction framework and its application to the detection of fabric defects. *The Journal of the Textile Institute,* 2008, **99**(5), 489-497, doi: 10.1080/00405000701692346.
31. BU, Honggang, WANG, Jun, HUANG, Xiubao. Fabric defects detection based on multiple fractal features and support vector data description. *Engineering Applications of Artificial Intelligence*, 2009, **22**(2), 224-235, doi: 10.1016/j.engappai.2008.05.006.
32. BLACKMORE, Denis, ZHOU, Jack G. A general fractal distribution function for rough surface profiles. *SIAM Journal on Applied Mathematics,* 1996, **56**(6), 1694-1719, 10.1137/S0036139995283122.
33. YANG, X.Z., PANG, G., YUNG, N. Discriminative fabric defect detection using adaptive wavelet. *Optical Engineering*, 2002, **41**(12), 3116-3126, doi: 10.1117/1.1517290.
34. HANMANDLU, Madau, CHOUDHURY, Dilip, DASH, Sujata. Detection of defects in fabrics using topothesy fractal dimension features. *Sig-*

nal Image and Video Processing, 2015**, 9**(7), 1521–1530; doi: 10.1007/s11760-013-0604-5.

35. PLOTNICK, Roy E., GARDNER, Robert H., HARGROVE, William W., PRESTEGAARD, Karen, PERLMUTTER, Martin. Lacunarity analysis: a general technique for the analysis of spatial patterns. *Physical Review E,* 1996, **53**(5), 5461–5468, doi: 10.1103/PhysRevE.53.5461.
36. CHUN, Hyen Chung, GIMÉNEZ, Daniel, YOON, Sung Won. Morphology, lacunarity and entropy of intra-aggregate pores: aggregate size and soil management effects. *Geoderma,* 2008, **146**(1-2), 83–93, doi: 10.1016/j.geoderma.2008.05.018.
37. QUAN, Yuhui, XU, Yong, SUN, Yuping, LUO, Yu. Lacunarity analysis on image patterns for texture classification. *IEEE Conference on Computer Vision and Pattern Recognition,* 2014, 160–167, doi: 10.1109/CVPR.2014.28.
38. DE MELO, R. H. C., CONCI, Aura. Succolarity: defining a method to calculate this fractal measure. *15th International Conference on Systems, Signals and Image Processing,* 2008, 10183147, doi: 10.1109/IWSSIP.2008.4604424.
39. VALOUS, Nektarios A., MENDOZA, Fernando, SUN, Da-Wen, & ALLEN, Paul. Texture appearance characterization of pre-sliced pork ham images using fractal metrics: Fourier analysis dimension and lacunarity. *Food Research International*, 2009, **42**(3), 353–362, doi: 10.1016/j.foodres.2008.12.012.
40. BLACHOWICZ, Tomasz, EHRMANN, Andrea, DOMINO, Krzysztof. Statistical analysis of digital images of periodic fibrous structures using generalized Hurst exponent distributions. *Physica A: Statistical Mechanics and its Applications,* 2016, **452**, 167–177, doi: 10.1016/j.physa.2016.02.013.
41. EHRMANN, Andrea, BLACHOWICZ, Tomasz, DOMINO, Krzysztof, AUMANN, Susanne, WEBER, Marcus O., ZGHIDI, Hafed. Examination of hairiness changes due to washing in knitted fabrics using a random walk approach. *Textile Research Journal*, 2015, **85**(20), 2147–2154, doi: 10.1177/0040517515581591.
42. EHRMANN, Andrea, BLACHOWICZ, Tomasz, ZGHIDI, Hafed, WEBER, Marcus O. Reliability of statistic evaluation of microscopic pictures taken from knitted fabrics. *Journal of Physics: Conference Series,* 2015, **633**, 012101, doi: 10.1088/1742-6596/633/1/012101.
43. LI, Jing, TENG, Honglei, LIU, Suqing, XU, Jing, LI, Tianduo. Three-dimensional spatial distribution analysis of fibre in wet-blue pig leather. *Journal of the Society of Leather Technologists and Chemists*, 2018, **102**(3), 111–117.
44. EHRMANN, Andrea, BLACHOWICZ, Tomasz. Angle and rotational direction dependent horizontal loop shift in epitaxial Co/CoO bilayers on MgO(100). *AIP Advances,* 2017, **7**(11), 115223, doi: 10.1063/1.4985032.
45. BLACHOWICZ, Tomasz, KOSMALSKA, Dorota, DÖPKE, Christoph, LEISTE, Harald, HAHN, Lothar, EHRMANN, Andrea. Varying steps in hysteresis loops of Co square nano-frames. *Journal of Magnetism and Magnetic Materials,* 2019, **491**, 165619, doi: j.jmmm.2019.165619.
46. HAVLIN, Shlomo; BEN-AVRAHAM, Daniel. Diffusion in disordered media. *Advances in physics*, 2002, **51**(1), 187–292, doi: 10.1080/00018730110116353.

Olena Kyzymchuk, Liudmyla Melnyk, Svitlana Arabuli
Kyiv National University of Technologies and Design, Department of Textile Technology and Design, Nemyrovycha-Danchenko str. 2, Kyiv, Ukraine

Study of Elastic Warp Knitted Bands: Production and Properties

Študija elastičnih snutkovnih pletenih trakov: izdelava in lastnosti

Original scientific article/*Izvirni znanstveni članek*
Received/*Prispelo* 4-2020 • Accepted/*Sprejeto* 5-2020

Abstract

Elastic fitted goods are identified as a separate group of medical textiles. This group includes elastic bandages, abdominal binders, posture correctors, corsets, recliners, etc. Elastic knitted bands are widely used in rehabilitation and prophylactic goods. This research studied the properties of elastic warp knitted bands that were made on an 18E gauge crochet machine. In order to reduce the product weight and to increase its comfort, a partial set (2-in/1-out) of elastomeric threads is used. This yarn is the main component of elastic fabric that affects stretch properties and end-use. In the warp knitted band, the polyurethane thread is usually used as longitudinal inlay yarn, which is located between the loop's overlap and underlap. In order to study the effect of polyurethane pre-elongation before knitting on band properties, seven pairs of gears were used and elongation was varied from 280% to 395%. The weft filling yarn connects the separate wales into the band. To prevent contact between polyurethane threads and the human body, the weft yarns were laid on both sides of the inlay yarn. The movements of weft guides were in opposite directions. In order to study the effect of weft yarn diameter on cover factor and bands properties, 2 ends, 4 ends or 6 ends of 16.7 tex polyester yarn were used to achieve corresponding overall linear densities of 33.4 tex, 66.8 tex and 100.2 tex. It was concluded that the partial drawing-in of the guide bar with polyurethane thread facilitated a reduction of up to 20% in the basis weight of the elastic band, while ensuring sufficient stretch properties. The impact of technological factors on the structural parameters and properties of the elastic band was established.

Keywords: elastic fabric, warp knitted band, elastomeric thread, stretch properties, guide bar drawing-in

Izvleček

Elastični izdelki so opredeljeni kot posebna skupina medicinskih tekstilij, v katero spadajo elastični povoji, trebušni pasovi, pasovi za pravilno držo, stezniki, počivalniki itd. Elastični pleteni trakovi se pogosto uporabljajo v izdelkih za rehabilitacijo in preventivo. V raziskavi so bile preučevane lastnosti elastičnih snutkovno pletenih trakov, izdelanih na kvačkalniku delitve 18E. Da bi zmanjšali maso izdelka in povečali njegovo udobje, je bil uporabljen delni vdev elastomernih osnovnih niti 2-vdeti/1-nevdeta osnovna nit). Elastomerna preja je bila glavni sestavni del elastičnega pletiva, ki vpliva na njegovo raztegljivost in končno rabo. V snutkovnem pletenem traku je poliuretanska preja običajno vzdolžno položena v zanko, nastalo med polaganjem niti na iglo in pod iglo. Za preučitev učinka predraztezka poliuretanske preje pred pletenjem na lastnosti traku je bilo uporabljenih sedem parov zobnikov, pri čemer se je raztezek spreminjal od 280 % do 395 %. Vložena votkovna preja je povezala ločene stolpce v trak. Da bi preprečili stik poliuretanskih niti s človeškim telesom, so bile votkovne preje vpletene na obeh straneh osnovne preje, položene v zanke. Polagalniki votkov so se gibali v nasprotnih smereh. Vpliv

Corresponding author/*Korespondenčna avtorica:*
Olena Kyzymchuk, Dr. Eng., Professor
E-mail: kyzymchuk.o@knutd.edu.ua
ORCID: 0000-0002-8874-8931

Tekstilec, 2020, ***63****(2), 113-123*
DOI: 10.14502/Tekstilec2020.63.113-123

premera votkovne preje na faktor kritja in lastnosti trakov je bil preučen z združevanjem 2, 4 ali 6 poliestrskih prej dolžinske mase 16,7 tex, s čimer so bile dosežene skupne dolžinske mase 33,4 tex, 66,8 tex in 100,2 tex. Ugotovljeno je bilo, da delno zatezanje poliuretanskih prej, vdetih v polagalnike, omogoča do 20-odstotno zmanjšanje osnovne mase elastičnega traku, hkrati pa zagotavlja zadostno raztegljivost. Ugotovljen je bil vpliv tehnoloških dejavnikov na strukturne parametre in lastnosti elastičnega traku.
Ključne besede: elastično pletivo, snutkovno pleteni trak, elastomerna nit, raztezne lastnosti, zatezanje niti v polagalnikih

1 Introduction

Compression garments are designed to provide fixed pressure to the human body. Such products are effective functional means in both therapy and the prevention of a number of diseases: varicose veins, the consequences of burns, post-surgery and post-traumatic edema, etc [1]. There are a number of requirements for compression garments and for materials for their production [2]. The two main requirements are: the stability of the product and the specified level of compression during use, as well as the guarantee of the product's comfort for consumers for the duration of use.

The necessary pressure on the human body is provided by fabric properties such as stretchability and elasticity, and by the product's construction: size and shape [3]. The elasticity of a knitted fabric is ensured by the incorporation of elastomeric thread [4] or corespun yarn with elastane core into the knitted structure as the filling yarn that is laid in the stretching direction [5]. High residual deformation and a significant change in linear dimensions after washing affect a product's size and the fabric structure. This also negatively affects the compression properties of products.

Elastic material contours to the human body and accumulates residual deformation in the most curved parts when a compression garment is used. Thus, unlike static loading, there is an increase in the part of residual deformations in certain areas of compression clothing and a change in the fabric structure with a corresponding increase in the stretchability of the material. This leads to a change in the properties and the deterioration of the product's appearance. The main factor in the changing shape and size of clothing, including compression garments, is thus the accumulation of cyclic residual deformation, as well as a change in the stitch density due to a change in the fabric thickness [6].

Scientists around the world are studying the structural parameters [7, 8] and properties [9] of elastic knitted fabric, in particular mechanical characteristics such as deformations [10], stretchability [11] and elasticity [12]. This indicate great interest in the problem and its relevance. The results of such studies can be used in the development and manufacture of new materials with improved properties [13].

When manufacturing clothes from elastic materials that fit tightly to the body, patterns are usually made smaller than ones from ordinary materials. At the same time, there is an important requirement to maintain conditions for normal blood circulation and other physiological processes in the human body. The maximum permissible pressure on the human body should not exceed 1330–2000 Pa [6]. At the section where clothes are tightly fitted to the body, the pressure level is directly proportional to the stress (σ) in the stretched fabric and inversely proportional to the radius of cross-section curvature (R) [14]. Thus, under the same load, the pressure of the fabrics with different elongation is different [15]. Garment pressure on the human body depends on the stresses that arise during fabric stretching. Thus, the study of the pressure of elastic fabric revealed its dependence on the knitting parameters and conditions of the product's use [16]. As a result of the two-factor experiment, it was determined that fabric pressure on the human body depends on the pre-elongation of the elastomer filament, and on the fabric elongation and surface curvature. Another study [17] attempted to investigate the influence of the inlay-yarn insertion density into a knitted structure and the area of a rigid element integrated into a knitted orthopaedic support on a compression generated by that support. It was concluded that the lower inlay-yarn insertion density and its total amount can be used for orthopaedic supports of lower compression class.

The design of compression products is usually based on an analysis of the experimental dependence of the distributed load (or voltage) on the relative deformation obtained, usually, at a constant rate of the

deformation (stretching diagrams) [13]. Therefore, the majority of studies on elastic materials involve the determination of their deformation properties using stretching diagrams, and using tests based on the load-unloading-relaxation cycle. An indirect approach for measuring pressure from a set of compression bandages and hosiery was developed by Cassandra Kwon et al. [18], from which rigidity (EI) values were determined, and tension–elongation curves and pressure-elongation data were calculated. The calculated pressure values were compared with PicoPress sensor readings measured on 10 participants. Results showed that the correlation between both approaches varied among bandage and hosiery samples.

However, during the use of compression products, the pressure on the body is not constant and decreases gradually to some equilibrium value. The authors [19] predicted the deformation properties of knitted fabric on the basis of a generalised Maxwell model. It was characterised by two average terms of relaxation and allowed the stress relaxation processes to be reliably simulated. Moreover, it allowed the dependence of the equilibrium stress component on the deformation to be predicted. The proposed method only needs the stress relaxation curve, which significantly reduces the test time. Ferdinand Tamoue et al. [20] concluded that the prediction of an applied pressure according to the modified Young-Laplace equation is realistic for both cotton-based and elastomer-based bandages. The main new findings were the utilisation of the specimen's stretched length for the prediction of the interface pressure in the modified equation, in contrast to the equation commonly found in literature, which uses the circumference of a randomly picked human subject's ankle to predict the pressure.

From the above-mentioned literature, the deformation properties of elastic textile materials are mostly determined on the one-cycle study by loading-unloading-relaxation [21]. As a result, the full deformation of the fabric and its components can be obtained, as well as the contents of elastic, plastic and residual deformations. There are several methods for determining the deformation characteristics of textile materials, which differ by the duration and conditions of the studies. The analysis of test methods of stretch properties of elastic fabric [22] allowed us to formulate recommendations on the efficiency of each.

The comfort characteristics of fabrics (particularly thermal insulation and permeability properties) are closely associated with changes in their structural parameters [23–26]. The evaluation of the air permeability of knitted fabrics containing elastane fibre applies both the standard method and a new approach based on fabric thickness measurement at different pressures [27]. Test results have shown that the air permeability of textile depends on their structure, fibre composition and porosity evaluated with regards to fabric thickness difference measured at different pressures [28]. The compressive behaviour of knitted elastic fabric affects excellence in comfort. It was found [29] that the stitch density (loop size) has a significant effect on the compressive load.

On the other hand, almost all research work examines elastic weft knitted fabrics, while only a few of them present study results of warp knitted fabric. The crocheting technique is widely used for elastic band production, but it is not sufficiently represented in scientific literature. Knitted fabric with elastomeric thread in each wale is usually used for rehabilitation products. It provides a high level of elasticity of the material and increases its density at the same time. The permeability of elastic knitted fabric can be increased by reducing the number of elastomeric yarns in its structure by not laying it in every course of weft knit and in every wale of a warp knit. However, this can lead to a decrease in elasticity and resilience. Thus, the purpose of this work was to study the structure and properties of elastic warp knitted bands with the partial threading of the guide bar by elastomeric threads.

2 Materials and methods

2.1 Sample production

All samples were produced on an 18E gauge LB-5000A crochet knitting machine made by Taiwan Giu Chun Ind. Co. Ltd. It was equipped with a heddle bar and 3-roller feeder for elastic threads or rubber.

The pillar stitch with closed loops (G1) from 16.7 tex polyester yarn was the ground interlooping of the studied fabrics (Figure 1). An elastomeric thread with a diameter of 0.8 mm was introduced into the knit structure as a longitudinal inlay yarn (G3). In order to reduce the product weight and to increase its permeability, the elastomeric filaments were

drawn according to the repeat: 2 in + 1 out, while 16.7 tex polyester yarn was also used as weft inlay yarn (G2 and G4). It was laid on both sides of fabric to ensure the connection of chains in the fabric and to cover the elastomer. To determine the effect of the weft in laid yarn thickness on the properties of the fabric and reliable covering of the elastomeric filament in the structure, 2 ends, 4 ends or 6 ends of the polyester yarn were used to achieve the resultant 33.4 tex, 66.8 tex and 100.2 tex weft yarn respectively (X1).

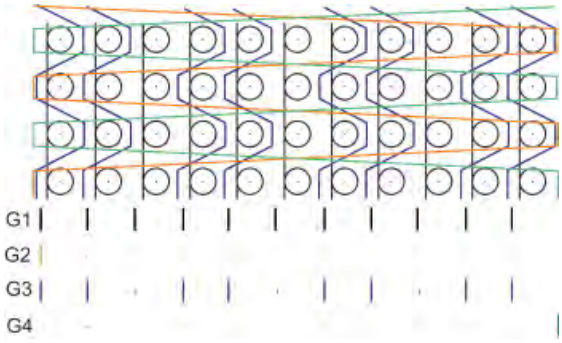

Figure 1: Lapping diagram

The parameters of the knitted structure and properties of the knitted fabric with elastomeric threads typically depend on its content. The elastomeric content can be limited by both the laying repeat and the degree of pre-elongation before entering the knitting zone [11, 30]. The preliminary elongation of the elastomeric filaments on the crochet machine is ensured by the ratio of the speed of the shafts' rotation in the feeding zone (Figure 2). In this study, it was varied by the number of gear teeth: leading z_1 – 27, 29, 31 and driven z_2 – 21, 23, 25, resulting in seven levels of the pre-elongation (X2) of the elastomeric filaments (Table 1). The gear combinations were chosen by taking into account the stability of the knitting and the quality of the knitted band. Other technological knitting conditions (tension of ground and weft threads, drawing-of force, etc.) were constant.

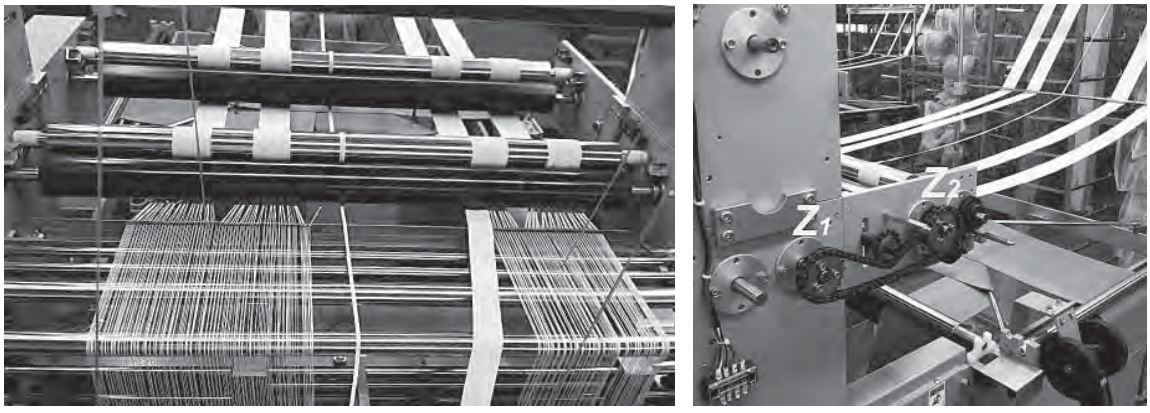

a) *b)*

Figure 2: Feeding of elastomeric thread on a crochet machine

Table 1: Production data

No.	Gearwheel		Pre-elongation of elastane (%)	Elastomer content in band with different weft yarn (%)		
	z_1	z_2		33.4 tex	66.8 tex	100.2 tex
1	27	21	280	51.4	41.5	35.1
2	27	23	300	49,0	39.8	34.8
3	27	25	330	47.4	37.6	32.8
4	29	23	330	47.7	38.2	32.2
5	29	25	365	45.4	35.8	32.1
6	31	23	360	45.3	36.5	30.5
7	31	25	395	44.7	36.5	28.7

2.2 Methodology

All knitted samples are conditioned by steaming and relaxing for 24 hours after knitting. Standard test methods were used to investigate the structural parameters of knitted materials [31–33]. Ten parallel measurements were done for each variant of elastic band.

The study of stretch properties of fabric was carried out on a relaxometer according to GOST 16218.9-89 [34] at a load of 25 N, which was selected by the number and diameter of elastomeric threads in the sample. Three parallel measurements were done for each variant of elastic band. The obtained results (Figure 3) showed a good convergence, which confirms their accuracy.

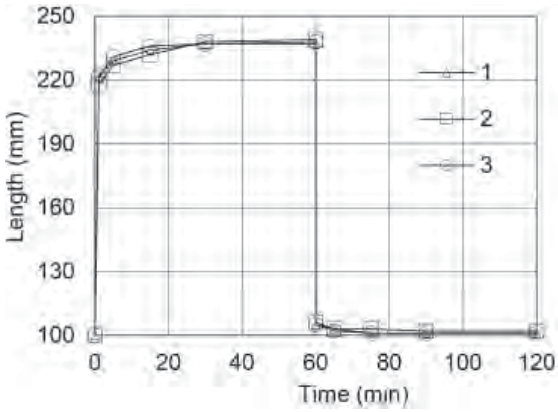

Figure 3: Dependence of a specimen's length on the cycling time for fabric #12

The studies of the coverage degree of the elastomeric threads by transverse weft threads were carried out by taking a photo of knitted samples at different elongation levels. A specimen was fixed in the clamps of a tensile testing machine; the camera was located to fix the middle part of the specimen. Stretching of the samples to a certain elongation (10%, 20%, 30% ... 100% was carried out at a constant speed (50 mm/min) of the lower clamp. The machine was stopped and a photo was taken.

3 Results and discussion

The structural parameters of elastic warp knitted bands are presented in Table 2 and in the graphs in Figures 4 and 5. It was observed that all studied knitted fabrics had two similar interdependent parameters: the number of wales per 100 mm, which was 74, and the length of the weft in-laying yarn per stitch of fabric, whose average value was 1.39 mm. For warp knitted fabric, these parameters mainly depend on the distance between needles, i.e. on the knitting machine gauge. Since all the samples were made on the same equipment, the values were unchanged.

The thickness of the knitted fabric was a function of the interlooping, as well as the number and diameter of the threads that were used for its production. Thus, in this study, it only depended on the linear density (33.4 tex, 66.8 tex or 100.2 tex) of the weft inlay yarn. The band thickness yields a mean value of 1.35 mm, 1.40 mm and 1.43 mm respectively.

The results also showed that the preliminary elongation of the elastomeric filament (X2) significantly affected its length per stitch (Figure 4.a). When pre-elongation was increased from 280% to 395%, the length of the elastomer thread per stitch decreased by 10%, regardless of the linear density of the transverse weft yarn. It should be noted that the parameter's value for warp knitted bands with a 33.4 tex weft yarn was 10% less than for the corresponding fabrics with 66.8 tex and 100.2 tex weft yarns. The X2 increase also led to some reduction of the length of the ground pillar stitch (Figure 4.b). This can be explained by the change in the stresses in the draw-off zone because the pulling load is the determining parameter of the loop length on a warp knitting machine. In this case, the trend was more pronounced for knitted fabric with 33.4 tex weft yarn where the observed value decreased by 10%, while the value decreased by only 5% for warp knitted bands with 66.8 tex weft yarn and was practically constant for bands with 100.2 tex weft yarn. These observations were influenced by the increasing contact area between the weft and the elastomer yarns arising from the increase in the frictional forces, which affected the degree of elastomer relaxation in the knitted structure.

The number of courses per 100 mm is an indicator that determines the fabric density vertically and depends on the loop height inversely, and therefore on the elastomeric thread length per stitch. The effects of the structural parameters are shown in Figure 5a. The index increased by increasing elastomeric thread pre-elongation and was larger for bands with 33.4 tex polyester as weft inlay yarn. This means that reducing the linear density of the weft threads reduced the number and size of its contact zones with the elastomeric filaments, which contributed to the elastomer shrinkage in the knitted structure and the increase in the stitch density.

Table 2: Structural parameters of elastic warp knitted band

No.	Initial factors		Density (per 10 cm)		Loop length (mm)			Thick-ness (mm)	Mass per unit area (g/m^2)
	Liner density of weft yarn (tex)	Pre-elon-gation of elastane (%)	Wales	Cours-es	Pillar stitch	Weft yarn	Elastomer		
1	33.4	280	74	213	5.69 ± 0.05	1.39	0.48 ± 0.02	1.34 ± 0.02	650.4 ± 1.3
2	33.4	300	74	228	5.80 ± 1.00	1.39	0.45 ± 0.01	1.34 ± 0.00	666.4 ± 1.6
3	33.4	330	74	242	5.77 ± 0.08	1.39	0.43 ± 0.01	1.37 ± 0.01	672.8 ± 1.5
4	33.4	330	74	244	5.57 ± 0.07	1.39	0.42 ± 0.01	1.34 ± 0.02	673.6 ± 1.4
5	33.4	365	74	259	5.73 ± 0.08	1.40	0.41 ± 0.00	1.35 ± 0.02	685.2 ± 1.8
6	33.4	360	74	264	5.51 ± 0.06	1.40	0.39 ± 0.00	1.37 ± 0.01	702.4 ± 1.5
7	33.4	395	74	271	5.28 ± 0.08	1.39	0.37 ± 0.00	1.35 ± 0.00	710.8 ± 1.7
8	66.8	280	74	200	5.86 ± 1.00	1.39	0.53 ± 0.02	1.40 ± 0.01	733.2 ± 2.0
9	66.8	300	74	213	5.92 ± 0.05	1.38	0.50 ± 0.02	1.40 ± 0.00	755.6 ± 2.0
10	66.8	330	74	215	5.64 ± 0.08	1.39	0.47 ± 0.01	1.40 ± 0.00	769.6 ± 1.8
11	66.8	330	74	216	5.68 ± 0.07	1.38	0.46 ± 0.01	1.41 ± 0.01	776.0 ± 2.1
12	66.8	365	74	226	5.66 ± 0.08	1.38	0.45 ± 0.01	1.41 ± 0.01	779.6 ± 1.9
13	66.8	360	74	228	5.58 ± 0.08	1.40	0.44 ± 0.01	1.41 ± 0.01	798.8 ± 2.0
14	66.8	395	74	232	5.66 ± 0.09	1.38	0.43 ± 0.00	1.40 ± 0.01	800.4 ± 1.8
15	100.2	280	74	180	5.68 ± 0.10	1.39	0.50 ± 0.01	1.43 ± 0.00	797.7 ± 2.0
16	100.2	300	74	180	5.70 ± 0.06	1.41	0.51 ± 0.02	1.43 ± 0.01	808.4 ± 2.1
17	100.2	330	74	188	5.54 ± 0.08	1.38	0.48 ± 0.02	1.43 ± 0.01	834.2 ± 1.9
18	100.2	330	74	196	5.73 ± 1.02	1.39	0.45 ± 0.01	1.42 ± 0.01	829.9 ± 2.0
19	100.2	365	74	192	5.46 ± 0.06	1.39	0.46 ± 0.01	1.42 ± 0.00	824.1 ± 2.1
20	100.2	360	74	200	5.62 ± 0.07	1.39	0.43 ± 0.00	1.43 ± 0.00	838.7 ± 1.9
21	100.2	395	74	208	5.64 ± 0.07	1.38	0.41 ± 0.00	1.42 ± 0.01	842.9 ± 2.2

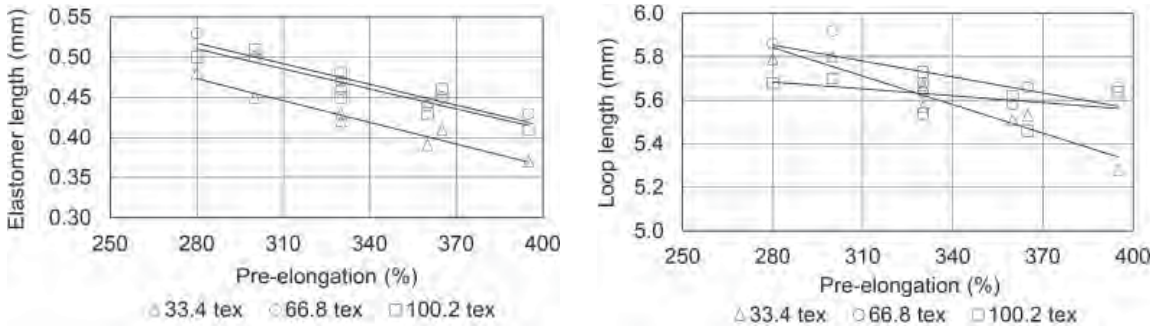

a) *b)*

Figure 4: Effect of pre-elongation ε of elastomeric threads on thread length: a) elastomeric thread per loop and b) pillar stitch

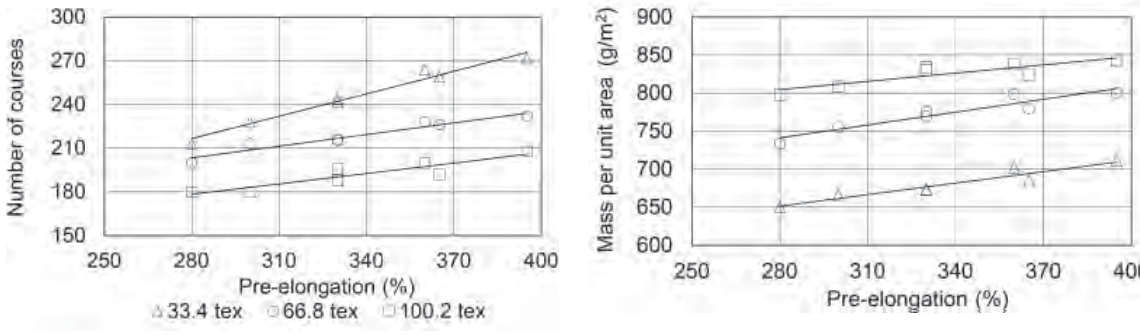

a) *b)*

Figure 5: Effect of pre-elongation ε of elastomeric threads on structure parameters: a) number of courses per 100 mm and b) mass per unit area

Table 3: Stretch characteristics of elastic warp knitted band

No.	Initial factors		Full deformation (%)	Deformation components (%)			Contributions		
	Liner density of weft yarn (tex)	Pre-elongation of elastane (%)		elastic, ε_1	plastic, ε_2	rezidual, ε_3	Δ_1	Δ_2	Δ_3
1	33.4	280	119.3	112.0	6.3	1.0	0.94	0.05	0.01
2	33.4	300	128.3	121.7	5.3	1.3	0.95	0.04	0.01
3	33.4	330	127.7	121.0	5.7	1.0	0.95	0.04	0.01
4	33.4	330	128.0	121.3	5.3	1.3	0.95	0.04	0.01
5	33.4	365	130.7	124.3	4.7	1.7	0.95	0.04	0.01
6	33.4	360	128.7	121.3	5.7	1.7	0.94	0.05	0.01
7	33.4	395	128.7	121.3	5.7	1.7	0.95	0.04	0.01
8	66.8	280	124.0	115.7	6.7	1.7	0.94	0.05	0.01
9	66.8	300	134.3	127.7	5.7	1.0	0.95	0.04	0.01
10	66.8	330	138.3	130.7	6.3	1.3	0.94	0.05	0.01
11	66.8	330	128.0	122.7	4.0	1.3	0.96	0.03	0.01
12	66.8	365	138.0	132.7	4.0	1.3	0.96	0.03	0.01
13	66.8	360	133.0	128.0	4.0	1.0	0.96	0.03	0.01
14	66.8	395	137.0	132.0	4.3	0.7	0.96	0.03	0.01
15	100.2	280	117.7	115.0	2.7	0.0	0.98	0.02	0.00
16	100.2	300	114.0	109.7	4.0	0.3	0.96	0.04	0.00
17	100.2	330	128.3	126.3	2.0	0.0	0.98	0.02	0.00
18	100.2	330	130.3	128.3	2.0	0.0	0.98	0.02	0.00
19	100.2	365	130.0	129.0	1.0	0.0	0.99	0.01	0.00
20	100.2	360	128.7	127.7	1.0	0.0	0.99	0.01	0.00
21	100.2	395	133.0	132.0	1.0	0.0	0.99	0.01	0.00

The mass per unit area of the fabric determines material consumption and the weight of the finished product. The developed warp knitted bands contain elastomeric threads that were laid according to repeat, which facilitated a reduction in their basic weight by 20% compared to the fabric with a full set of elastomeric threads [35].

The results (Figure 5b) demonstrated that the mass per unit area of the warp knitted band increased by 10% with double density (66.8 tex) weft threads and

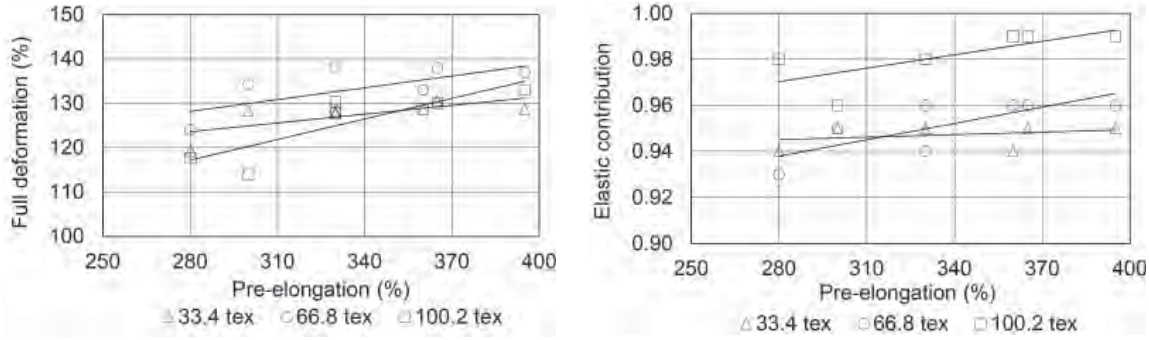

a) *b)*

Figure 6: Effect of pre-elongation ε of elastomeric threads on stretch properties: a) full deformation and b) elastic deformation contribution

by 17% with triple density (100.2 tex) weft threads. The mass per unit area of the warp knitted band increased by 5–7% with an increase in of the pre-elongation of the elastomeric threads, which was mainly due to the vertical increase of the stitch density.

An investigation of the stretchability of elastic warp knitted fabrics was carried out by stretching the band walewise, i.e. in the direction of the inlaid elastomeric filament. Three parallel measurements were performed for each variant. The obtained results showed a good convergence, which confirms their accuracy. The results of full deformation and its components calculations are presented in Table 3.

As a result, it was established that the full deformation of the elastic warp knitted band (Figure 6a) was from 115% to 140%, which facilitates their use in medical binders and other support products. The full deformation of the investigated variants was directly proportional to the pre-elongation of the elastomeric filaments. Increasing the linear density of the weft

Table 4: Samples photos within stretching

Fabric elongation (%)	Liner density of weft yarn (tex)		
	33.4	66.8	100.2
0			
20			
40		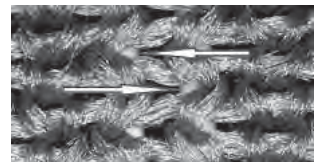	
60	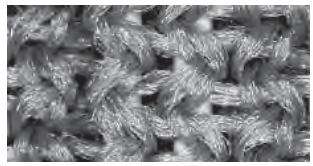	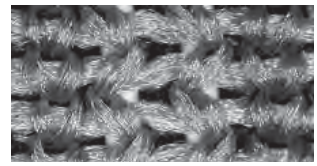	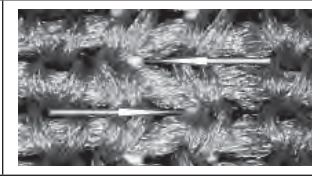

inlay yarn resulted in a slight (within 10%) decrease of deformation. The dependence of the full deformation on the pre-elongation of the elastomer filament can be expressed as ($R^2 = 0.8$): $\varepsilon f = 94.1 + 0.1\,\varepsilon$.

The elastic component of the full deformation of warp knitted band had the highest content (≥ 0.93). Its value increased with the pre-elongation level of the elastomeric filament (Figure 6b), which confirmed the conclusions made by the authors in a previous study [22]: increasing the pre-elongation of elastomeric yarn leads to an increase in the yarn strain. As a result, the relaxation processes in the fabric structure are faster. The knitted band with 33,4 tex weft threads demonstrated the smallest level of elastic deformation.

It should be noted that the residual deformation of the elastic warp knitted bands was insignificant (did not exceed 1.7%) and therefore will not affect the quality of the medical and prophylactic products for which this elastic fabric is designed. It is obvious that the residual component of full deformation was near zero for the elastic band with 100.2 tex weft threads.

When using elastomeric yarn without any wrapping, the comfort of the fabric may be degraded. An elastomeric yarn should not be placed at the surface of the knitted structure as in the initial state as well as in a stretched state. Studies of the coverage degree of the elastomeric threads by transverse weft threads were carried out by taking a photo of knitted samples at different elongation levels (Table 4). A specimen was fixed in the clamps of the tensile testing machine; the camera was located to fix the middle part of the specimen. Samples were stretched to a certain elongation (10%, 20%, 30% ... 100%) at a constant speed (50 mm/minute) of the lower clamp. The machine was stopped and a photo was taken. Obviously, at the initial state (elongation 0%), the transverse weft threads completely covered the elastomer, preventing it from reaching the surface in all samples. For samples with a 33.4 tex transverse weft thread, the elastomer was visible even at 20% elongation. For samples with a 100.2 tex, the transverse weft thread visibility of the elastomer was observed at 60% or higher elongation.

4 Conclusion

An elastic warp knitted band for use as a fixing element in rehabilitation and prophylactic products has been developed. It is proposed that the elastic thread should not be inlaid in every wale and the guide bar threaded according to repeat 2: 1 in order to reduce the material consumption and product's weight. This results in a 20% reduction in the mass per unit area of the warp knitted band, while maintaining relaxation characteristics within the relevant requirements for rehabilitation and prophylactic products. Based on the two-factor experiment planned and conducted in the work, the following was concluded:

- the linear density of the weft yarn (X1) affected the thickness, vertical density and surface density of the knitted material, and, to a lesser extent, the content of the elastic component in full deformation; and
- the pre-elongation of the elastomeric threads before the knitting zone had a significant effect on the vast majority of the investigated properties: an increase in pre-elongation from 280% to 395% which led to
- an increase in the number of courses per 100 mm by 15–27%, mass per unit area by 7–10% and full deformation and its elastic component by 15%, and
- a decrease in the length of the elastomer filament per stitch by 10%, as well as the residual component of the full deformation**.**

From the result of our studies, it was found that the use of 100.2 tex transverse weft threads guarantees full coverage of the elastomer within the elastic band's elongation of up to 60%. Despite the fact that there is 15–20% saving in material consumption and that fabrics satisfy the elasticity indices when using 33.4 tex transverse weft thread, their use is not recommended since even with an elongation of 20% there is the possibility of elastomeric threads making contact with the human body.

References

1. LIU, Rong, GUO, Xia, LAO, Terence T and LITTLE, Trevor. A critical review on compression textiles for compression therapy: textile-based compression interventions for chronic venous insufficiency. *Textile Research Journal,* 2017, **87**(9), 1121–1141, doi: 10.1177/0040517516646041.
2. MARINKINA, M., CHAGINA L., PROTALINSKIY C., BOGATYRIAVA M. To the question

of accounting for the stability of the load which is provided by compressive clothes during exploitation. *Proceeding of HEI. Textile Industry Technology,* 2015, **5**(359), 118–123.

3. MURALIENĖ Laima, MIKUČIONIENĖ Daiva, ANDZIUKEVIČIŪTĖ–JANKŪNIENĖ Akvilė, JANKAUSKAITĖ Virginija. Compression properties of knitted supports with silicone elements for scars treatment and new approach to compression evaluation. *IOP Conf. Series: Materials Science and Engineering,* 2019, 500, 012016, doi: 10.1088/1757-899X/500/1/012016.
4. PIVEC, T., SMOLE M. S., GAŠPARIČ P., KLEINSCHEK K. S. Polyurethanes for medical use. *Tekstilec*, 2017, **60**(3), 182–197, doi: 10.14502/Tekstilec2017.60.182-197.
5. KYZYMCHUK, O., MELNYK, L. Influence of miss knit repeat on parameters and properties of elasticized knitted fabric. *IOP Conf. Series: Materials Science and Engineering,* 2016, **141**, 012006, 1–7, doi: 10.1088/1757-899X/141/1/012006.
6. MAKSUDOV, N., NIGMATOVA F., YULDASHEV Zh., ABDUVALIEV R. Analysis of the deformation properties of high-elastic knitwear garments for designing sports clothes. *Universum: Technical Science : online scientific journal,* 2018, **9**(54).
7. PAVKO-CUDEN A. Parameters of compact single weft knitted structure (part 2): loop modules and munden constants – compact and supercompact structure. *Tekstilec*, 2010, **53**(10-12), 259–272.
8. PAVKO-CUDEN, A. Parameters of compact single weft knitted structure (part 3): fabric thickness and knapton constant. *Tekstilec*, 2011, **54**(1–3), 5–15.
9. FATKIĆ, Edin, GERŠAK, Jelka. Dimensional changes of single jersey weft knitted fabric with elastomer yarn consumption during relaxation process. *Tekstilec*, 2013, **56**(1), 22–33.
10. SULAR, V., OKUR, A. and OZCELIK, E. Cyclic deformation properties of knitted sportswear fabric by different test methods. *Industria Textila,* 2017, **68**(3), 176–185, doi: 10.35530/IT.068. 03.1330.
11. CHATTOPADHYAY, R., GUPTA, D., BERA, M. Effect of input tension of inlay yarn on the characteristics of knitted circular stretch fabrics and pressure generation. *The Journal of The Textile Institute*, 2012, **103**(6), 636–642, doi: 10.1080/00405000.2012.665237.
12. MAQSOOD, M., NAWAB, Y., UMAR, J., UMAIR, M. and SHAKER, K. Comparison of compression properties of stretchable knitted fabrics and bi-stretch woven fabrics for compression garments. *The Journal of The Textile Institute,* 2017, **108**(4), 522–527, doi: 10.1080/00405000.2016.1172432.
13. MAKLEWSKA, E., NAWROCKI, A., LEDWOŃ, J., KOWALSKI, K. Modelling and designing of knitted products used in compressive therapy. *Fibres and Textiles in Eastern Europe,* 2006, **14**(5), 111–113.
14. MYAZINA, U. Features of the deformation of knitted fabrics under technological and operational influences. *Proceeding of HEI. Textile Industry Technology,* 2008, **2**, 28–32.
15. JARIYAPUNYA, Nareerut, MUSILOVÁ, Blažena. Predictive modelling of compression garments for elastic fabric and the effects of pressure sensor thickness. *The Journal of The Textile Institute*, 2019, **110**(8), 1132–1140, doi: 10.1080/00405000.2018.1540285.
16. KYZYMCHUK, O., MELNYK, L., BOGUNOVA O. Investigation of pressure of elastic warp knitted fabric. *Herald of Khmelnytskyi National University. Technical Science,* 2019, **2**(271), 85–90, doi: 10.31891/2307-5732-2019-271-2-85-88.
17. MIKUCIONIENE, D. and MILASIUTE, L. Influence of knitted orthopaedic support construction on compression generated by the support. *Journal of Industrial Textile,* 2017, **47**(4), 551–566, doi: 10.1177/1528083716661205.
18. KWON, Cassandra, HEGARTY, Meghan, OXENHAM, William, THONEY-BARLETTA, Kristin, GRANT, Edward and REID, Lawrence. An indirect testing approach for characterizing pressure profiles of compression bandages and hosiery. *The Journal of The Textile Institute*, 2018, **109**(2), 256–267, doi: 10.1080/00405000.2017.1340079.
19. NADEZHNAYA, N., KUZNETSOV, A., CHARKOVSKIY, A. Prediction of the deformation properties of knitwear for compression products. *Vestnik of Vitebsk State Technological University,* 2013, **24**(1), 48–54.
20. TAMOUE, Ferdinand, EHRMANN, Andrea, and BLACHOWICZ, Tomasz. Predictability of sub-bandage pressure in compression therapy based on material properties. *Textile Research*

Journal, 2019, **89**(21–22), 4410–4424, doi: 10.1177/0040517519833969.
21. ŠAJN-GORJANC, D., PRAČEK, S. The prediction of elastic behavior of fabric from stretch yarn. *Industria Textila,* 2016, **67**(3), 157–163.
22. KYZYMCHUK, O., MELNYK, L. Stretch properties of elastic knitted fabric with pillar stitch. *Journal of Engineered Fibers and Fabrics,* 2018, **13**(4), 1–10, doi: 10.1177/1558925018820722.
23. OĞLAKCIOĞLU, N., MARMARALI, A. Thermal comfort properties of some knitted structures. *Fibres and Textiles in Eastern Europe,* 2007, **15**(5–6), 64–65.
24. VLASENKO, V., KOVTUN, S., BEREZNENKO, N., SUPRUN, N., MURAROVA, A. Water and heat transfer through multilayer textile composites. *Vlakna a Textil*, 2006, **13**(1–2), 29–32.
25. CELCAR, D., GERŠAK, J., MEINANDER, H. Evaluation of textile thermal properties and their combinations. *Tekstilec,* 2010, **53**(1–3), 9–32.
26. ONOFREI, E., ROCHA, A., CATARINO, A. The influence of knitted fabrics' structure on the thermal and moisture management properties. *Journal of Engineered Fibers and Fabrics,* 2011, **6**(4), 10–22, doi: 10.1177/155892501100600403.
27. DAUKANTIENE, V., VADEIKE, G. Evaluation of the air permeability of elastic knitted fabrics and their assemblies. *International Journal of Clothing Science and Technology,* 2018, **30**(6), 839–853. doi: 10.1108/IJCST-02-2018-0021.
28. UGBOLUE S. C. O. The air-permeability and bulk of plain-knitted fabrics. *The Journal of The Textile Institute*, 1975, **66**(8), 297–299, doi: 10.1080/00405007508630509.
29. PAZIREH, Ehsan, GHAREHAGHAJI, Ali Akbar, HAGHIGHAT, Ezzatollah. Study on the comfort of knitted elastic fabrics based on compressive deformation behavior. *Journal of Engineered Fibers and Fabrics,* 2014, **9**(4), doi: 10.1177/155892501400900410.
30. SADEK, R., EL-HOSSINI, A. M., ELDEEB, A. S., YASSEN, A. A. Effect of Lycra extension percent on single jersey knitted fabric properties. *Journal of Engineered Fibers and Fabrics,* 2012, **7**(2), 11–16, doi: 10.1177/155892501200700203.
31. ISO 23606 Textiles – knitted fabrics – representation and pattern design, 2009, 1–13.
32. ISO 3801 Textiles – woven fabrics – determination of mass per unit length and mass per unit area, 1977, 1–4.
33. ISO 5084 Textiles – Determination of thickness of textiles and textile products, 1996, 1–5.
34. Smallwares. Test methods at tension [online]. LinkedIn Corporation [accessed 12. 05. 2020]. Available on World Wide Web: <https://www.slideshare.net/normajodell/gost-162189-89>.
35. KYZYMCHUK, O., MELNYK, L., LIAKHOVA, V., HUBAR, I. Influence of technological parameters on the basis weight of elasticized fabric. *Bulletin of Kyiv National University of Technologies and Design. Technical Science,* 2017, **3**(110), 83–90.

Nuredin Muhammed, Nalankilli Govindan
Bahir Dar University, Ethiopian Institute of Textile and Fashion Technology, Textile Chemistry Research and Innovation Centre, 1037, Bahir Dar, Ethiopia

Chemical Modification of Cotton Cellulose by Carbamation with Urea and its Dyeability with Reactive Dyes without the use of Electrolytes

Kemična modifikacija bombaža s karbamiranjem s sečnino in njegova obarvljivost z reaktivnimi barvili brez uporabe elektrolita

Original scientific article/*Izvirni znanstveni članek*
Received/*Prispelo* 3-2020 • Accepted/*Sprejeto* 5-2020

Abstract

Cotton cellulose is primarily dyed with reactive dyes that form a strong covalent bond with the substrate. The reactive dyeing process requires a high amount of salt and alkali. Studies have been conducted to improve exhaustion and reduce the use of a high amount of salt and alkali through the cationisation of the substrate. This study focuses on the carbamation of mercerised cotton cellulose for the purpose of preparing an alternative way of dyeing cotton fabric with reactive dye in the absence of electrolytes. The effect of carbamation was shown qualitatively using FTIR spectroscopy where the optimal results were achieved using a urea concentration of 400 g/l, a temperature of 135 °C and a time of 5 minutes. The carbamated cotton demonstrated a lower decomposition temperature than that of native cotton. Colour strength, exhaustion, fixation and total dye utilisation studies demonstrated good results compared to the dyeing of conventional cotton fabric.

Keywords: cotton, carbamation, urea, pad-dry-cure technique, dyeing, Reactive Red HE3B, adsorption isotherm

Izvleček

Barvanje bombažne celuloze poteka večinoma z reaktivnimi barvili, ki tvorijo močno kovalentno vez s substratom. Proces barvanja z reaktivnim barvilom zahteva veliko količino soli in alkalij. Opravljene so bile raziskave s kationizacijo substrata za izboljšanje izčrpanja in zmanjšanje uporabe velikih količin soli in alkalij. Študija se osredotoča na karbamiranje mercerizirane bombažne celuloze z namenom priprave alternativnega načina barvanja bombažne tkanine z reaktivnim barvilom v odsotnosti elektrolita. Učinek karbamiranja je bil kvalitativno viden na spektrih FTIR, kjer so bili optimalni rezultati doseženi pri koncentraciji sečnine 400 g/l, temperaturi 135 °C in času 5 min. Karbamirani bombaž je imel nižjo temperaturo razgradnje od nemodificiranega bombaža. Jakost obarvanja, izčrpanje, fiksiranje in celotna uporaba barvil je pokazala dobre rezultate v primerjavi z barvanjem konvencionalne bombažne tkanine.

Ključne besede: bombaž, karbamiranje, sečnina, impregnirno-fiksirni postopek, barvanje, Reactive red HE3B, adsorpcijska izoterma

Corresponding author/Korespondenčni avtor:
Prof. Dr. Nalankilli Govindan
E-mail: gnalankilli@yahoo.com
Phone: +251 984624403
ORCID: 0000-0001-9836-0925

Tekstilec, 2020, ***63****(2), 124-137*
DOI: 10.14502/Tekstilec2020.63.124-137

1 Introduction

Cellulose is a chemically homogeneous linear polymer of up to 10,000 anhydroglucose units that are connected by β-1,4 bonds [1]. Each glucose unit is tilted by 180° towards its neighbour. The structural subunit of cellulose is cellobiose. Chemical uniformity facilitates the spontaneous crystallisation of cellulose molecules. Hydrogen bonding within and between multiple layers of parallel molecules results in the formation of tightly packed microfibrils. It has been reported that, in the manufacturing of cellulose carbamate, urea first decomposes into ammonia and isocyanic acid at approximately 135 °C [2], while Fu et al. reported that the decomposition of urea starts above its melting temperature of 132.7 °C [3]. Isocyanic acid (–HNCO–) reacts with cellulose hydroxyl (–OH) groups to form cellulose carbamate. The carbamate groups are substituted in the hydroxyl groups of the cellulose chain [4–7]. Reaction efficiency depends, *inter alia*, on the amount of urea, reaction conditions and raw material properties [8, 9]. The processes for synthesizing carbamated cellulose materials are explained in the following sections.

Solventless carbamation has been reported by heating (in an oven or oil bath) urea with a mercerised, carbamated cotton/cellulose (MCC) or alkali-swollen cotton linters in the temperature range of 110–185 °C for 3–9 hours, with an urea/cellulose weight ratio of 1.5–4.0, followed by microwave heating (255 W power) for 2–5 minutes [9]. Cellulose carbanilation performed through the reaction of cellulose, with phenyl isocyanate mostly in dimethyl sulfoxide (DMSO) or pyridine as the solvents, has been used widely for determining the analytical parameters of celluloses through gel permeation chromatography (GPC) in organic solvents, such as tetrahydrofuran (THF) or N,N-dimethylacetamide (DMAc) [10]. Carbanilation was performed using native cellulose or its alkali-activated counterpart. Many of these reactions start heterogeneously (suspension) and turn homogeneously. Hearon et al. carried out work through the suspension of cotton linters in refluxing pyridine, while reaction was conducted using phenyl isocyanate or a-naphthyl isocyanate to give the corresponding tricarbanilates. The reaction mixture became homogeneous after 36 and 40 hours, respectively. The CC was precipitated from the reaction mixture [11]. Cellulose tricarbanilate was obtained through the reaction of a suspension of biopolymer in DMF, using phenyl isocyanate in the presence of triethylenediamine as a catalyst at 95–100 °C. The suspension turned homogeneous within 30–60 minutes CC films were cast directly from the reaction mixture [12].

The reaction of cellulose with phenyl isocyanate in pyridine at 80 °C for 2 days produced a clear solution (MCC) or was incomplete (a pulp). The precipitation of CC in methanol resulted in the loss (5–26% (w/w)) of a low molecular weight fraction, while precipitation in water/methanol mixture (volume ratio 30/70) resulted in less [13] or no product fractionation [14]. Incomplete carbanilation of fibrous cellulose (bisulfite pulp; 86.3–97.1% α-cellulose; decrystallized cotton linters) was later avoided through the pretreatment (activation) of the biopolymer with liquid ammonia. The reaction was carried out for 2 days at 80 °C in pyridine, DMF or DMSO. Clear solutions of cellulose tricarbanilate were obtained in all cases [4].

Kenaf core cellulose was suspended in urea solutions [0.9–4.5% (w/w)] and the mixture was stirred under normal and then reduced pressure, the latter to enhance urea penetration within the biopolymer fibres. The reaction was induced by MW heating (380 W power) for 10–30 minutes. The N% in the purified CC increased as a function of increasing the urea concentration in the solution and the reaction time [15]. Cellulose derivatisation can be better controlled, and the reaction temperature reduced, e.g. to 100–130 °C, where an activated biopolymer was employed and carbanilation was carried out in the presence of a solvent. Another approach to obtaining CC under heterogeneous conditions is to use SC–CO_2 as a solvent to introduce urea into the biopolymer fibres [16]. The simplest approach to prepare CC under homogeneous conditions is to derivatise the hydroxyl groups of the AGU of a cellulose derivative. Cellulose tricarbamate from MCC, cotton linters, sulfate pulp, and cellulose obtained from wheat straw and hardwood by steam explosion was obtained through the reaction of phenyl isocyanate with the biopolymer dissolved in DMAc/LiCl for 2 hours, at 60–80 °C, in the presence or absence of a pyridine catalyst [14].

The conditions employed for carbamate formation under homogeneous conditions may lead to the formation of by-products [17, 18]. The formation of these by products was avoided by using anhydrous reaction conditions, a low reaction temperature

60–70 °C and a longer time period of 24–48 hours, and by using di(1-butyl) tin dilaurate as catalyst, a controlled amount of isocyanate (phenyl- and 1-butyl) and product workup that did not include quenching using an alcohol. The reaction of MCC, cotton linters or partially silylated cellulose in DMAc started heterogeneously and then turned homogeneously. Good to high yields (65–94%) of products with DS of carbamate from 1.74 to 3.0 were obtained [19]. Chemical modifications to cationise cotton have been reported to have beneficial effects in dyeing with reactive dyes [20–23].

In cellulose carbamate, the hydroxyl groups in the cellulose repeating unit are partially substituted with carbamate groups. The degree of substitution indicates the average amount of substituted hydroxyl groups per anhydroglucose unit. The theoretical maximum DS is thus 3.0 [2]. Properties that are affected most by the degree of substitution are solubility, swelling and plasticity. One of the key factors governing the substitution of the prepared cellulose carbamate is the amount of urea in the manufacturing process [24]. The nitrogen content of cellulosic material is often used to describe the substitution degree of cellulose carbamates. However, nitrogen content only indicates the amount of nitrogen in the sample, not the exact degree of substitution. Moreover, the uniformity of the product and the evenness of the carbamate groups in the cellulose chains are significant factors in determining cellulose carbamate quality and properties. However, researchers have reported that it is challenging to determine the uniformity of the substituted cellulose[11, 25]. Guo et al. and Yin et al. reported that the carbamate group is stable in acidic media, but that hydrolysis can take place in alkaline media. In alkaline media, the carbamate groups are irreversibly decomposed to carbonate and ammonia at a rate dependent on NaOH concentration and temperature [6, 17].

2 Materials and methods

2.1 Materials

Plain weave cotton fabric (half-bleached) with a warp density of 26 ends/cm, a weft density of 22 picks/cm, mass per unit area of 150 g/m^2, warp and weft-way tensile strength of 319N and 228N respectively, and a warp and weft yarn count of 50 tex (20 Ne) were used throughout the work. Urea extra pure (Loba Chemie Pvt. Ltd., India), which decomposes at temperature above its melting temperature as a source for isocyanic acid, sodium hydroxide pellets, which is a strong alkali for mercerising, sodium carbonate powder to fix the reactive dye to the fibre, acetic acid to neutralise the fabric after mercerising, sodium sulphate for exhaustion in the conventional reactive dyeing of cotton (Alpha Chemika, India) and reactive dye of the class of HE (Reactive Red HE3B) for dyeing were utilised throughout this study.

The following instruments were used in this study: Perkin Elmer TGA instruments to study the thermal decomposition properties of the carbamated material, a Perkin Elmer FTIR spectrometer to identify the molecular fingerprint of the carbamated fabric and a Tensolab 100 (Mesdan Lab, Italy) to evaluate the mechanical strength of the carbamated fabric. Also used were: a crock meter (Mesdan Lab, Italy) to evaluate the resistance to fading of the dyed carbamated fabric to dry or wet rubbing, a lightfastness solar box (Mesdan Lab, Italy) to evaluate the resistance to fading of the dyed carbamated fabric while exposed to light and Laundr-o-meter (Mesdan Lab, Italy) to evaluate the resistance to fading of the dyed carbamated fabric to wet washing. A Gretagmacbeth Colour Eye 310 was used to evaluate colour strength, while a UV/VIS spectrometer (Perkin Elmer Lambda 25, Singapore) was used to determine dye absorbance. The machines used in this study were an eco-IR dyeing machine for dyeing (Ahiba, US), a Padder Lab 300 (Mesdan Lab, Italy) for the application of treatments application to the mercerised fabric and an oven dryer (Mesdan Lab, Italy) for drying and curing purposes. The Kjeldahl method was used to determine the nitrogen content in the carbamated fabric to determine the degree of carbamation.

2.2 Methods

The experimental part of this study was divided into three main sections.

i. First, the carbamation of the cotton cellulose (i.e. the initial pre-treatment of half-bleached fabric through mercerization for the purpose of enhancing the accessibility of the functional groups in cotton cellulose) was carried out with the objective of optimisation. The main variables during the manufacturing of cotton cellulose carbamate were temperature, time and the concentration of

urea. The properties of the cotton cellulose carbamate were studied, with major responses being the degree of substitution and the tensile strength (warp and weft direction) of the fabric. The optimised fabric was analysed using FTIR to determine the molecular fingerprint of the product, while TGA studies were also performed.

ii. Secondly, the optimised carbamated and uncarbamated cotton was dyed using reactive dyes (i.e. Reactive Red HE3B dye). The properties of the dyed cotton cellulose carbamate were evaluated against the dyed uncarbamated cotton fabric. The tests carried out were: the degree of exhaustion, fixation, colour strength (K/S), fastness to washing, fastness to light and rubbing fastness.

iii. Thirdly, the modelling of an adsorption isotherm experiment was performed using Langmuir and Freundlich adsorption isotherms to find the best method to express the property of the carbamated cotton cellulose for dye adsorption.

Preparation of cellulose carbamate derivatives

a. Mercerisation

The mercerisation of half-bleached cotton fabric (i.e. sinking time < 3 seconds) was performed manually using a setup of a non-adjustable pan and frame. A piece of fabric was fixed to the pins of the steel frame with a tension of 3% and submerged into the concentrated (300 g/l) NaOH solution for 60 seconds with a mercerising temperature of 20–25 °C. The frame with the fabric still attached was then transferred to a sink and rinsed with running water to remove the majority of the alkali. After detaching the fabric from the frame, was rinsed, neutralised with dilute acetic acid, rinsed/washed with water and air dried. As an indicator of the degree of mercerisation, the barium number of the mercerised cotton fabrics was determined according to the AATCC test method 89-2003 [26].

b. Carbamation

The mercerised cotton fabric (barium activity number = 141.2 ± 1.0) was subjected to carbamation using 100 g/l, 250 g/l and 400 g/l amounts of urea by following pad-dry-cure method. The prepared cotton fabric was impregnated using a padding liquor in a laboratory padding mangle. The samples were then pre-dried for 5 minutes at 60 °C using an oven dryer, and then cured at 135 °C, 160 °C and 185 °C for 1, 3 and 5 minutes. The prepared carbamated samples were washed thoroughly with distilled water to purify them from the remains of urea and finally air dried.

The experiment and optimisation were carried out using the response surface methodology (i.e. three-level factorial), with the major responses being the degree of substitution of carbamate groups in place of hydroxyl groups, warp- and weft-way tensile strength.

Dyeing of uncarbamated and carbamated cotton

Dyeing of untreated (uncarbamated) and carbamated cotton fabrics was carried out using a laboratory eco-IR dyeing machine. Dyeing of uncarbamated cotton with Reactive Red HE3B (Figure 1) dye was performed according to the procedure recommended by the manufacturer, in which a shade (% o.w.f.) of Reactive Red HE3B (C.I. Reactive Red 120) dye was added to a room temperature dyebath. The fabric samples were then added and each bath was heated to 80 °C at a rate of 1.5 °C/minute. Before reaching 80°C, electrolyte (Na_2SO_4) of 40 g/l was added in two instalments at 55 °C and 65 °C to each bath. After holding the temperature at 80 °C for 10 minutes, 10 g/l of sodium carbonate was added. The bath was then held at 80 °C for 50 minutes, cooled to 60 °C at a rate of 2.5 °C/minute and then discarded (Figure 2 (a)) [27].

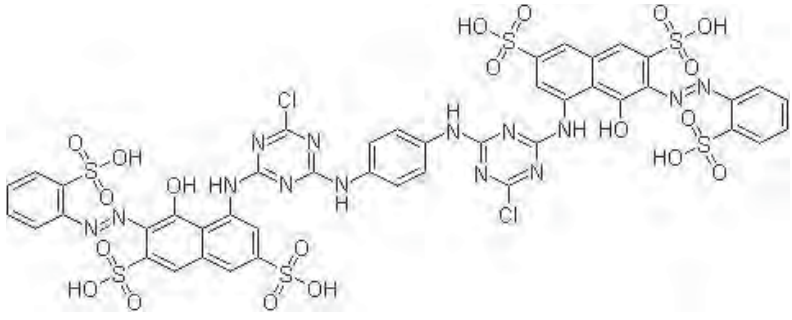

Figure 1: Reactive Red HE3B

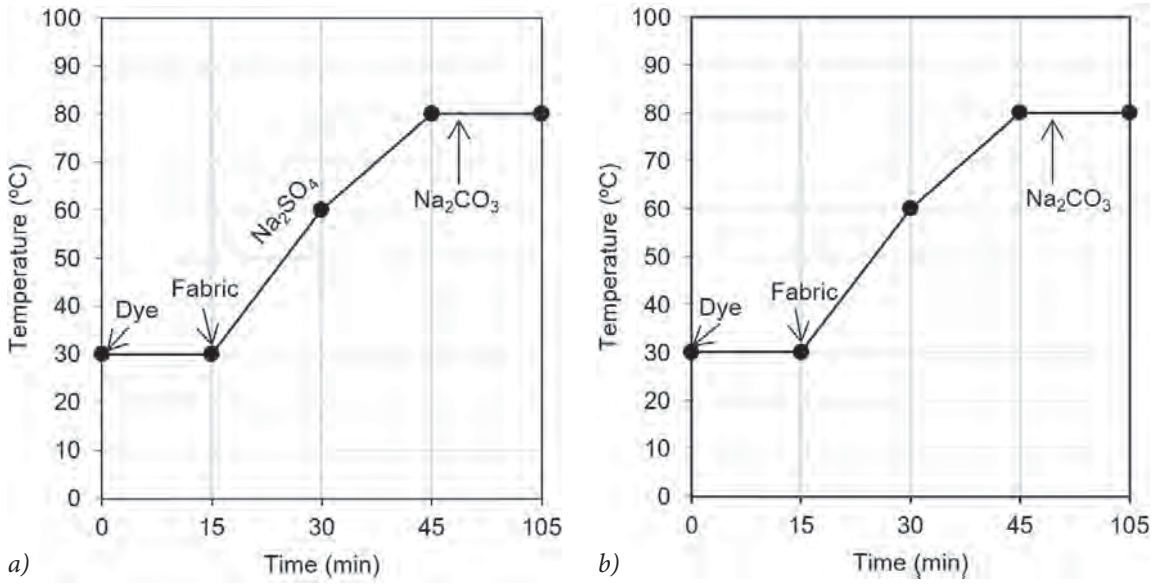

Figure 2: Dyeing cycle of (a) uncarbamated cotton fabric, (b) carbamated cotton fabric

The procedure for dyeing the carbamated cotton was the same as that for uncarbamated cotton, except that the dyeing of carbamated cotton was done in the absence of electrolytes (Na_2SO_4), with the bath buffered at pH 6 using acetic acid (Figure 2 (b)). Dye uptake of both the carbamated cotton without sodium sulphate and uncarbamated cotton with sodium sulphate, was measured by sampling the dye bath before and after the dyeing process. The absorbance of the diluted dye solution was measured at the wavelength of the maximum absorption (λ_{max} = 560) of the dye using a UV-visible spectrophotometer. Percent dye bath exhaustion E% was determined using equation 1.

$$E = 100\left(1 - \frac{A_1}{A_0}\right)\ (\%) \qquad (1),$$

where A_0 represents the absorbance of the dye solution before dyeing and A_1 represents the absorbance of the dye solution after dyeing. The colour strength of the dyed samples was determined as the *K/S* value calculated from the sample reflectance (*R*) (equation 2):

$$\frac{K}{S} = \frac{(1 - R)^2}{2R} \qquad (2)$$

The extent of the dye fixation of the reactive dyes on all the carbamated and uncarbamated cotton fabrics were determined using measurements of the *K/S* values of the dyed samples taken before and after soaping, from which the extent of dye fixation was calculated using equation 3 and 4.

$$F = \frac{C_2}{C_1}\ 100\ (\%) \qquad (3),$$

$$T = E\ \frac{C_2}{C_1}\ (\%) \qquad (4),$$

where *T* represents total dye fixed (%), C_1 represents the *K/S* value of dyed sample before soaping, C_2 represents the *K/S* value of dyed sample after soaping and *F* represents the degree of fixation of absorbed dye.

Determination of the degree of substitution

The percentage of nitrogen present in the cotton fabric was measured in duplicate and used as an indicator of the level of carbamation. The analysis was conducted according to the Kjeldahl method using a sample mass of 10 mg ± 2 mg.

The degree of substitution (DS) was determined using equation 5 below:

$$DS = \frac{162 \times N}{(14 \times 100) - (43 \times \mathrm{N})} \qquad (5),$$

where *N* represents specimen nitrogen content (%), 162 represents the molar mass (g/mol) of an anhydroglucose unit (AGU), 14 represents the molar mass of nitrogen (g/mol) and 43 represents the net increment in molar mass (g/mol) of an AGU on

substitution of a hydroxyl (–OH) by a carbamate ($–OCONH_2$) group.

Tensile strength and fastness testing

Tensile strength was tested according to the ASTM D5034 textile grab method [28], colourfastness to laundering according to the AATCC test method 61-2007 [26], colourfastness to light in accordance with the ISO 105-B02:1994, and colourfastness to rubbing in accordance with the AATCC test method 8-2007 (AATCC, 2010).

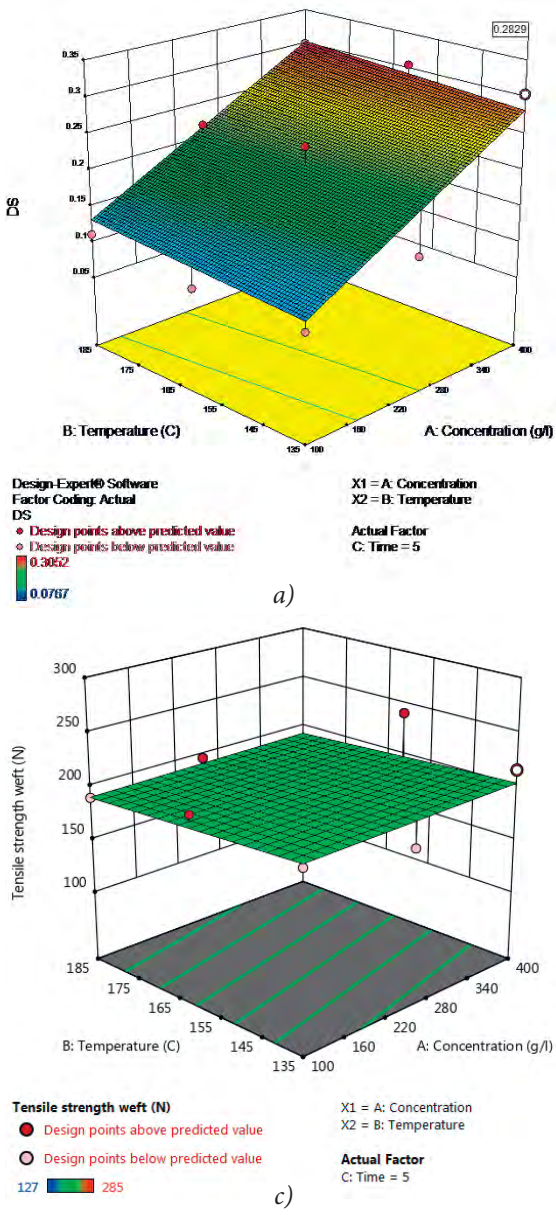

Figure 3: Response for (a) optimum carbamation, (b) weft-way tensile strength and (c) warp-way tensile strength

3 Results and discussion

3.1 Optimisation of the carbamation

The response surface methodology (RSM) was used to evaluate the degree of the carbamate group that has been substituted in place of the hydroxyl group of cotton cellulose, with less effect on the weft- and warp-way tensile strength. The design was also used to study the relationship between the variables (urea concentration, curing temperature and curing time) and the responses (degree of substitution and tensile

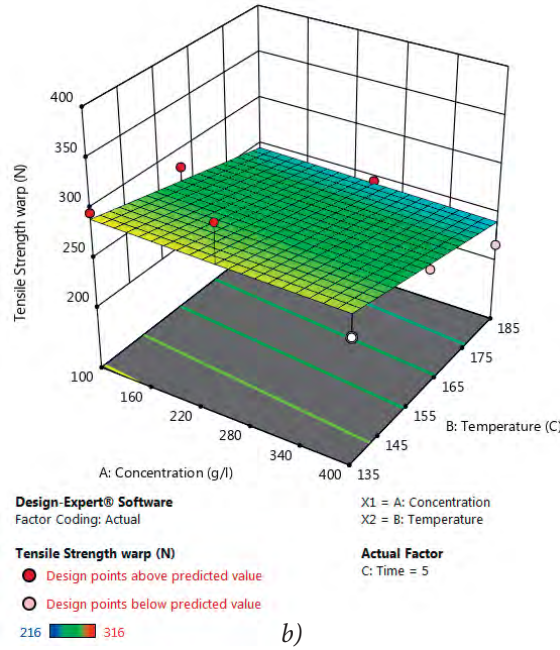

strength). Analysis of variance (ANOVA) was used to test whether the variables (urea concentration, curing temperature and curing time) significantly affect the response values (degree of substitution, warp-way tensile strength and weft-way tensile strength). The results are presented in Figure 3.

The effects of the factors are concentration, curing temperature and curing time, while responses are the degree of substitution, DS and tensile strength. It could be understood from the results that DS increased significantly by increasing the concentration of urea and increasing time, while there was no significant change in DS due to the varying of temperature. Tensile strength in the warp direction was affected significantly by increasing the temperature, while there was no significant change due to increment in concentration and curing time. Tensile strength in the weft direction was affected significantly by all the factors (concentration, temperature

and time). The desired results were found to be: DS of 0.283, tensile strength in warp of 285.98 N and weft of 203.82 N. Under these conditions, the warp tensile strength decreased by 10.35%, while the weft tensile strength decreased by 10.61% relative to the control half-bleached fabric.

3.2 FTIR analysis

Bands due to the stretching of OH groups of crystalline and amorphous modifications of cellulose in terms of celluloses I and II on account of mercerisation and carbamation have been reported in literature [3, 31]. Because the properties of cotton cellulose carbamate material are one of the significant factors that contribute to the dyeability of material, differences between the mercerised cotton cellulose carbamate sample and mercerised, uncarbamated cotton were evaluated to understand the chemical change that took place in carbamation (Figure 4). Carbamates of cotton cellulose were characterised by means of FTIR to confirm the reaction of hydroxyl groups with urea. A typical loss in the transmittance band for the carbamated cotton was observed in the range of 3600 cm^{-1} to 3300 cm^{-1}, which is assigned to the ($-NH_2$) [31] of the carbamate group. The stretch is not as broad or strong as it appeared in the uncarbamated cotton (–OH stretch) in this region. The transmittance band from 3300 cm^{-1} to 3000 cm^{-1} is very broad in the uncarbamated cotton, which indicates the large numbers of –OH groups in the cotton [3, 31], while this band is not as broad in the carbamated cotton, which indicates a reduction in –OH groups that are replaced by the carbamate group.

The transmittance peak at around 1100 cm^{-1} observed on uncarbamated cotton disappeared on the carbamated cotton. This can be attributed to the loss of –OH vibration in the carbamated cotton fabric. The reduction of hydroxyl peak at 3250 cm^{-1} represents strong evidence for the reaction of urea with the cotton samples.

3.3 Thermogravimetric analysis

The TG curves of the mercerised cotton cellulose and its carbamate derivatives with DS of 0.2829 are shown in the Figure 5. The TG curves were separated into three sections. At the initial stage, the weight loss observed in the temperature range of 100 °C to 150 °C could be attributed to the evaporation of water and gas absorbed by the cellulose. In the range of 150 °C to 250 °C, there appeared a minor thermal decomposition of residues. In the TG curves, it was found that all the major decompositions are located in the range of 300 °C to 400 °C and 300 °C to 375 °C for control cotton cellulose and carbamated cotton cellulose, respectively. When comparing the samples, it was discovered that the major decomposition temperature of control cotton fabric was higher than carbamated cotton cellulose. From the FTIR (Figure 4), it was observed that the carbamation of cotton showed the diminished intensity of hydrogen bonding in the range of 3600 cm^{-1} to 3300 cm^{-1}, as the decrease in intensity had a visible effect on

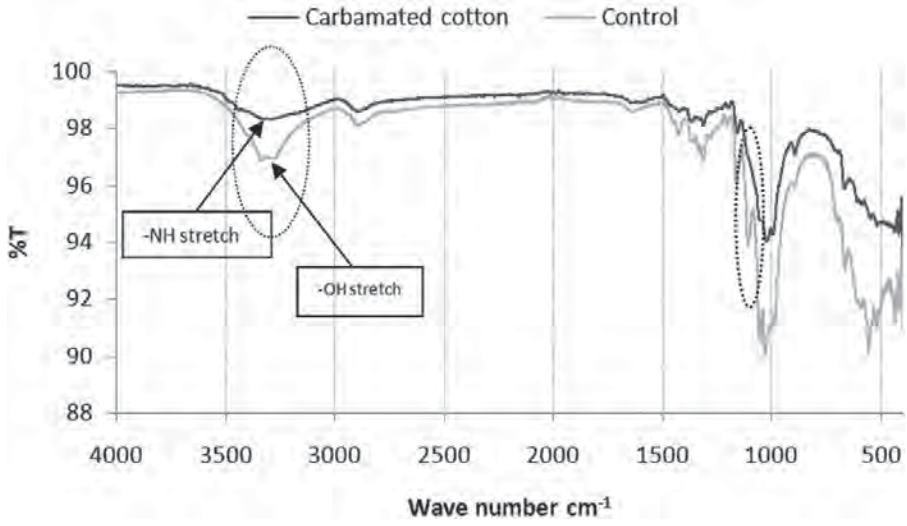

Figure. 4: FTIR spectra of carbamated and control fabric

the TG curve (Figure 5) and on the decomposition temperature of the materials.

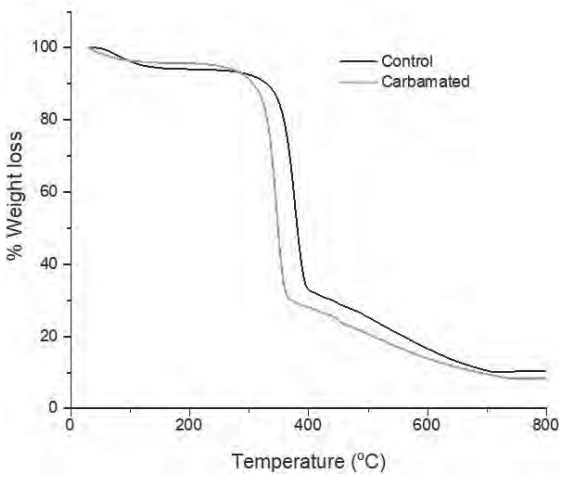

Figure 5: TG curves of cotton cellulose and carbamated cotton

3.4 Dyeing results

Exhaustion, fixation and dye utilised

The results of exhaustion, fixation and dye utilised are presented in Table 1. Exhaustion was determined by measuring the absorbance of the dye bath before and after the dyeing process at the wave length of maximum absorption (λ_{max} = 543 nm). The exhaustion percentage of the carbamated and mercerised cotton was higher than that of the control half-bleached fabric. For all fabrics, the exhaustion decreased by increasing the initial dye bath concentration. This can be attributed to the increment in affinity of the dye to the fibre. The dye utilisation of Reactive Red HE3B on all the control, mercerised and carbamated samples decreased by increasing the dye bath concentration. The exhaustion and dye utilisation are presented in Figures 6 and 7. The change percentage in dye utilisation was 12%, 13%, 7%, 15%, 14% and 10% for the shade depths of 0.5%, 1%, 2%, 3%, 4% and 5%, respectively, between the control and carbamated fabric.

Table 1: Summary of the dyeing properties of Reactive Red HE3B for carbamated, mercerised and control samples

Shade (%)	Absorbance of dye solution before dyeing (A_1)	Material type	Absorbance of dye solution after dyeing (A_2)	K/S value		Exhaustion (%)	Fixation (%)	Total dye utilised (%)
				Before washing (C1)	After washing (C2)			
0.5	6.2	T[a)]	0.80	3.80	3.44	87.10	90.48	78.81
		UT[b)]	1.30	1.38	1.21	79.03	87.51	69.16
		M[c)]	0.90	3.90	3.50	85.48	89.74	76.72
1	8	T	1.90	5.27	4.78	76.25	90.58	69.06
		UT	2.80	2.02	1.88	65.00	92.93	60.40
		M	2.10	5.34	4.54	73.75	85.08	62.75
2	8.7	T	3.40	6.98	6.48	60.92	92.90	56.59
		UT	3.80	2.30	2.14	56.32	93.14	52.46
		M	3.50	7.17	6.83	59.77	95.29	56.96
3	9.3	T	4.10	7.59	7.19	55.91	94.68	52.94
		UT	4.70	3.39	3.07	49.46	90.59	44.81
		M	5.00	7.46	7.08	51.46	94.84	48.80
4	9.9	T	5.60	7.89	7.25	43.43	91.90	39.92
		UT	6.20	3.93	3.62	37.37	92.15	34.44
		M	7.54	7.68	7.35	36.64	95.70	35.06
5	10.8	T	6.30	8.00	7.37	41.67	92.07	38.36
		UT	6.80	4.38	4.09	37.04	93.43	34.60
		M	8.23	7.91	7.35	35.70	92.92	33.18

[a)]carbamated, [b)]control half-bleached fabric, [c)]mercerised fabric

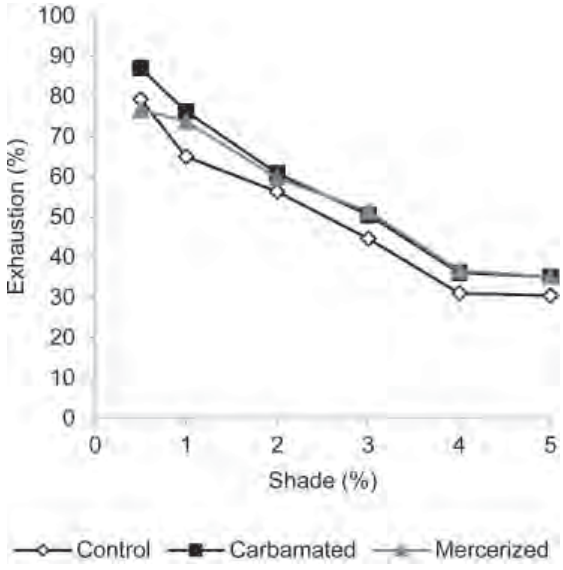

Figure 6: Percent exhaustion of Reactive Red HE3B on carbamated, mercerised and control fabric

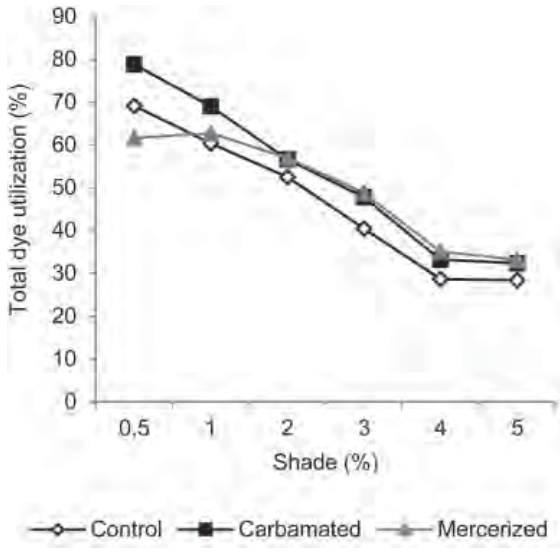

Figure 7: Total dye utilisation of carbamated, mercerised and control samples

Colour intensities (*K/S*) were employed to express the reduction ratio of light owing to absorption and scattering achieved based on reflectance. Figure 8 shows that the colour strength of the carbamated cotton dyed without sodium sulphate was much higher than that of the control half-bleached fabric. The carbamated cotton cellulose fabric was dyed with Reactive Red HE3B without using electrolytes; pH was instead made slightly acidic (pH = 6) through the addition of acetic acid. The improved dye uptake of carbamated cotton fabric may be attributed to the generation of positive charges, while the treatment fabric before carbamation (i.e. caustic mercerised) could also affect the dye adsorption, with the carbamate groups introduced. Very good levelling on the carbamated cotton cellulose samples was visually confirmed in this study.

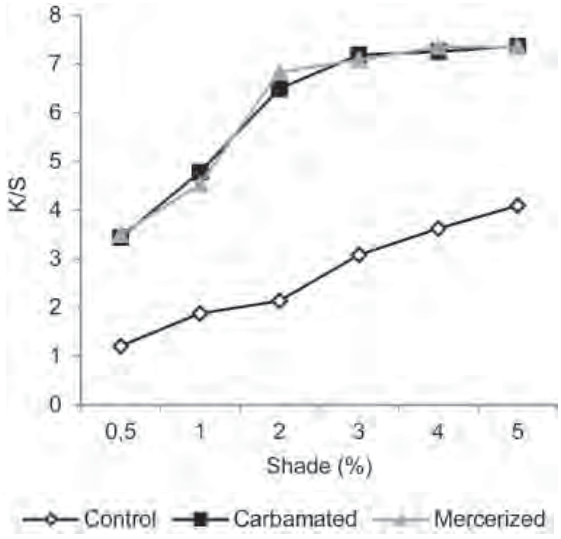

Figure 8: K/S values of carbamated, mercerised and control dyed samples

In the dyeing of carbamated cotton samples using an acid bath, it was confirmed that there was a strong attraction between the cationic dye sites on the carbamated cotton and the anionic Reactive Red HE3B dyes, which led to the achievement of higher exhaustion rates, without the addition of electrolytes to the dye bath. An enhancement of the colour strength is expected when the dye concentration is increased, as a greater number of dye molecules would be available in the vicinity of the cotton cellulose at higher concentrations. Unlike uncarbamated cotton, however, the dye build-up on the carbamated cotton is limited by its saturation adsorption value, which could be related to the amount of nitrogen introduced during pretreatment. The colour strength of the carbamated cotton increased by increasing the dye concentration, but the difference was very small at a 4% shade. This indicates that the fibre reached its saturation point, while the control half-bleached fabric colour strength increased in a fairly linear fashion. Looking at the results, the colour strength achieved by using a 5% shade of Reactive Red HE3B on the control half-bleached fabric could be obtained by using a 1% shade on the carbamated cotton fabric,

thus increasing the dye utilisation. Moreover, excellent levelness was visually observed on the dyed carbamated cotton fabric.

Fastness properties

The overall result of dyeing properties in terms of the fastness of Reactive Red HE3B towards carbamated cotton and control half-bleached fabric is summarised in Table 2. The result shows that wash fastness and rub fastness were not affected significantly. This may be due to the formation of a strong ionic bond between the fibre and the dye because it is equally good as the covalent bond that normally links the dye and the fibre.

Adsorption isotherm analysis

In order to study the adsorption property of Reactive Red HE3B dye on the carbamated cotton at a constant temperature, a sample of fabric was placed in a dye bath buffered at pH 6 and dyed for two hours at the temperature recommended by the dye manufacturer (i.e. 80 °C) [25]. The adsorption of Reactive Red HE3B dye by mercerised, carbamated cotton as a function of concentration is shown in Figure 9. It was observed that the initial dye adsorption was fast, and decreased with a subsequent increase in the concentration the dye.

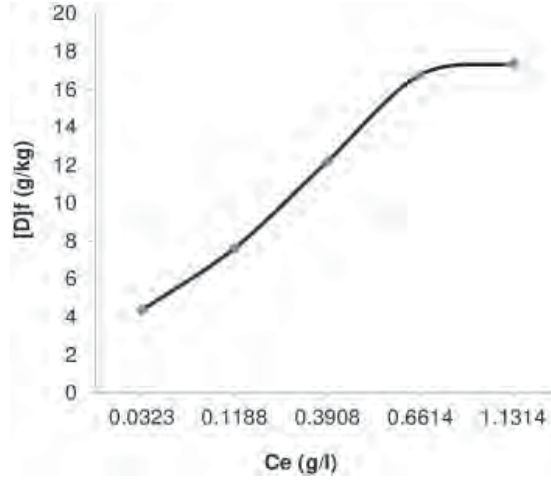

Figure 9: Effect of concentration on the adsorption of Reactive Red HE3B: temperature 80 °C; pH 6; amount is 5 g; time is 2 hours

Table 2: Summary of colourfastness results

Con. (%)	Material type	Wash fastness							Rubbing fastness		Light fastness
		Colour change	Staining on white								
			CA	CO	PA	PES	PAN	WO	Dry	Wet	
0.5	Control	4–5	4–5	4	4–5	5	4–5	5	5	4–5	4
	CCC[a)]	4–5	4	3–4	4–5	5	4–5	5	5	4–5	4
	M[b)]	4–5	4–5	4	4–5	5	4–5	5	5	4–5	5
1	Control	4–5	4–5	4	4–5	5	4–5	4–5	5	4–5	4
	CCC	4–5	4	3–4	4	5	4–5	4–5	4–5	4–5	4
	M	4–5	4–5	4	4–5	5	4–5	4–5	5	4–5	5
2	Control	4–5	4–5	4	4–5	5	4–5	4–5	5	4–5	5
	CCC	4	4	3–4	4	4–5	4–5	4–5	4–5	4–5	5
	M	4–5	4–5	4	4–5	5	4–5	4–5	5	4–5	5
3	Control	4–5	4–5	4	4	4–5	4–5	4–5	4–5	4–5	5
	CCC	4	4	3–4	3–4	4–5	4	4	4	4	5
	M	4–5	4–5	4	4	4–5	4–5	4–5	4–5	4–5	5
4	Control	4	4–5	4	4	4–5	4–5	4–5	4–5	4–5	5
	CCC	3–4	4	3–4	3–4	4–5	4	4	4	4	5
	M	4	4–5	4	4	4–5	4–5	4–5	4–5	4–5	5
5	Control	4	4	3–4	3–4	4–5	4–5	4	4	4	5
	CCC	3–4	3–4	3	3–4	4	3–4	3–4	4	4	5
	M	4	4	4	4	4–5	4–5	4	4	4	5

[a)] carbamated cotton cellulose; [b)]mercerised; CA: acetate; CO: cotton; PA: nylon, PES: polyester; PAN: acrylic; WO: wool

The profile obtained (Figure 9) from the study was utilised to plot Langmuir and Freundlich adsorption isotherms using well-known adsorption isotherm equations. In both the cases, linear plots were obtained and reveal the applicability of these isotherms on the ongoing adsorption process. Figures 10 (a) and 10 (b) illustrate Freundlich and Langmuir plots respectively for the adsorption of Reactive Red HE3B on mercerised carbamated cotton, while different Freundlich and Langmuir constants derived from these plots are presented in Table 3. However, the best fit for the system is found with a Freundlich adsorption isotherm with an R^2 value of 0.987 (Figure 10 (a)), while with Langmuir, the fit obtained is $R^2 = 0.963$ (Figure 10 (b)). It can thus be concluded that the dyes are not only attached to the available carbamate groups, but that they also form layers. In normal situations, with the dye used, the formation of layers is not particularly surprising because the dye molecule is essentially linear, similar to a direct dye. It would, therefore, be expected to show a tendency to form layers, with hydrogen bonding between appropriately placed groups on the dye and the fibre, and between dye molecules and other dye molecules. In this study, however, this kind of result was not expected because the carbamate groups that ionize (positively) should attract the negatively ionized Reactive Red HE3B dyes, while the remaining –OH were not expected to adsorb, as the hydroxyl group and the dye are negatively ionized and should thus repel one another. However, from the results, the adsorption was mostly explained with the Freundlich adsorption isotherm, which assumes that the dye adsorption is not limited to the functional groups available in the material to be dyed. The assumption was therefore made that the introduced functional groups play the role of attracting not only a single molecule, but rather many molecules that could be adsorbed on the hydroxyl groups.

Table 3: Freundlich and Langmuir constants of Reactive Red HE3B over carbamated cotton: temperature 80 °C; pH 6; amount 5 g; time 2 hours

Freundlich constants	n	0.407
	K	1.254
Langmuir constants	$[S]_f$ (g/l)	15.97
	K (l/g)	0.0056

Figure 11 shows the SEM image of half-bleached control, mercerised and carbamated fabrics. It is evident that surface roughness increased after carbamation, better than the deconvoluted, swollen and circular cross section of mercerised fibres. The fibres in the half-bleached control fabric are convoluted; surface roughness is not visible up to a magnification of 500-x. Surface roughness may have improved the adsorption property of the carbamated fabric, since it is expected that only the carbamate groups will be involved in the adsorption of the Reactive Red HE3B dye. The fact that most studies

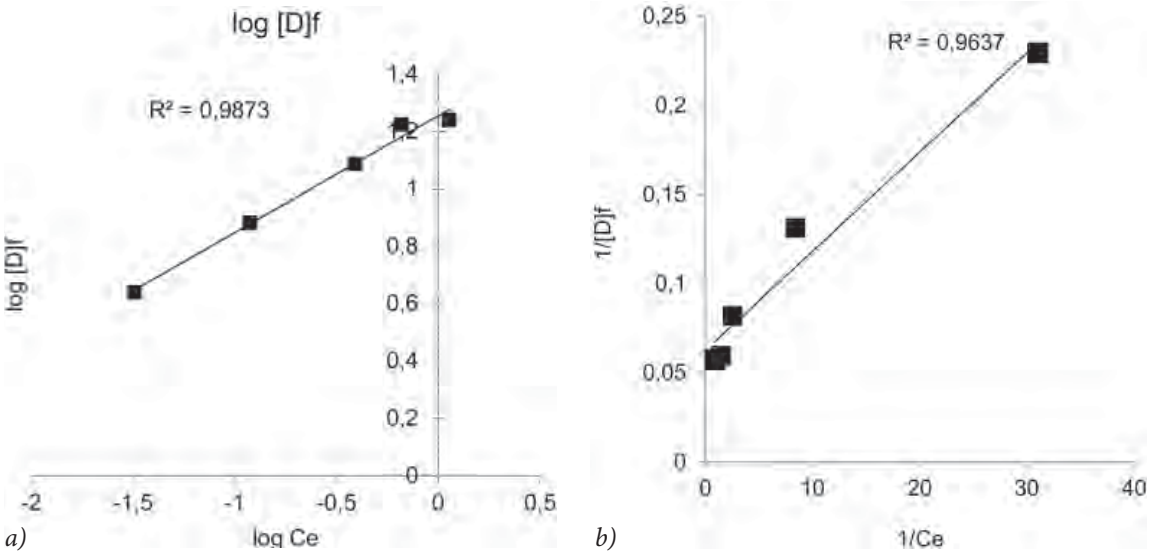

Figure 10: Adsorption isotherm for Reactive Red HE3B carbamated cotton system: temperature of 80 °C; pH 6; amount is 5 g; time is 2 hours; (a) Freundlich; (b) Langmuir

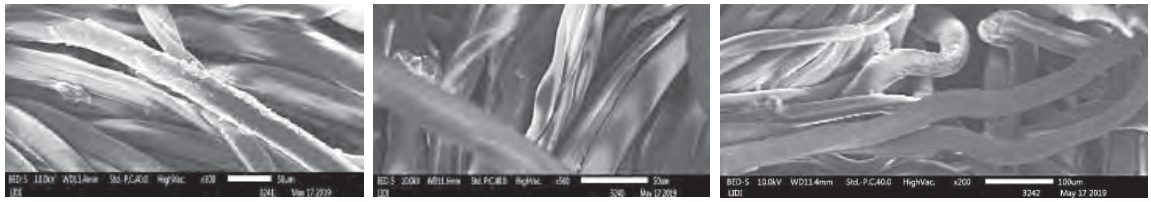

a) *b)* *c)*

Figure 11: SEM image of (a) carbamated; (b) control and (c) mercerised fabric

[29–31] of adsorption isotherm on cationised cotton provide a better explanation of the Langmuir adsorption isotherm (which is not the case in this study) might be because the surface roughness of the carbamated cotton fibre increased. The experimental data were fitted to the Langmuir model, with the linearised form presented in Figure 10 (b), which had high correlation coefficient ($R^2 = 0.963$), and demonstrated a very good correlation with the aforementioned model. The correlation coefficients also indicated a good correlation between parameters, and confirmed the functional adsorption of Reactive Red HE3B dye onto the carbamated fabric. Interestingly, the carbamated cotton with the selected dye fits the Freundlich model of adsorption isotherm, showing an even better correlation ($R^2 = 0.987$), as indicated in Figure 10 (b). A conclusion concerning a Langmuir-type interaction between anionic dyes and aminised cotton was already reported by Porter [32]. It was described that the sorption of dye from dye baths can be stopped when the amino groups of fibres have been saturated with dye molecules. According to the results obtained (which a Freundlich type of interaction explains better), the process could be because of the interaction between the anionic Reactive Red HE3B dye and a positive functional site ($-NH_3^+$) of the cotton fabric, which first causes the sorption of more dye molecules on the carbamated cotton. After the dyeing sites are fully saturated, dyes might begin to be adsorbed on the surface by weak bonds. The dyeing process will thus be improved with the mechanism explained, while the surface roughness of the carbamated cotton might play a crucial role.

4 Conclusion

The problem of reactive dyes requiring a large amount of electrolytes could be mitigated through an additional pretreatment process after mercerisation using urea to introduce a carbamate group in place of hydroxyl groups to make the cotton fabric positively charged. This makes the Reactive Red HE3B dye, which is negatively charged, highly attracted to the fibre. It can be concluded from the investigated report that urea, pad-dry-cure modification (i.e. carbamation) can improve the dyeability of cotton fibre. The treatment of carbamation allowed the adsorption of Reactive Red HE3B dye molecules onto cotton fibres and the reaction between the dye molecule and the cotton fibre without the utilisation of electrolytes. The procedure for optimum carbamation appeared to be at a urea concentration of 400 g/l for a curing time of 5 minutes at 135 °C. The degree of substitution was 0.2829, while warp- and weft-way tensile strengths were affected significantly. Dyeing studies show very good results with DS of 0.2829, The method would have great potential for industrial application, as pad-dry-cure is a relatively clean, environmentally friendly technique, with less energy, water, time and resources required, as the liquor could be reused. An entirely new system is required on curing equipment, which can collect the ammonia gas released during the decomposition of urea (which could be considered an advantage and could be used as a pre-activating agent for cotton cellulose, replacing caustic mercerisation, or as a raw material for different chemical reactions), while care must be given during the production of cotton cellulose carbamate.

The thermal analysis showed carbamated cotton fabrics have a very rapid degradation property above a temperature of 300 °C up to 370 °C, where the control half-bleached fabric starts at the same temperature of 300 °C and goes up to 400 °C. The dyeing results were good, with satisfactory fastness properties. The visual levelness of the dyed fabric was also good. The exhaustion, fixation and total dye utilisation percentage showed improvement compared with control half-bleached fabric. The change in total dye utilisation was in the range of 7–15% than that of control half-bleached fabric.

Dyeing basically happens between the negatively charged Reactive Red HE3B dye and the positively charged cotton cellulose due to the replacement of the hydroxyl group with the carbamate group. The adsorption isotherm demonstrated a good correlation with Langmuir (R^2 = 0.963) and Freundlich (R^2 = 0.987), while the increment in the surface roughness studied by SEM played a role in dyeing and in explaining the isotherm as Freundlich.

References

1. HEINZE, T., LIEBERT, T. Unconventional methods in cellulose functionalization. *Progress in Polymer Science,* 2001, **26**(9), 1689–1762, doi: 10.1016/S0079-6700(01)00022-3.
2. ROUETT, H. K., SCHWAGER, B. *Encyclopedia of textile finishing*. Berlin : Springer. 2001.
3. FU, F., XU, M., WANG, H., WANG, Y., GE, H., ZHOU, J. Improved synthesis of cellulose carbamates with minimum urea based on an easy scale-up method. *ACS Sustainable Chemistry and Engineering,* 2015, **3**(7), 1510–1517, doi: 10.1021/acssuschemeng.5b00219.
4. FU, F., YANG, Q., ZHOU, J., HU, H., JIA, B., ZHANG, L. Structure and properties of regenerated cellulose filaments prepared from cellulose carbamate–NaOH/ZnO aqueous solution. *ACS Sustainable Chemistry and Engineering*, 2014, **2**(11), 2604–2612, doi:10.1021/sc500559g.
5. FU, S., HINKS, D., HAUSER, P., ANKENY, M. High efficiency ultra-deep dyeing of cotton via mercerization and cationization. *Cellulose*, 2013, **20**(6), 3101–3110, doi: 10.1007%2Fs10570-013-0081-6.
6. GUO, Y., ZHOU, J., SONG, Y., ZHANG, L. An efficient and environmentally friendly method for the synthesis of cellulose carbamate by microwave heating. *Macromolecular Rapid Communications,* 2009, **30**(17), 1504–1508, doi: 10.1002/marc.200900238.
7. KEUNECKE, G., STRUSZCZYK, H., STAROSTKA, P., MIKOLAJSCYK, W., URBANOWSKI, A. *Method for modified manufacture of cellulose carbamate, US Patent 5906926 (A). 1999-05-25.*
8. NOZAWA, Y., HIGASHID, F. Partially carbamate reaction of cellulose with urea. *Journal of Applied Polymer Science*, 1981, **26**(6), 2103–2107, doi: 10.1002/app.1981.070260633.
9. SELIN, J. F., HUTTUNEN, J., TURUNEN, O., FORS, J., EKLUND, V., EKMAN, K. *Cellulose carbamate solutions, US Patent 4526620 (A). 1985-07-02.*
10. HEINZE, T., EL SEOUD, O. A., KOSCHELLA, A. *Cellulose Derivatives : Synthesis, Structure, and Properties.* Cham : Springer, 2018, 379–409.
11. HEARON, W., AND HIATT, G. D., FORDYCE, C. R. Carbamates of cellulose and cellulose acetate : I. preparation. *Journal of the American Chemical Society*, 1943, **65**(5), 829–833, doi: 10.1021/ja01245a020.
12. HALL, D. M., HORNE, J. R. Preparation of cellulose triacetate and cellulose tricarbanilate by nondegradative methods. *Journal of Applied Polymer Science*, 1973, **17**(12), 3727–3732, doi: 10.1002/app.1973.070171214.
13. WOOD, B. F., CONNER, A. H. HILL JR, C. G. The effect of precipitation on the molecular weight distribution of cellulose tricarbanilate. *Journal of Applied Polymer Science*, 1986, **32**(2), 3703–3712, doi: 10.1002/app.1986.070320225.
14. TERBOJEVICH, M., COSANI, A, CAMILOT, M., FOCHER, B. Solution studies of cellulose tricarbanilates obtained in homogeneous phase. *Journal of Applied Polymer Science*, 1995, **55**(12), 1663–1671, doi: 10.1002/app.1995.070551206.
15. EVANS, R., WEARNE, R. H., WALLIS, A. F. Molecular weight distribution of cellulose as its tricarbanilate by high performance size exclusion chromatography. *Journal of Applied Polymer Science*, 1989, **37**(12), 3291–3303, doi: 10.1002/app.1989.070371202.
16. GAN, S., ZAKARIA, S., CHIA, C. H., KACO, H., PADZIL, F. N. M. Synthesis of kenaf cellulose carbamate using microwave irradiation for preparation of cellulose membrane. *Carbohydrate Polymers,* 2014, **106**(1), 160–165. doi: org/10.1016/j.carbpol.2014.01.076.
17. YIN, C., LI, J., XU, Q., PENG, Q., LIU, Y., SHEN, X. Chemical modification of cotton cellulose in supercritical carbon dioxide : Synthesis and characterization of cellulose carbamate. *Carbohydrate Polymers*, 2007, **67**(2), 147–154, doi: 10.1016/j.carbpol.2006.05.010.
18. WALLIS, A. F., WEARNE, R. H. Side reactions of phenylisocyanate during amine-catalysed carbanilation of cellulose. *European Polymer Journal,* 1990, **26**(11), 1217–1220, doi: 10.1016/0014-3057(90)90031-X.

19. EVANS, R., WEARNE, R. H., WALLIS, A. F. Effect of amines on the carbanilation of cellulose with phenylisocyanate. *Journal of Applied Polymer Science*, 1991, **42**(3), 813–820, doi: 10.1002/app.1991.070420326.
20. MORMANN, W., MICHEL, U. Improved synthesis of cellulose carbamates without by-products. *Carbohydrate Polymers*, 2002, **50**(2), 201–208, doi: 10.1016/S0144-8617(02)00016-4.
21. CAI, J., ZHANG, L., ZHOU, J., QI, H., CHEN, H., KONDO, T., CHEN, X., CHU, B. Multifilament fibers based on dissolution of cellulose in NaOH/urea aqueous solution : structure and properties. *Advanced Materials*, 2007, **19**(6), 821–825, doi: 10.1002/adma.200601521.
22. CAI, Y., PAILTHORPE, M. T., DAVID, S. K. A new method for improving the dyeability of cotton with reactive dyes. *Textile Research Journal*, 1999, **69**(6), 440–446, doi: 10.1177/004051759906900608.
23. CHATTOPADHYAY, D. P., CHAVAN, R. B., SHARMA, J. K. Salt-free reactive dyeing of cotton. *International Journal of Clothing Science and Technology*, 2007, **19**(2), 99–108. doi: 10.1108/09556220710725702.
24. SUBRAMANIAN SENTHIL KANNAN, GOBALAKRISHNAN, M., KUMARAVEL, S., NITHYANADAN, R., RAJASHANKAR, K. J., VADICHERALA, T. Influence of cationization of cotton on reactive dyeing. *Journal of Textile and Apparel, Technology and Management*, 2006, **5**(2), 23–30, https://textiles.ncsu.edu/tatm/wp-content/uploads/sites/4/2017/11/subramanainfull161_05.pdf.
25. NOZAWA, Y., HIGASHID, F. Partially carbamate reaction of cellulose with urea. *Journal of Applied Polymer Science*, 1981, **26**(6), 2103–2107, doi: 10.1002/app.1981.070260633.
26. AATCC. *Technical manual of the American Association of Textile Chemists and Colorists*. Research Triangle Park : American Association of Textile Chemists and Colorists, 2012.
27. MONTAZER, M., MALEK, R. M. A., RAHIMI, A. Salt free reactive dyeing of cationized cotton. *Fibers and Polymers*, 2007, **8**(6), 608–612. doi: 10.1007/BF02875997.
28. ASTM. *Standard test method for tensile properties*. West Conshohocken : ASTM International, 2010.
29. MUGHAL, M. J., NAEEM, M., ALEEM, A., SAEED, R., AHMED, K. Effect of a cationising agent on the conventional reactive dyeing of cotton. *Coloration Technology*, 2008, **124**(1), 62–65. doi: 10.1111/j.1478-4408.2007.00122.x.
30. BROADBENT, A. D. *Basic principles of textile coloration*. West Yorkshire : Society of Dyers and Colourists, 2001.
31. MARRINAN, H. J., MANN, J. Infrared spectra of the crystalline modifications of cellulose. *Journal of Polymer Science,* 1956, **21**(98), 301–311, doi: 10.1002/pol.1956.120219812.
32. PORTER, J. J. Dyeing equilibria : interaction of direct dyes with cellulose substrates. *Coloration Technology*, 2002, **118**(5), 238–243, doi: 10.1111/j.1478-4408.2002.tb00106.x.

Dinesh Bhatia [1, 2], S.K. Sinha[2]
[1] Jawahar Lal Nehru Govt. Engineering College, Department of Textile Engineering, Sundernagar (Himachal Pradesh), India
[2] Dr. B.R. Ambedkar National Institute of Technology, Department of Textile Technology, Jalandhar (Punjab), India

Thermo-physiological Properties of Structurally Modified Wool/Polyester Blended Machine and Hand-Spun Yarns as a Weft in Handloom Fabrics

Lastnosti toplotne udobnosti ročno stkanih tkanin z votkom iz strukturno modificirane preje iz mešanice volna/poliester, izdelanim strojno in ročno

Original scientific article/*Izvirni znanstveni članek*
Received/*Prispelo* 4-2020 • Accepted/*Sprejeto* 5-2020

Abstract

An attempt was made to compare the combined desirability value for a treated and untreated handloom fabric using machine-spun and hand-spun blended yarns as weft. The experimental plan included the preparation of both hand-spun and machine-spun yarns at different blend compositions according to a mixture design prepared on Design-Expert software, followed by the preparation of fabric on a handloom. The dissolution of one component using a suitable chemical treatment was then performed on both fabrics made from hand-spun and machine-spun yarn by taking into account an expected significant change in the arrangement of constituent fibres that ultimately enhance performance in terms of the thermo-physiological behaviour of fabrics. All properties viz air permeability, compressibility, thermal resistance, water vapour permeability, bending rigidity and drying capacity showed significant differences for both type of fabrics. Fabrics with hand-spun yarn as a weft demonstrated higher values of thermal resistance, compressibility, water vapour permeability and drying capacity due to the voluminous and soft structure of hand-spun yarn compared to fabric with machine-spun yarn as a weft. In general, after the dissolution of the polyvinyl alcohol component, both types of fabrics exhibited higher values of thermal resistance, compressibility, drying capacity and water vapour permeability, while values for air permeability and bending rigidity were lower for untreated fabrics. The results of the optimisation of treated fabrics with machine-spun yarn as weft demonstrated the highest desirability value (0.73), as well as a lower percentage of wool fibres (55%), followed by treated fabrics with hand-spun yarn as weft, which demonstrated a desirability value of 0.66 and a percentage of wool fibres of 60% in the blend composition. Untreated fabrics (both machine-spun and hand-spun) exhibited a similar desirability value and at same blend composition (20% polyester, 70% wool and 10% polyvinyl alcohol).
Keywords: desirability, optimisation, blend composition, PVAL, handloom, thermal resistance

Izvleček

Neobdelane in obdelane ročno stkane tkanine z votkom iz strojno in ročno izdelanih mešanih prej so bile primerjane z vidika kombiniranega indeksa zaželenosti. Eksperimentalni načrt vključuje pripravo ročno in strojno spredene preje iz mešanic različne sestave glede na načrt, zasnovan s pomočjo programskega orodja Design-Expert, ki mu je sledila izdelava tkanin na ročnih statvah. Obe vrsti tkanin, izdelanih z ročno oziroma strojno spredeno prejo v votku, so bile kemično obdelane, pri čemer se je raztopila ena komponenta, da bi dosegli pričakovano spremembo razporeditve

Corresponding author/*Korespondenčni avtor:*
Dr. S.K. Sinha
E-mail: sinhask@nitj.ac.in
ORCID: 0000-0003-0871-3948

Tekstilec, 2020, ***63****(2), 138-150*
DOI: 10.14502/Tekstilec2020.63.138-150

vsebovanih vlaken, ki znatno izboljšajo toplotno udobje tkanin pri nošenju. Vse lastnosti, tj. zračna prepustnost, stisljivost, toplotni upor, prepustnost vodne pare, upogibna togost in kapaciteta sušenja, kažejo na velike razlike med obema vrstama tkanin. Zaradi voluminozne in mehke strukture ročno spredene votkovne preje so imele tkanine, ki so to prejo vsebovale, višje vrednosti toplotnega upora, stisljivosti, prepustnosti vodne pare in so se sušile hitreje v primerjavi s tkaninami, ki so vsebovale strojno spredeno votkovno prejo. Na splošno sta po raztopitvi komponente polivinilnega alkohola obe vrsti tkanin pokazali višje vrednosti toplotnega upora, stisljivosti, sposobnosti sušenja in prepustnosti vodne pare in nižje vrednosti zračne prepustnosti in upogibne togosti v primerjavi z neobdelanimi tkaninami. Rezultati optimizacije za obdelane tkanine, ki so vsebovale strojno spredeno votkovno prejo, kažejo najvišjo indeks zaželenosti (0,73) pri najnižji vsebnosti volne (55 %), sledijo obdelane tkanine z ročno spredeno prejo v votku (0,66) in 60 % volnenih vlaken v mešanici. Neobdelane tkanine (s strojno in ročno spredeno votkovno prejo) so imele skoraj podobni indeks zaželenosti in enako mešanico (20 % poliestra, 70 % volne in 10 % polivinil alkohola).
Ključne besede: zaželenost, optimizacija, sestava mešanice, PVAL, ročne statve, toplotni upor

1 Introduction

The handloom industry is one of the oldest and largest cottage industry in India,which represents and preserves the vibrant culture of India. Due to the use of less capital and power, their eco-friendly behaviour and their suitability for innovation and transformation with respect to market requirements, handloom fabrics provide a broader scope for research and innovation. Comfort is considered one of the fundamental properties for evaluating any textile material. Comfort is defined as "the absence of unpleasantness or discomfort" or "a natural state compared to the mere active state of pleasure". Handloom fabrics are more comfortable due to the specific behaviour of handloom fabric and the structure of hand-spun yarn because the structure of yarn and fabric plays an important role in the comfort of any fabric.

Thermo-physiological wear comfort, which relates to the heat and moisture transport properties of clothing and the way that clothing helps to maintain the heat balance of the body during various activities, is one of the basic and necessary properties of a fabric. Any change in the structure of yarn and fabric helps to improve comfort in terms of heat and moisture, as it plays important role in the comfort of any fabric. Thus, many researchers attempt to identify different methods by which the structure of yarn and fabric can be altered to improve comfort properties. The nature, composition and arrangement of constituent fibres, through the dissolving of one component, can influence the structure, properties and performance of yarn, which may ultimately influence fabric comfort properties [1–6]. Mixture experiments are a special class of response surface experiments in which the product under investigation is made up of several components or ingredients [7]. This design is thus suitable in a situation where the response is a function of the proportions of the different ingredients in the mixture [8].

During the twenty-first century, clothing markets have become highly competitive due to high demand and changing fashion. The textile and clothing industries are searching for competitive advantages by understanding and meeting consumer needs and desires in order to survive on the rapidly changing, highly competitive clothing market. Different statistical techniques are developed by researchers to satisfy the needs of industries. These include response surface methodology and various optimisation algorithms, e.g. the desirability function-based approach [9–10], multiple regression and linear programming-based approaches [11], and utility function-based approach [12]. Among the above, the desirability function-based approach has gained the most popularity in solving optimisation problems. Ghosh et al. [13] optimised different comfort and safety properties using the desirability function to achieve an overall desirability varying from zero to one. Gupta et al. [14] used the desirability approach to optimise carpet durability by considering abrasion loss, compression and compression recovery as a single objective. Knitted fabric properties, such as areal density, bursting pressure, extensibility, dimensional stability and abrasion resistance, were optimised using the desirability function [15]. Asim et al. [16] estimated the fixation of reactive printing and crease-resistant finishing using the desirability function.

The disappearance of traditional textiles, through globalisation due to a lack of seriousness in this

field, has again prompted researchers to improve the quality of these fabrics through different product development to compete on the highly competitive market of power loom fabrics.

The present work involved a detailed study of all the important fabric comfort properties of handloom fabrics made of the same warp yarn and different filling (for both machine- and hand-spun), which were produced according to a mixture design from different percentages of wool, polyester and PVAL. The optimisation of different fabric properties was preformed using the desirability function.

2 Experimental

2.1 Materials

Merino wool (19.5 μm, 70 mm), polyester (2 dtex, 52 mm) and polyvinyl alcohol (PVAL; 1.44 dtex, 44 mm) fibres were blended on a gill box in different proportions according to a mixture design.

Table 1: Levels and factors are given below

Factors	Low	Medium	High
Polyester (%)	20	40	60
Merino wool (%)	30	50	70
PVAL (%)	10	15	20

Table 2: Mixture design used to produce different blend proportions of yarn

S. No.	Polyester (%)	Merino wool (%)	PVAL (%)
S1	35	45	20
S2	20	60	20
S3	20	65	15
S4	20	70	10
S5	55	30	15
S6	40	50	10
S7	60	30	10
S8	40	50	10
S9	20	70	10
S10	60	30	10
S11	60	30	10
S12	50	30	20

Twelve wool/polyester/PVAL blended yarn samples, with a nominal linear density 50 tex (20 Nm), were prepared on a worsted spinning system. Another set of twelve yarns of the same linear density were also prepared on charkha (hand-spun yarns). A mixture design (Table 2) was used to investigate the proportion of different fibres on various properties of yarn. The idea of using a mixture design is to study the effect of the proportion of different fibres, and to set the proportion of the fibres according to the end-product with limited numbers of samples. The levels and percentages of different fibres are presented in Table 1.

2.2 Fabric formation

Twenty-four fabric samples were prepared on a handloom by varying weft yarns (twelve from machine-spun and twelve from hand-spun yarn) and keeping warp yarn constant for all the fabrics. BT and BTH denote fabrics before treatment with machine-spun and hand-spun weft yarn respectively, while AT and ATH denote fabrics after treatment with machine-spun and hand-spun weft yarn respectively.

2.3 Dissolution of PVAL fibre on fabric stage

After the production of fabrics, PVAL was removed by treating the fabrics (that contain PVAL in their filling yarn) with 0.5% formic acid at 90 °C for 60 minutes, followed by a hot wash. All fabric samples were then dried in an oven, followed by conditioning for 24 hours under standard atmospheric conditions to achieve standard moisture conditions.

2.4 Test methods

The prepared samples were conditioned and tested for different fabric properties according to the standard mentioned below. Air permeability was measured using a TEXTEST FX 3300 air permeability tester according to the BS 5636 standard. Water vapour permeability (WVP) was measured according to the BS 7209 standard. Permeability was calculated using equation 1.

$$WVP = \frac{24\,m}{\mathrm{A} \times t}\ (\mathrm{g\ m^{-2}\ 24^{-1}\ h^{-1}}) \qquad (1),$$

where, m represents loss in mass (g), A represents the open area of the dish (m^2) and t represents the time between weighing (h).

For the purpose of testing drying capacity, 12 circular specimens per sample were cut using a round-shaped

cutter, each with an area of 100 cm^2. Specimens were conditioned at a standard atmosphere for 6 hours as per ASTM D 1776 and the weight of each sample (W_1) was recorded. The samples were dipped in distilled water to a depth of around 10 cm with the help of a wire sinker. After 6 hours, the specimens were taken out and kept on a sponge sheet to dry in a closed room where there was no air movement. A tropical atmosphere room temperature (27 °C ± 2 °C) and relative humidity (65% ±2 %) were maintained during the test. All fabrics were kept under the same conditions and the face side of the specimens was kept up. After a fixed time (i.e. 10 hours), the weight (W_2) of specimens was taken for all samples. Drying capacity was calculated by using equation 2.

$$\textit{Drying capacity} = \\ = (W_2 - W_1) \times 100 \text{ (g m}^{-2}\text{ 10}^{-1}\text{ h}^{-1}\text{)} \quad (2),$$

where W_1 represents the weight of the specimen (g) and W_2 represents the weight of water (g) dried from the fabric per 100 cm^2 in 10 h.

The test to determine fabric stiffness was carried out according to ASTM D1388-33 using a stiffness tester. Before the tests, the samples were conditioned under laboratory conditions (27 ± 2 °C, 65 ± 2% relative humidity (RH)). The tests were performed on each fabric sample at five replicas in both the warp and weft directions. Equation 3 given below was used to calculate the bending rigidities in the warp and weft directions. Overall fabric bending rigidity was calculated using equation 4.

$$G = 9.807 \times 10^{-6} Wc^3 \quad (3),$$

where, G represents the fabric bending rigidity (μNm) and W represents the mass per unit area (g m^{-2}), while the bending length c is equal to half the length of the overhang (mm).

$$G_o = (G_w G_f)^{\frac{1}{2}} \quad (4),$$

where, G_o represents the overall fabric bending rigidity, G_w represents the warp bending rigidity and G_f represents the weft bending rigidity.

To measure compressibility, the thickness of the fabric was measured using a thickness gauge at pressures of 20 g cm^{-2} and 50 g cm^{-2}. The compressibility of the fabric was then calculated using equation 5:

$$\textit{Compressibility} = \left[\frac{T_{20} - T_{50}}{T_{20}}\right] \times 100 \text{ (\%)} \quad (5),$$

where T_{20} and T_{50} represent the thickness of fabric measured using a thickness gauge at pressures of 20 g cm^{-2} and 50 g cm^{-2} respectively.

The thermal resistance of fabric was measured on a Testex guarded hot plate thermal conductivity tester. A minimum of three observations were carried out to determine the average CLO value.

3 Results and discussion

3.1 Observed structural changes

SEM images of untreated and treated fabric are shown in Figures 1–4. Figure 1 and Figure 3 show a

a) b)

Figure 1: Scanning electron microscope images: a) S4 BT and b) S4 AT

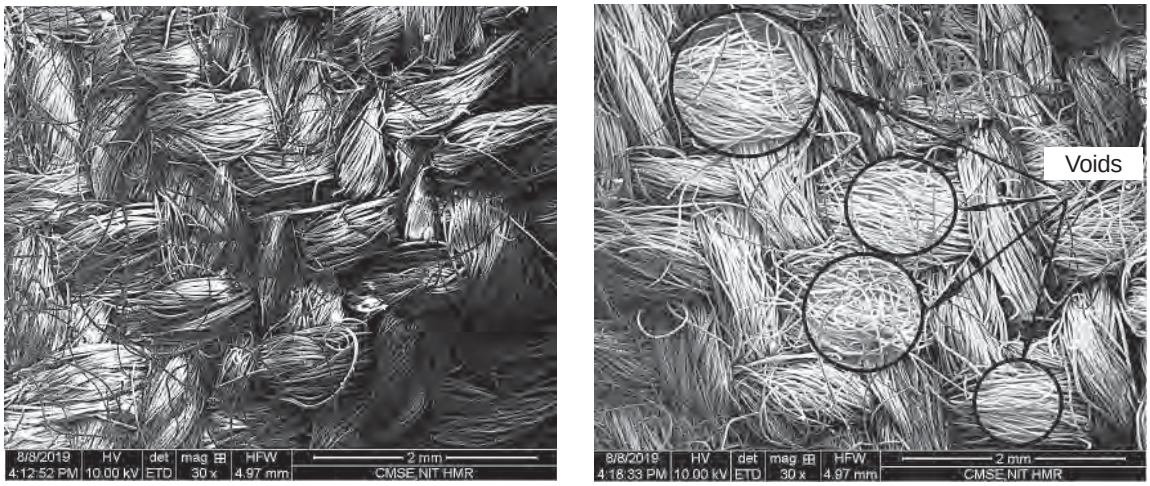

a) *b)*

Figure 2: Scanning electron microscope images: a) S4 ATH and b) S4 BTH

a) *b)*

Figure 3: Scanning electron microscope images: a) S7 BT and b) S7 AT

a) *b)*

Figure 4: Scanning electron microscope images: a) S7 ATH and b) S7 BTH

fabric with maximum wool content with machine-spun and hand-spun yarn as a weft respectively, while Figure 2 and Figure 4 show a fabric with maximum polyester content with machine-spun and hand-spun yarn as a weft respectively.

The following observations can be made from the images:

(a) The removal of the PVAL component led the creation of voids in the structure of fabric.
(b) The treatment of fabric with hand-spun yarn as a weft created more voids than fabric with machine-spun yarn as a weft.
(c) More voids were observed in fabric with weft yarn with a higher percentage of wool after the dissolution of the PVAL component than in fabric with weft yarn with a lower wool content.

The creation of voids after the dissolution of the PVAL component influences the arrangement and configuration of fibres in yarns. This change in the arrangement and configuration of fibres in yarn and fabric ultimately influences the thermo-physiological characteristics of fabric.

3.2 Properties of fabrics

Table 3 shows the physical properties of fabrics, such as the weight per unit area, thickness, thread density and yarn linear density of both treated and untreated fabrics for hand-spun and machine-spun yarns as weft.

Table 4 shows properties related to the thermo-physiological behaviour of both treated and untreated fabrics with machine- and hand-spun yarns as a weft.

Thermal resistance

The experimental results of thermal resistance (CLO value) are presented in Table 4 for both treated and untreated fabrics containing both hand- and machine-spun yarns as a weft at different blend compositions.

It is evident from Figure 5 that the CLO value is higher for fabrics containing hand-spun yarn than for fabrics that contain machine-spun yarn as a weft. Air entrapment is one of the major reasons for the enhancement of the thermal resistance of any fabric. Hand-spun yarn is voluminous and soft, which helps to make bulkier fabric than machine-spun yarn, which helps to entrap more air, resulting in a higher value of thermal resistance in terms of a higher CLO value.

As shown in Figure 5, the thermal resistance of treated fabric (for both machine- and hand-spun yarn) is higher than that of untreated fabric. After the dissolution of the PVAL component, the diameter of the yarn increased causing the creation of pores in the structure, which helps in the entrapment of air, resulting in a higher CLO value for treated fabrics than for untreated fabrics.

Table 3: Physical properties of fabrics before and after treatment (weft from both hand- and machine-spun yarns)

Seq. no	Mass per unit area ($g\ m^{-2}$)				Thickness (mm)				EPI/PPI				Linear density (Nm) warp/weft yarns	
	BT	AT	BTH	ATH	BT	AT	BTH	ATH	BT	AT	BTH	ATH	BT	BTH
S1	190	180	185	178	0.58	0.62	0.59	0.64	48/50	46/48	48/51	46/48	30.2/20.5	30.2/20.4
S2	175	170	174	168	0.64	0.67	0.65	0.70	49/51	47/49	49/51	47/49	30.2/20.4	30.2/20.5
S3	178	170	173	165	0.67	0.69	0.65	0.70	50/51	46/47	50/51	46/47	30.2/20.4	30.2/20.4
S4	170	159	168	154	0.66	0.69	0.64	0.70	48/53	47/48	48/52	47/48	30.2/20.3	30.2/20.4
S5	176	164	174	163	0.55	0.59	0.57	0.61	50/52	47/50	50/52	47/50	30.2/20.3	30.2/20.4
S6	183	175	182	173	0.57	0.60	0.59	0.63	48/53	47/51	48/53	47/51	30.2/20.4	30.2/20.3
S7	182	172	180	172	0.55	0.58	0.57	0.59	50/49	48/47	50/49	48/47	30.2/20.4	30.2/20.4
S8	185	179	180	172	0.57	0.59	0.59	0.63	53/52	51/51	53/52	51/51	30.2/20.2	30.2/20.3
S9	168	160	165	158	0.65	0.68	0.67	0.71	48/52	47/51	48/52	47/51	30.2/20.2	30.2/20.4
S10	182	174	178	170	0.55	0.57	0.56	0.60	50/51	50/49	49/51	50/49	30.2/20.3	30.2/20.4
S11	181	172	178	171	0.54	0.57	0.56	0.60	50/51	49/50	50/51	49/50	30.2/20.4	30.2/20.3
S12	180	169	178	168	0.55	0.57	0.58	0.61	50/51	49/50	49/51	49/50	30.2/20.5	30.2/20.4

Table 4: Fabric properties before and after treatment (weft from both hand- and machine-spun yarns)

S. No.	Thermal resistance (CLO)				Compressibility (%)				Air permeability ($cm^3\ cm^{-2}\ s^{-1}$)				
	BT	AT	BTH	ATH	BT	AT	BTH	ATH	BT	AT	BTH	ATH	
S1	0.14	0.20	0.16	0.21	16.27	25.34	20.24	27.78	35.12	28.14	32.12	25.14	
S2	0.16	0.21	0.18	0.22	18.98	26.62	22.41	28.24	36.01	29.12	34.11	28.47	
S3	0.16	0.21	0.18	0.22	19.14	27.22	23.14	29.45	36.92	30.22	33.45	29.15	
S4	0.17	0.20	0.18	0.21	20.94	28.05	24.20	30.25	38.25	31.25	35.21	29.78	
S5	0.14	0.18	0.16	0.19	13.23	17.95	17.25	20.10	27.35	20.95	24.78	20.12	
S6	0.15	0.18	0.16	0.20	15.67	22.46	19.47	24.58	30.66	25.16	27.22	24.14	
S7	0.14	0.19	0.16	0.21	12.75	16.62	16.78	18.89	26.02	19.22	23.92	19.14	
S8	0.15	0.18	0.17	0.19	17.27	22.81	21.62	24.78	32.41	25.51	29.33	24.18	
S9	0.16	0.19	0.18	0.20	20.13	26.94	24.18	28.45	36.22	29.92	33.62	28.46	
S10	0.14	0.18	0.16	0.20	12.71	16.34	16.98	18.78	26.3	19.3	23.14	19.13	
S11	0.14	0.18	0.16	0.20	12.56	15.98	16.89	18.90	25.22	18.92	22.7	18.27	
S12	0.14	0.20	0.16	0.21	11.48	18.67	15.24	17.49	27.97	21.77	24.87	20.47	

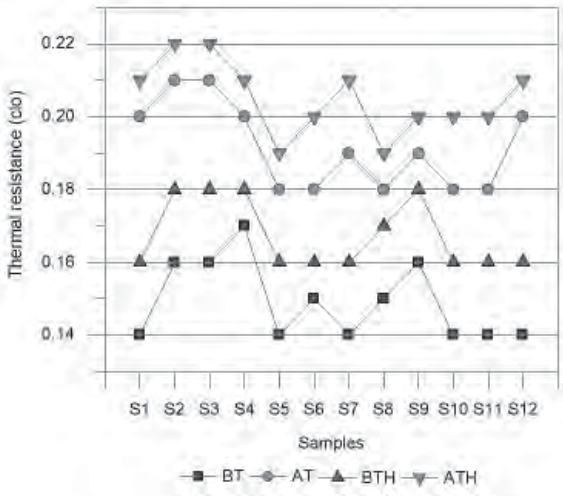

Figure 5: Thermal resistance of fabrics

Compressibility

The compressibility of any fabric is influenced by its bulkiness and thickness. Bulkier and thicker fabric compresses more easily than less bulky and thinner fabric. Figure 6 shows the compressibility for all fabrics in the treated and untreated stages. It was determined that fabric with hand-spun yarn compresses more easily than fabric with machine-spun yarn as a weft. Due to the structural differences and higher bulk of hand-spun yarn, the fabrics are spongier that fabrics with machine-spun yarn as a weft. Thus, fabrics from hand-spun yarn are bulkier, which leads to the higher compression value of the fabric.

This study also found that treated fabric shows a higher compression than untreated fabric, for both fabrics with machine- and hand-spun yarn as a weft, as shown in Figure 6. After the dissolution of the PVAL component, pores developed in the yarn structure, which ultimately led to a reduction in the compactness of fabric. Thus, the compression of treated fabric increased after the dissolution of the PVAL component.

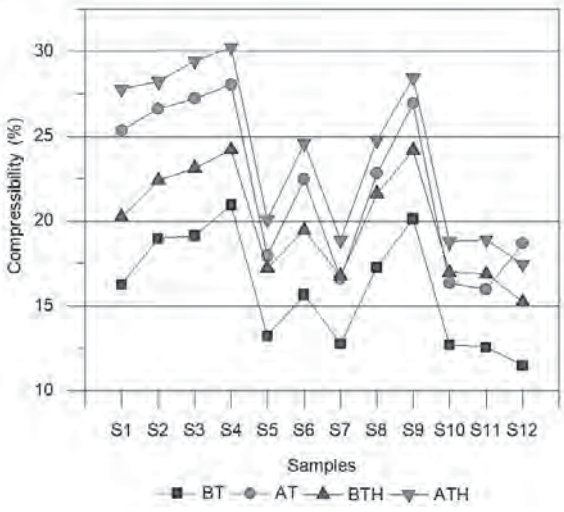

Figure 6: Compressibility of fabrics

Air permeability

The air permeability of fabric depends on the inter and intra yarn pores, and the hairiness of the yarn used in a fabric. Hand-spun yarns are voluminous

	Water vapour permeability ($g\ m^{-2}\ 24^{-1}\ h^{-1}$)				Bending rigidity (μNm)				Drying capacity ($g\ m^{-2}\ 10^{-1}\ h^{-1}$)			
	BT	AT	BTH	ATH	BT	AT	BTH	ATH	BT	AT	BTH	ATH
	1425.5	1621.2	1220.34	1410.12	204.42	181.34	200.23	178.98	187	294	200	300
	1617.2	1720.2	1410.21	1547.27	213.43	187.78	204.45	184.22	211	303	228	307
	1635.3	1789.9	1420.10	1549.22	215.67	187.67	210.26	183.26	211	305	226	310
	1712.2	1821.4	1545.23	1658.47	203.78	194.89	199.32	190.78	223	293	235	300
	1454.7	1659.5	1245.10	1469.20	183.89	169.21	178.96	161.45	190	273	205	280
	1522.2	1728.6	1322.89	1536.23	188.45	161.66	180.23	155.58	197	278	211	288
	1410.5	1578.7	1245.55	1389.36	192.67	170.67	185.69	162.24	191	278	208	280
	1534.4	1789.9	1332.45	1589.36	187.67	172.73	180.23	165.89	197	277	215	282
	1693.8	1822.4	1489.59	1635.78	201.89	193.90	195.78	184.78	207	283	219	288
	1456.9	1547.2	1278.36	1345.25	191.34	168.45	182.36	162.45	190	275	204	281
	1447.1	1549.4	1274.32	1345.89	192.43	170.23	183.54	161.23	189	272	202	278
	1456.3	1687.3	1233.36	1458.36	206.22	172.56	198.58	189.22	191	296	204	302

and can easily flatten, thereby reducing both inter and intra yarn porosity. Moreover, any increase in hairiness will cause air permeability to decrease. The hairiness of hand-spun yarn was higher than that of machine-spun yarn, resulting in the higher air permeability of fabric with machine-spun yarn as a weft.

Table 4 illustrates that the dissolution of one component resulted in a lower value of air permeability for treated fabrics than for untreated fabric. The air permeability of fabric was closely correlated with inter yarn porosity. Both intra and inter yarn porosity was affected by yarn flattening or deformation in the fabric due to yarn compressibility. After the dissolution of the PVAL component, there was an increase in both yarn and fabric compressibility, which might have led to yarn flattening or fabric deformation. This ultimately reduced the air permeability of treated fabric.

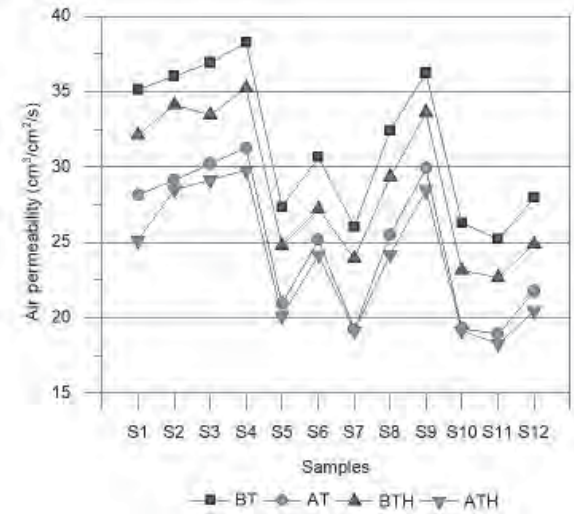

Figure 7: Air permeability of fabrics

Water vapour permeability

It is evident from Figure 8 that fabric containing hand-spun yarn as a weft exhibited lower water vapour permeability than fabric with machine-spun yarn as a weft. The water vapour permeability of fabric depends on the rate of diffusion. The irregular structure of hand-spun yarn could lead to a reduction in the diffusion rate, resulting in the reduced water vapour permeability of fabric.

Experimental results for the water vapour permeability of fabrics before and after treatment are presented in Table 4, which shows that, after the dissolution of the PVAL component, treated fabric exhibited a higher water vapour permeability than untreated fabric. The transfer of vapour through fabric depends on diffusion. The rate of diffusion from fabric depends on the pores/voids created in the structure by the dissolution of the PVAL component from a blended yarn. After the dissolution of the PVAL component, pores were created in the yarn structure, which resulted in the better transfer of water vapours through the diffusion process from one side of fabrics to other

through pores within the structure, resulting in a higher value of water vapour permeability for treated fabric.

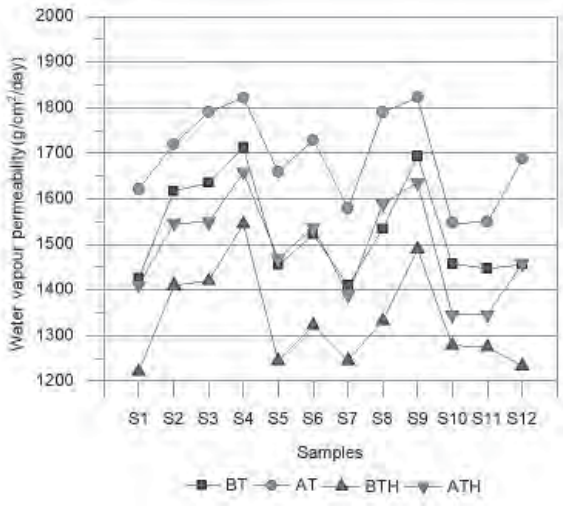

Figure 8: Water vapour permeability of fabrics

Bending rigidity

Fabric bending rigidity is an important parameter that can influence the handling and comfort of textile material. It is evident from Figure 9 that fabric with hand-spun yarn as a weft exhibited a lower bending rigidity than fabric with machine-spun yarn as a weft. Hand-spun yarn is softer and more pliable than machine-spun yarn. Fabric from machine-spun yarn is thus stiff.

Experimental results shown in Table 4 for untreated and treated fabric show a reduction in bending rigidity after the removal of the PVAL component

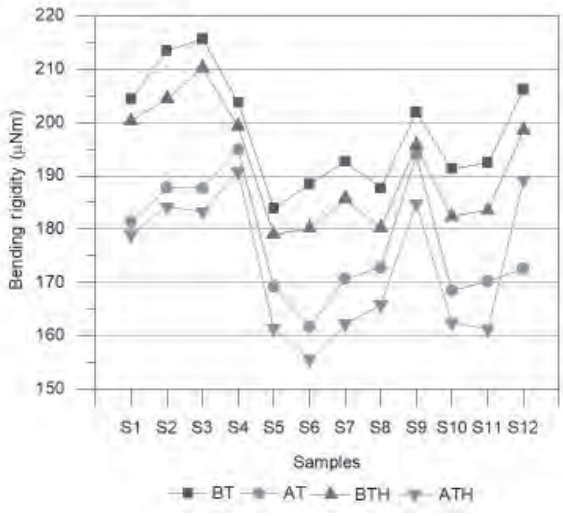

Figure 9: Bending rigidity of fabrics

for both type of fabrics. This may be due to the creation of pores after the dissolution of the PVAL component, which ultimately enhanced fabric flexibility.

Drying capacity

It is evident from Figure 10 that the drying capacity of fabrics with hand-spun yarn as a weft is higher than that of fabric with machine-spun yarn as a weft. The porous nature of hand-spun yarn, which helps to absorb higher water content, resulted in a higher value of drying capacity than that of fabric with machine-spun yarn as a weft.

Results from Table 3 shows that the drying capacity value increased after the dissolution of the PVAL component, meaning that treated fabric will take more time to dry than untreated fabric. A structure that can absorb a larger mass of water will have a high drying capacity value, i.e. it will take longer to dry.

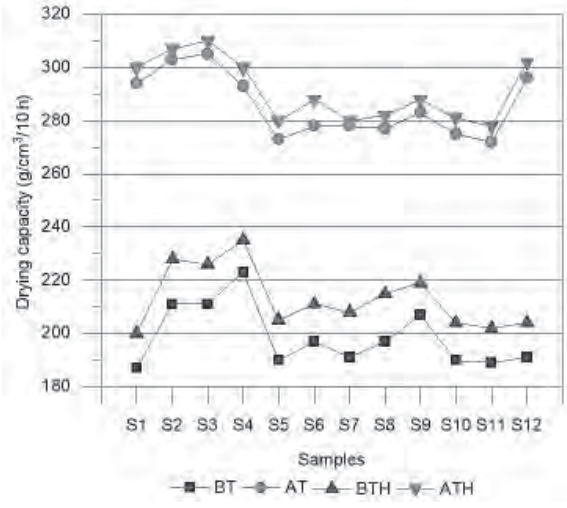

Figure 10: Drying capacity of fabrics

3.3 Optimisation of fabric properties through desirability function

Today, multi-response optimisation is a suitable method for overcoming the problem of conflicting responses of single response optimisation. Under this optimisation technique, the desired weight is given to all responses (equal weight in the present study) for varying values of input parameters to calculate the combined impact of all desirability responses. Parameters are set to enhance fabric quality according to customers' demands. Figures 11–14 show the curves of various factors (all six responses

are given equal weights) for untreated fabric with machine-spun yarn as a weft, treated fabric with machine-spun yarn as a weft, untreated fabric with hand-spun yarn as a weft and treated fabric with hand-spun yarn as a weft respectively.

The parameters required to maximise overall desirability involve the percentages of fibres presented in Table 5 for different treated and untreated fabrics with machine-spun and hand-spun yarn as a weft.

Table 5: Percentage of fibres in weft with maximum desirability for different types of fabrics

Fabric	Fibres content in weft		
	Polyester (%)	Merino wool (%)	PVAL (%)
BT fabric	20	70	10
AT fabric	35	55	10
BTH fabric	20	70	10
ATH fabric	30	60	10

The illustrations above (Figure 15 a–d) show the overall desirability for BT, AT, BTH and ATH fabrics respectively. Harrington's rating system was used to interpret desirability values. The overall desirability value for BT fabric was 0.65 (Figure 15 a) and 0.73 for AT fabric (Figure 15 b). It means that after the dissolution of PVAL, there was an improvement in overall desirability for fabric with machine-spun yarn as a weft, while in the case of fabric with hand-spun yarn as a weft, the overall desirability value remained approximately the same (0.66 and 0.67 for BTH and ATH respectively) as shown in Figure 10 c and d respectively. According to the Harrington standard, this threshold indicates that product quality is acceptable with regard to the specifications for BT, AT, BTH and ATH fabrics. The overall desirability bar graph for BT fabric (Figure 15 a) indicates that all responses are acceptable, but that the individual desirability values of bending rigidity (0.42) and drying capacity (0.25) require some improvement. Effectively, for AT fabric, the individual desirability value for all responses was good, except for thermal resistance, which requires a small improvement according to the Harrington standard, as shown in Figure 15 b.

As evident in Figure 15 c, the individual desirability values for BTH fabric for different properties, such as air permeability, water vapour permeability, bending rigidity and compressibility, are 0.72, 0.79, 0.66 and 0.74 respectively, and are also acceptable according to the Harrington standard, while the individual desirability values for thermal resistance and drying capacity were 0.51 and 0.57, which are also acceptable but still require some improvement.

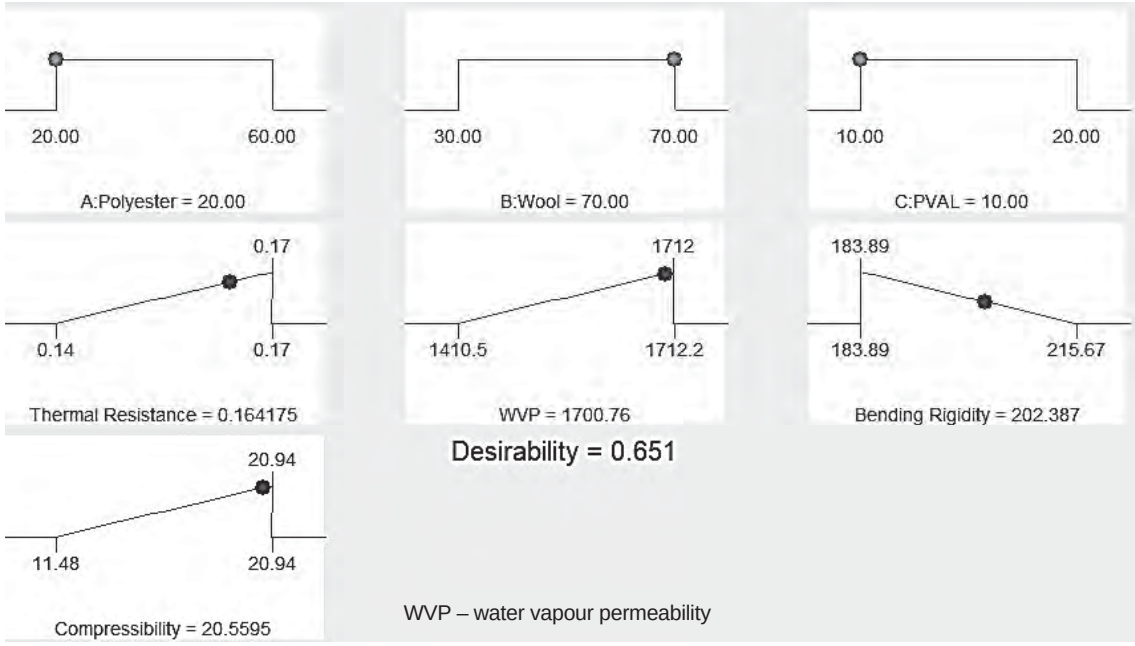

Figure 11: Curves of various factors for untreated fabric with machine-spun yarn as a weft

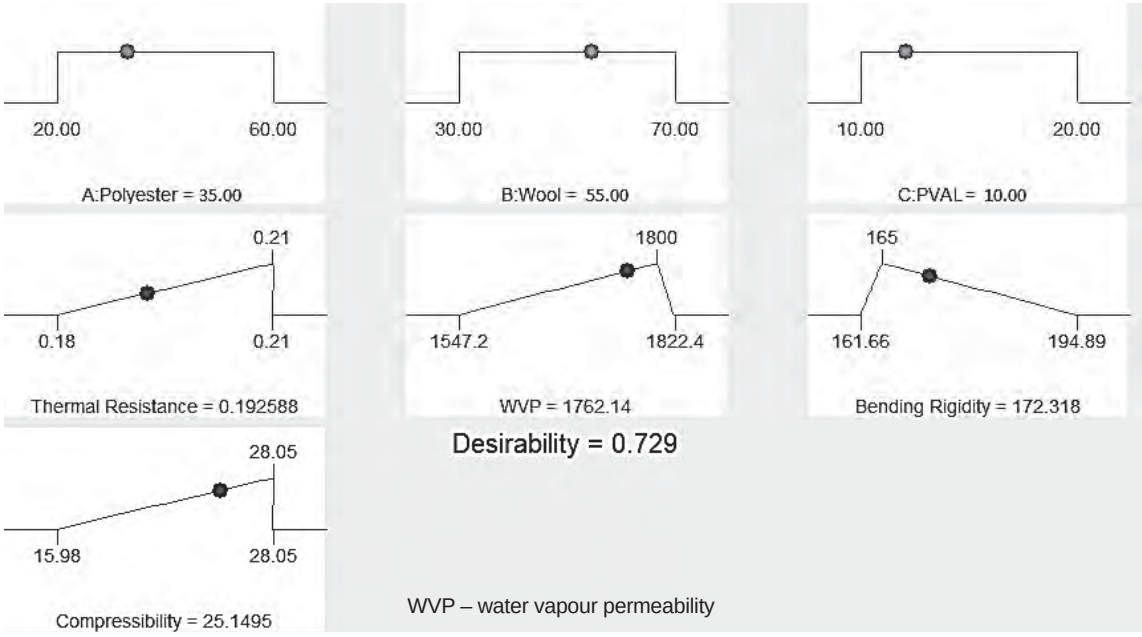

Figure 12: Curves of various factors for treated fabric with machine-spun yarn as a weft

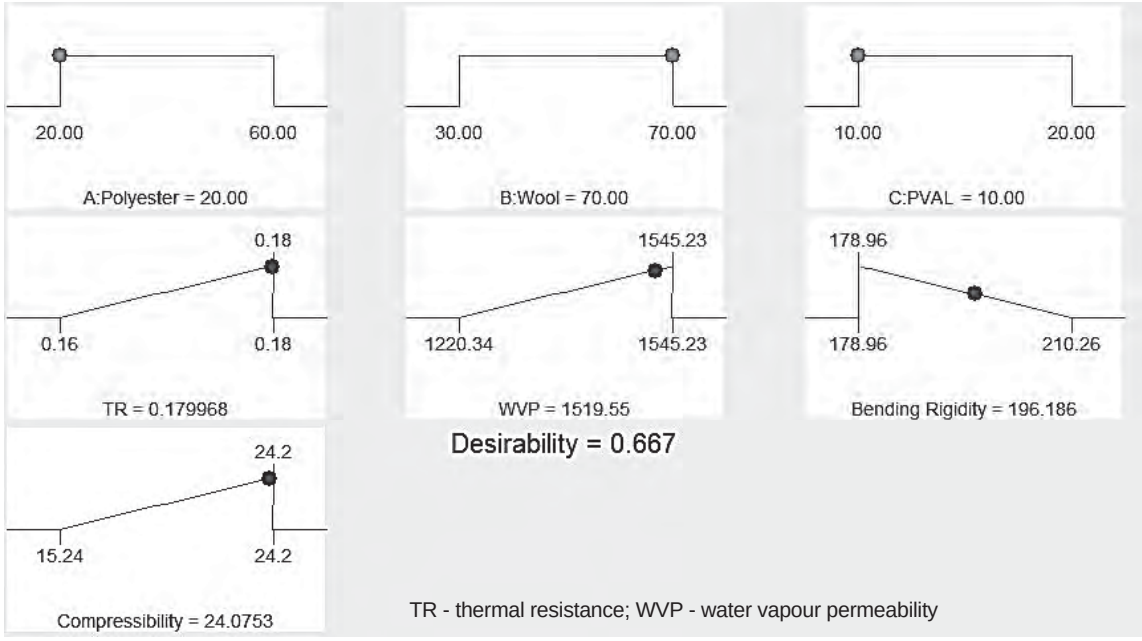

Figure 13: Curves of various factors for untreated fabric with hand-spun yarn as a weft

It is evident from Figure 15 d that all responses for ATH fabric exhibited excellent individual desirability values, except bending rigidity (0.49), which requires some improvement, and drying capacity (0.29), which requires more improvement.

4 Conclusion

This study addressed the effect of hand-spun and machine-spun weft yarns, before and after treatment, on different properties that influence the thermo-physiological behaviour of fabric. A fabric with hand-spun

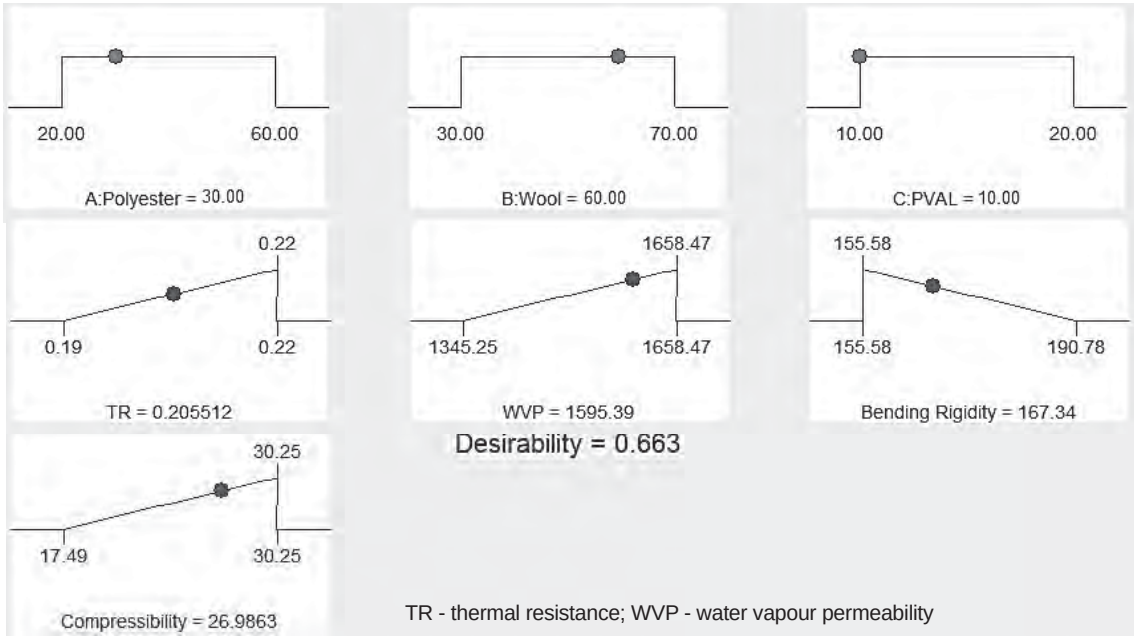

Figure 14: Curves of various factors for treated fabric with hand-spun yarn as a weft

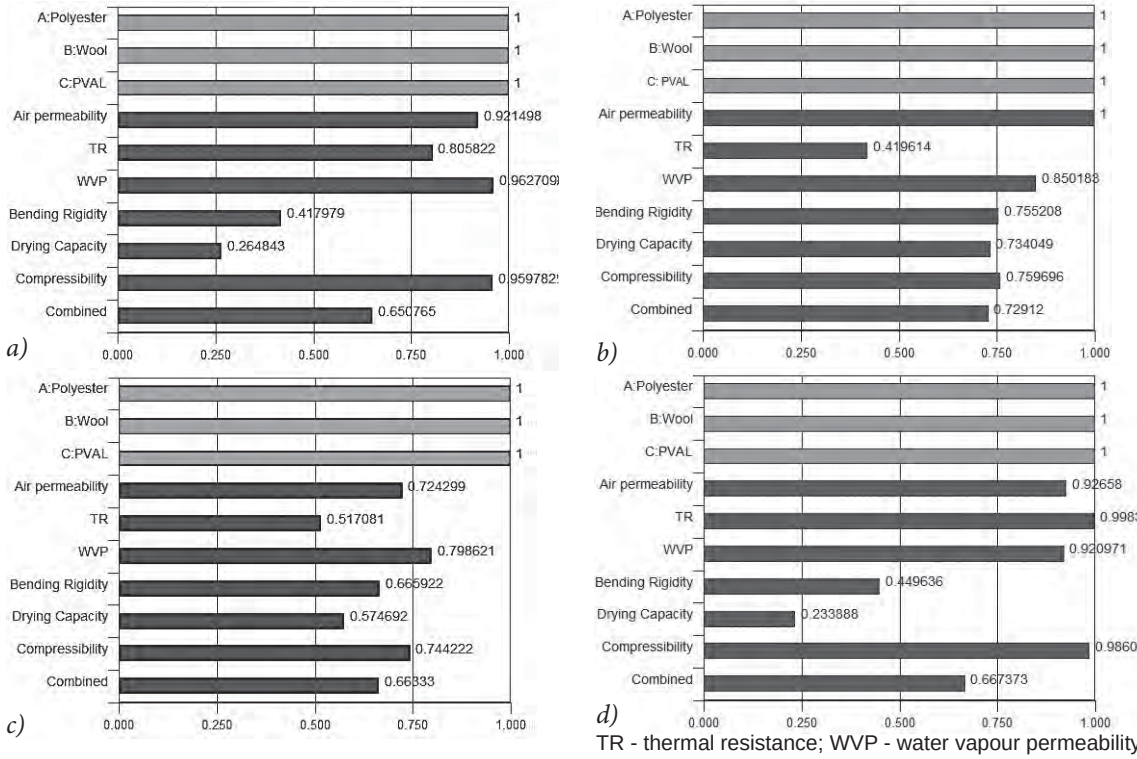

Figure 15: Overall desirability: a) BT, b) AT, c) BTH and d) ATH

yarn as a weft exhibited higher values of thermal resistance, bending rigidity, compressibility and drying capacity, while air permeability and water vapour permeability values were lower than fabrics with machine-spun yarn as a weft. After the dissolution of the PVAL component, thermal resistance, compressibility, water vapour permeability and drying capacity increased due to the creation of pores in

the structure of both AT and ATH fabrics. Optimisation using a multi-response technique was also performed to identify the suitable percentage of fibres to achieve maximum desirability for customers for different fabric properties. Results for optimisation indicate that the same desirability (0.65) can be achieved for both fabrics, either machine-spun or hand-spun, in the same blend composition. After the dissolution of PVAL, fibres in the case of AT fabrics exhibited an improved desirability value (0.73), as well as a change in the percentage of wool (55%) in the blend composition relative to BT fabric (70%). After the treatment of fabric with hand-spun yarn as weft, there was no change in desirability values, but there was a reduction in the percentage of wool (60%) in the blend composition relative to BTH fabric (70%).

References

1. SHARMA, N., KUMAR, P., BHATIA, D., SINHA, S.K. Moisture management behaviour of knitted fabric from structurally modified ring and vortex spun yarn. *Journal of The Institution of Engineers (India): Series E*, 2016, **97**(2), 123–129, doi:10.1007/s40034-015-0075-z.
2. BHATIA, D., MALHOTRA, U., MALHOTRA, A. Impact on properties of woven fabric from structurally modified shoddy/wool blended worsted yarn. *Journal of Fashion Technology & Textile Engineering*, 2016, **4**(1), 1–6, doi: 10.4172/2329-9568.1000128.
3. SINHA, S.K., KUMAR, P., GHOSH, S. Study on the packing density of structurally modified ring spun yarn. *Fibres and Polym*ers, 2016, **17**(11), 1898–1907, doi:10.1007/s12221-016-5940-y.
4. DAS, A., ISHTIAQUE, S.M., SINGH, R.P. Packing of micro-porous yarns. Part II : Optimization of fabric characteristics. *Journal of the Textile Institute*, 2009, **100**(3), 207–217, doi:10.1080/00405000701559917.
5. CHANDRASEKARAN, V., SENTHILKUMAR, P., KARTHIK, T. Optimization of spinning parameters influencing the characteristics of structurally modified viscose yarn. *Journal of the Textile Institute*, 2016, **107**(1), 50–63, doi:10.1080/00405000.2014.1000017.
6. GHAREHAGHAJI, A.A., MOGHASSEM, A.R. Redistribution of fibres in the structure of hollow ring spun yarn. *International Journal of Engineering, Transactions B: Applications*, 2009, **22**(2), 197–204.
7. ERIKSSON, L., JOHANSSON, E., KETTANEHWOLD, N., WIKSTRÖM, C., WOLD, S. Design of experiments : principles and applications. Umeå : Umetrics Academy, 2000.
8. BAYKAL, P.D., BABAARSLAN, O., EROL, R. Prediction of strength and elongation properties of cotton/polyester-blended OE rotor yarns. *Fibres & Textiles in Eastern Europe*, 2006, **14**(1), 18–21.
9. PAL, S., GAURI, S.K. A desirability functions-based approach for simultaneous optimization of quantitative and ordinal response variables in industrial processes. *International Journal of Engineering, Science and Technology (IJEST)*, 2018, **10**(1), 76–87, doi:10.4314/ijest.v10i1.6.
10. DERRINGER, G., SUICH, R. Simultaneous optimization of several response variables. *Journal of Quality Technology*, 1980, **12**(4), 214–219. doi: 10.1080/00224065.1980.11980968.
11. VINING, G.G., MYERS, R.H. Combining taguchi and response surface philosophies : a dual response approach. *Journal of Quality Technology*, 1990, **22**(1), 38–45, doi:10.1080/00224065.1990.11979204.
12. KUMAR, P., BARUA, P.B., GAINDHAR, J.L. Quality optimization (multi-characteristics) through Taguchi's technique and utility concept. *Quality and Reliability Engineering International*, 2000, **16**(6), 475–485, doi: 10.1002/1099-1638-(200011/12)16:6<475::AID-QRE342>3.0.CO;2-0.
13. GHOSH, A., MAL, P., MAJUMDAR, A., BANERJEE, D. Optimization of knitted fabric comfort and UV protection using desirability function. *Journal of Engineered Fibers and Fabrics*, 2016, **11**(4), 20–28, doi:10.1177/155892501601100404.
14. GUPTA, S.K., GOSWAMI, K.K., MAJUMDAR, A. Optimization of durability of Persian hand-knotted wool carpets by using desirability functions. *Textile Research Journal*, 2018, **88**(1), 89–98, doi:10.1177/0040517516676056.
15. HADJ TAIEB, A., MSAHLI, S. Optimization of the knitted fabric quality by using multicriteria phenomenon tools. *International Journal of Fiber and Textile Research*, 2013, **3**(4), 66–77.
16. ASIM, F, MAHMOOD, M, SIDDIQUI, M, A. Optimization of process parameters for simultaneous fixation of reactive printing and crease resistant finishing using desirability function. *Journal of Textile and Apparel, Technology and Management*, 2012, **7**(3), 1–12.

Ivana Bonić[1], Andrea Palac[1], Ana Sutlović[2], Branka Vojnović[1], Mario Cetina[1]
[1] University of Zagreb, Faculty of Textile Technology, Department of Applied Chemistry, Prilaz baruna Filipovića 28a, HR-10000 Zagreb, Croatia
[2] University of Zagreb, Faculty of Textile Technology, Department of Textile Chemistry and Ecology, Savska c. 16/9, HR-10000 Zagreb, Croatia

Removal of Reactive Black 5 dye from Aqueous Media using Powdered Activated Carbon – Kinetics and Mechanisms

Odstranjevanje barvila Reactive Black 5 iz vodnih medijev z uporabo praškastega aktivnega oglja – kinetika in mehanizmi

Original scientific article/*Izvirni znanstveni članek*
Received/*Prispelo* 3-2020 • Accepted/*Sprejeto* 5-2020

Abstract

The textile industry is considered one of the major environmental polluters, primarily due to the quantity and composition of wastewater. It is therefore important to examine its different treatment methods. For this purpose, the isothermal adsorption of Reactive Black 5 dye on powdered activated carbon at 25(±1) °C and 45(±1) °C was carried out to determine the effect of initial dye concentration, contact time and temperature on the adsorption process. In order to investigate the mechanism of adsorption of Reactive Black 5 dye on activated carbon, kinetic studies have also been carried out. Experimental data were analysed using a pseudo-first-order and pseudo-second-order kinetic models, as well as an intraparticle diffusion model. Standard Gibbs free energy values of the adsorption process were also calculated, while the morphological analysis of activated carbon before and after adsorption was performed using a scanning electron microscope. The efficiency of activated carbon as an adsorbent for Reactive Black 5 dye is evidenced by the fact that more than 60% of dye is adsorbed after 30 minutes regardless of initial concentration and temperature. The experimental data also showed that adsorption is kinetically controlled assuming a pseudo-second-order process, and that intraparticle diffusion is not the only process that influences the adsorption rate. Negative values of standard Gibbs free energy indicate that the adsorption reaction is spontaneous, while a higher negative value for temperature of 45 °C compared to 25 °C shows that a higher temperature is more energetically favourable for the adsorption of Reactive Black 5.
Keywords: adsorption, activated carbon, Reactive Black 5, kinetics, intraparticle diffusion

Izvleček

Tekstilna industrija velja za eno glavnih onesnaževalk okolja, predvsem zaradi količine in sestave odpadnih voda, zato je pomembno preučiti različne metode njihove obdelave. V ta namen je bila izvedena izotermična adsorpcija barvila Reactive Black 5 na praškasto aktivno oglje pri 25 °C ± 1 °C in 45 °C ± 1 °C, da bi ugotovili vpliv začetne koncentracije barvila, časa stika in temperature na postopek adsorpcije. Za preučitev mehanizma adsorpcije barvila Reactive Black 5 na aktivno oglje so bile izvedene tudi študije kinetike. Eksperimentalni podatki so bili analizirani s kinetičnimi modeli psevdo prvega in psevdo drugega reda, kot tudi z modelom difuzije delcev snovi. Za proces adsorpcije je bila določena standardna Gibbsova prosta energija. Morfološka analiza aktivnega oglja je bila izvedena z rastrskim elektronskim mikroskopom. Učinkovitost aktivnega oglja kot adsorbenta za barvilo Reactive Black 5 je razvidna iz dejstva, da se je več kot 60-odstotkov barvila adsorbiralo po 30 minutah, ne glede na začetno koncentracijo in temperaturo. Eksperimentalni podatki so pokazali tudi, da je adsorpcija

Corresponding author/*Korespondenčni avtor:*
Prof. dr. Mario Cetina
E-mail: mario.cetina@ttf.unizg.hr
ORCID: 0000-0001-7524-5828

Tekstilec, 2020, ***63****(2), 151-161*
DOI: 10.14502/Tekstilec2020.63.151-161

kinetično nadzorovana, pri čemer se predpostavlja proces psevdo drugega reda in da difuzija delcev ni edini proces, ki vpliva na hitrost adsorpcije. Negativne vrednosti standardne Gibbsove proste energije nakazujejo, da je reakcija adsorpcije spontana, višja negativna vrednost pri temperaturi 45 °C v primerjavi s 25 °C pa kaže, da je višja temperatura energijsko ugodnejša za adsorpcijo barvila Reactive Black 5.
Ključne besede: adsorpcija, aktivno oglje, Reactive Black 5, kinetika, difuzija delcev

1 Introduction

At the end of the 20th century, with all of the inventions and technical aids used every day, the relationship between man and nature was disrupted, and the Earth's ecosystem broken. Due to human knowledge and creativity over the last 250 years, a modern way of life, industrial development, advancing technology and agriculture, the use of large amounts of energy and natural resources, as well as the pursuit of a better and more comfortable life have led to the emergence of environmental hazards and their consequences (i.e. acid rain, desertification, ozone depletion, climate change and other harmful phenomena). A great deal of attention worldwide has been given to environmental protection, the effect of harmful substances on human health and the entire ecosystem. Particular attention is given to industry, as it is no longer possible to continue expanding production and waste accumulation without inflicting permanent damage to nature.

The textile industry is one of the major environmental polluters. It uses significant quantities of water [1], which is eliminated as wastewater after being processed. Taking into account total industrial water pollution, textile finishing is considered one of the largest water consumption and pollution processes. The quantity and composition of wastewater depend on the type of basic raw material being processed (cotton, wool, flax, silk, synthetic fibres, blends, etc.) and textile finishing process used (laundering, bleaching, dyeing, printing, etc.), i.e. the type of chemicals used during some processes and the number of consecutive processes during production. In addition, the use of certain special finishing agents often results in specific and greater pollution of wastewater. Textile industry wastewater has a wide range of pH values and temperatures, it may be coloured and mainly contains various types of pollutants, most commonly dyes, surfactants, pesticides, oils, fats, solvents, heavy metals, inorganic salts, waste fibres, etc. [2]. Special attention is given to dyes and pigments because they are highly visible materials so that even the minimum amount released into the environment may cause the appearance of colour in open waters. Besides being aesthetically deficient, coloured water prevents the penetration of light into natural water, which negatively affects the entire natural water ecosystem, i.e. organisms depending on water quality. There are more than 100,000 commercially available dyes with over 700,000 tonnes produced annually. Wastewater stream from the textile dyeing process contains unutilised dyes (about 8–20% of the total pollution load due to incomplete dye exhaustion) and auxiliary chemicals [3]. Besides, some dyes have been proven to have allergenic, toxic and/or carcinogenic properties that make them not only dangerous or potentially harmful to the environment, but also to human health in contact with human skin [4]. The continuous monitoring of dye content in wastewaters should therefore be an integral part of the technological process of textile materials and permitted concentrations regulated by law. Dyeing and printing should be carried out by achieving the maximum effect using a minimum amount of dye, not only for ecological reasons (reduced quantity of unused textile auxiliaries in wastewater), but also for economic reasons.

Taking all of the above-mentioned facts into consideration, it is necessary to treat the wastewater by reducing the amount of harmful substances to legally limited concentrations. There are numerous methods for the treatment and disposal of textile industry wastewater: coagulation and flocculation, chemical oxidation, biological treatment, membrane separation, reverse osmosis, etc. [3, 5, 6]. Although high quality effluents can be obtained through water treatment with each of the previously mentioned processes, some of them have limitations/disadvantages, such as the use of excess chemicals, the formation of larger amounts of sludge that needs adequate care, and the incomplete removal of colour. Removal of dyes from wastewater is generally difficult. They are usually non-biodegradable, resistant to aerobic digestion,

and stable to light, heat and oxidising agents. One of the most commonly used and effective treatment methods for coloured water is adsorption, which is based on the accumulation of the substance from the solution in a solid phase. Adsorption is one of the best treatment methods due to its flexibility, simplicity of design, and sensitivity to toxic pollutants. Furthermore, adsorption generally does not result in the formation of harmful substances [3, 7–9]. Activated carbon is the most popular adsorbent used for wastewater treatment due to its adsorption efficiency and great capacity, although some other adsorbents are less expensive and easily available. It is efficient in the removal of different types of dyes, including reactive dyes [10–15].

It is known that adsorption is a time-dependent process, and it is therefore necessary to know the adsorption rate for removal of dyes from wastewater. The most important factor in the design of adsorption systems is thus prediction of the rate of adsorption for a given system. This paper aims to present adsorption efficiency of commercial activated carbon for the removal of Reactive Black 5 dye (RB5). The effect of contact time, initial dye concentration and temperature on adsorption were monitored. The pseudo-first-order and pseudo-second-order models were used to correlate the adsorption kinetic data, while intraparticle diffusion was used to evaluate the diffusion mechanism of the adsorption process. Activated carbon was also characterised before and after the adsorption of RB5 using a scanning electron microscope.

2 Materials and methods

2.1 Materials

Reactive Black 5 dye (Drimarene Black R-3B, supplied by Clariant GmbH, C.I. 20505, chemical formula: $C_{26}H_{21}N_5Na_4O_{19}S_6$, M_r = 991.82), was used for the adsorption experiment. The chemical structure of the dye prepared by the Accelrys Draw program is shown in Figure 1. One thousand milligrams per litre stock solution of dye was prepared by dissolving the required amount of dye in deionised water. The solutions of appropriate concentrations were prepared by diluting the stock solution with deionised water. Powdered activated carbon was purchased from the Croatian company Kemika. Adsorbent was dried in an oven at 105 °C for 24 hours and stored in a desiccator until it was used.

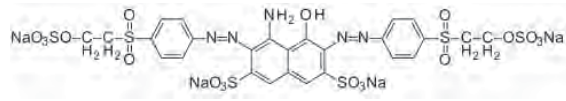

Figure 1: Chemical structure of Reactive Black 5

2.2 Batch mode adsorption studies

Adsorption studies were conducted by contacting 50 ml of dye solution of different initial concentrations (c_0 = 300, 500 and 700 mg/dm^3) with 0.2 g of activated carbon in glass bottles. The experiments were repeated three times under identical conditions to confirm their repeatability. Experimental points presented in figures are the average values of three the repetitions. Suspensions were shaken at different contact times (15, 30, 45, 60, 90, 120, 180, 240 and 360 minutes and 16 hours until equilibrium was reached) with an impeller speed of 250 rpm at 25(±1) °C and 45(±1) °C (Heidolph Unimax 1010 with Incubator 1000). Experiments after 360 minutes for initial concentration of c_0 = 300 mg/dm^3 were not performed due to extremely low dye concentration after an adsorption time of 240 minutes. Suspensions were filtered after agitation through filter-paper blue ribbon. The residual liquid-phase dye concentration after adsorption was determined spectrophotometrically by monitoring the absorbance using a UV–Vis spectrophotometer (Lambda 20, Perkin Elmer) at a maximum absorbance wavelength (λ_{max} = 598 nm). The calibration graph of absorbance versus concentration followed a linear Beer-Lambert relation.

The amount of adsorbate adsorbed at any time t, q_t (mg/g), and the amount of adsorbate adsorbed at equilibrium, q_e (mg/g), were calculated using the following equation:

$$q = \frac{v \cdot (c_0 - c_t)}{m} \quad (1),$$

where c_0 (mg/dm^3) represents the initial dye concentration, c_t (mg/dm^3) represents the dye concentration in the liquid phase after appropriate time of adsorption and when equilibrium is reached (t = 16 hours), V represents the volume of the liquid phase (dm^3), and m represents the mass of the adsorbent (g).

Percentage of adsorbed dye (% ads.) is calculated using the equation:

$$\%\ ads. = \frac{c_s}{c_0} \times 100 \quad (2),$$

where c_s (mg dm^{-3}) represents the concentration of the adsorbed dye in a solid phase ($c_s = c_0 - c_t$).

2.3 Morphological analysis of adsorbent and dye-adsorbent samples

A field emission scanning electron microscope (Mira, Tescan) was used for visualization of the adsorbent's morphology before and after adsorption. The accelerating voltage was 10.00 kV, while scanning was performed in situ on a sample powder. Samples were pre-coated with gold/palladium in a sputter coater. Optical micrographs were recorded using a Nikon Elipse E 400 microscope.

3 Results and discussion

3.1 Effect of contact time, temperature and initial dye concentration on the adsorption process

The objective of this work was to assess the effectiveness of activated carbon for the treatment of

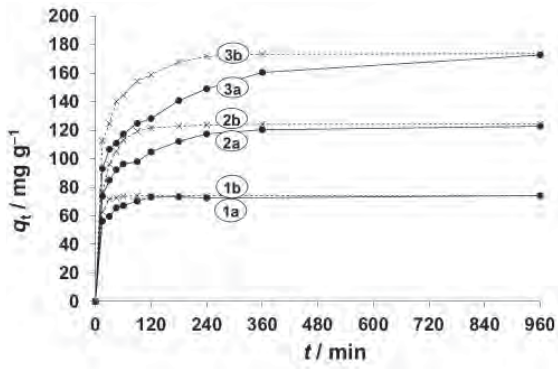

Figure 2: Effect of initial concentration and temperature on the amount of adsorbed RB5 on activated carbon after appropriate time (initial concentrations, c_0: ① 300 mg/dm^3, ② 500 mg/dm^3, ③ 700 mg/dm^3; temperatures: a) 25 °C, b) 45 °C)

Table 1: Percentage of adsorbed RB5 (% ads.) and amount of adsorbed RB5 at any time t (q_t) for three initial dye concentrations (c_0) at both temperatures

T (°C)	t (min)	c_0 = 300 mg/dm^3		c_0 = 500 mg/dm^3		c_0 = 700 mg/dm^3	
		% *ads.*	q_t (mg/g)	% *ads.*	q_t (mg/g)	% *ads.*	q_t (mg/g)
25	15	74.9	56.2	59.0	73.8	53.2	93.1
	30	79.5	59.6	68.0	85.0	60.9	106.6
	45	87.4	65.6	73.9	92.3	63.3	110.8
	60	89.6	67.2	76.9	96.2	67.0	117.2
	90	93.7	70.3	78.3	97.9	71.2	124.7
	120	97.5	73.1	83.9	104.8	73.2	128.1
	180	97.7	73.3	89.7	112.1	80.4	140.7
	240	96.5	72.4	93.9	117.4	85.1	148.9
	360 [a]	---	---	96.1	120.2	91.7	160.4
	960	98.8	74.1	98.2	122.7	98.6	172.6
45	15	83.8	62.8	61.2	76.5	64.2	112.5
	30	95.4	71.6	76.9	96.1	71.2	124.6
	45	96.6	72.5	84.1	105.1	80.0	140.0
	60	98.1	73.6	90.4	113.1	82.5	144.4
	90	98.7	74.0	95.4	119.3	88.2	154.3
	120	98.7	74.0	97.2	121.5	90.7	158.7
	180	99.0	74.2	98.2	122.8	95.9	167.8
	240	98.7	74.0	98.8	123.6	98.0	171.5
	360 [a)]	---	---	99.3	124.1	98.9	173.2
	960	98.7	74.0	99.4	124.3	99.2	173.6

[a)] *Due to extremely low dye concentration after the adsorption time of 4 hours, an adsorption experiment after 6 hours for initial concentration of c_0 = 300 mg/ dm^3 was not performed*

dye-rich textile wastewater with special focus on the reduction of colour polluters. The initial concentration of RB5 varied from 300 to 700 mg/dm^3, which is a possible range of dye concentration in textile industry wastewater after the process of dying. The dependence of the amount of adsorbate adsorbed after appropriate time (q_t) versus time (t) is presented in Figure 2, while data are given in Table 1.

It is evident from Figure 2 that a higher initial concentration of the dye increases the adsorption capacity and that the amount of adsorbed RB5 is higher at higher temperature for all concentrations. As equilibrium for the initial concentration c_0 = 300 mg/dm^3 was reached very quickly, the amount of adsorbate adsorbed was monitored from 15 minutes to 4 hours, while for the other two initial concentrations were monitored from 15 minutes to 6 hours. The plots can be approximately divided into three regions. The first region includes a very fast initial adsorption, probably governed by a rapid external diffusion process, which mainly includes adsorption of dye on the surface of activated carbon. After this step follows the second region, with a milder and gradual increase of adsorbed dye, and the third region where a state of equilibrium was almost reached.

The sorption capacity at equilibrium at both temperatures increased from *ca*. 74 to *ca*. 173–174 mg/g with an increase of the initial dye concentration from 300 to 700 mg/dm^3 (Table 1). Initially, differences in adsorbed RB5 between two temperatures for the same initial dye concentration were more significant, while after a longer period of adsorption, quantities of adsorbed RB5 became very similar. Also, as expected, less time was needed to obtain high dye adsorption percentage values for lower concentrations of dye (Figure 3). Thus, approximately 90% of RB5 was adsorbed at 25 °C for initial concentrations of c_0 = 300, 500 and 700 mg/dm^3 after 1, 3 and 6 hours, respectively (Table 1). At 45 °C, these times are significantly shorter, and they were between 15 and 30 minutes for c_0 = 300 mg/dm^3, 1 hour for c_0 = 500 mg/dm^3 and 2 hours for c_0 = 700 mg/dm^3. The efficiency of activated carbon for the adsorption of RB5 is also evidenced by the fact that more than 60% of dye is adsorbed after 30 minutes, regardless of initial concentration and temperature.

3.2 Kinetics of adsorption

Kinetic studies were performed in order to investigate the mechanism of adsorption and potential rate controlling steps. Kinetic study is important to an adsorption process because it depicts the uptake rate of the adsorbate and controls the residual time of the whole adsorption process for a given system. The experimental data were analysed using three kinetic models: pseudo-first-order and pseudo-second-order kinetic models, and an intraparticle diffusion model. The pseudo-first-order and pseudo-second-order models are used most frequently for determining of kinetic parameters.

Pseudo-first-order kinetic model

Lagergren [16] proposed a rate equation for the sorption of solute from a liquid solution based on solid capacity. The kinetic model of this the most widely used rate equation is expressed using the following equation:

$$\frac{dq_t}{dt} = k_1 (q_e - q_t) \quad (3),$$

where k_1 represents the rate constant of the pseudo-first-order (min^{-1}).

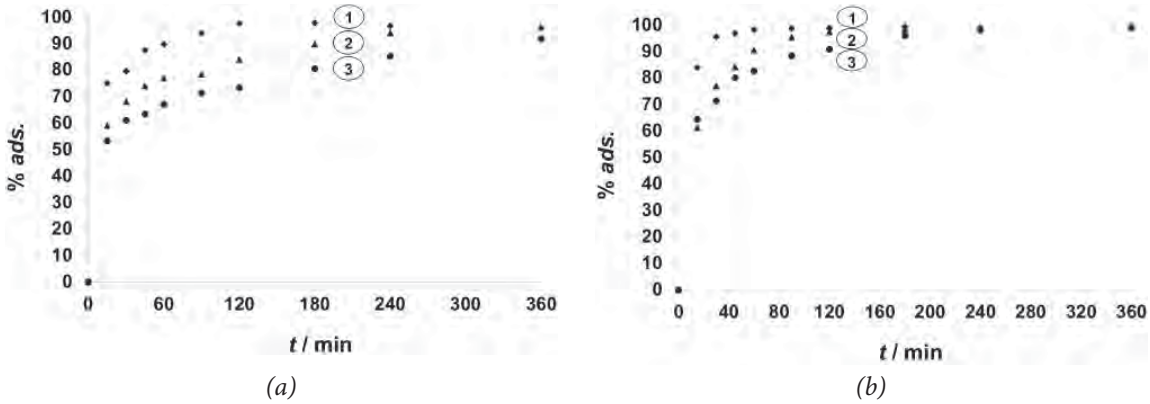

Figure 3: Effect of initial concentration on percentage of adsorbed RB5 (% ads.) at temperatures of (a) 25 °C and (b) 45 °C (initial concentrations, c_0: ① 300 mg/dm^3, ② 500 mg/dm^3, ③ 700 mg/dm^3)

Integrating this equation for the boundary conditions $t = 0$ to $t = t$ and $q_t = 0$ to $q_t = q_t$ results in:

$$\ln(q_e - q_t) = \ln q_e - k_1 \cdot t \quad (4).$$

The kinetic constant k_1 can be determined by plotting $\ln(q_e - q_t)$ against time (t), and if the first-order equation is applicable, the plot should give a linear relationship, and facilitates the calculation of the rate constant of pseudo-first-order (k_1) from the slope and amount of adsorbate adsorbed at equilibrium ($q_{e,calc}$) from the intercept. The values of the constants of the pseudo-first-order model for adsorption of RB5 onto activated carbon are given in Table 2.

The values of the correlation coefficient (R^2) obtained from the linear plot (Eq. 4) are relatively high (from 94.6% to 99.8%), the exception being the initial concentration of c_0 = 300 mg/dm^3 at 25 °C (71.1%). However, for all concentrations and at both temperatures, there is considerable disagreement between the experimental and calculated values of the amount of adsorbed RB5 at equilibrium ($q_{e,exp}$ and $q_{e,calc}$). This suggests that this sorption system is not a first-order reaction and that a pseudo-second-order model might provide a better correlation of the data.

Pseudo-second-order kinetic model

Ho and McKay [17, 18] developed a second-order equation based on adsorption capacity. This kinetic model is illustrated by the following equation:

$$\frac{dq_t}{dt} = k_2 (q_e - q_t)^2 \quad (5),$$

where k_2 represents the rate constant of the pseudo-second-order (g mg^{-1} min^{-1}).

Integrating the equation (5) for the same boundary conditions used for the first-order results in the equation presented below in the linear form:

$$\frac{t}{q_t} = \frac{1}{k_2 \cdot q_e^2} + \frac{1}{q_e} \cdot t \quad (6).$$

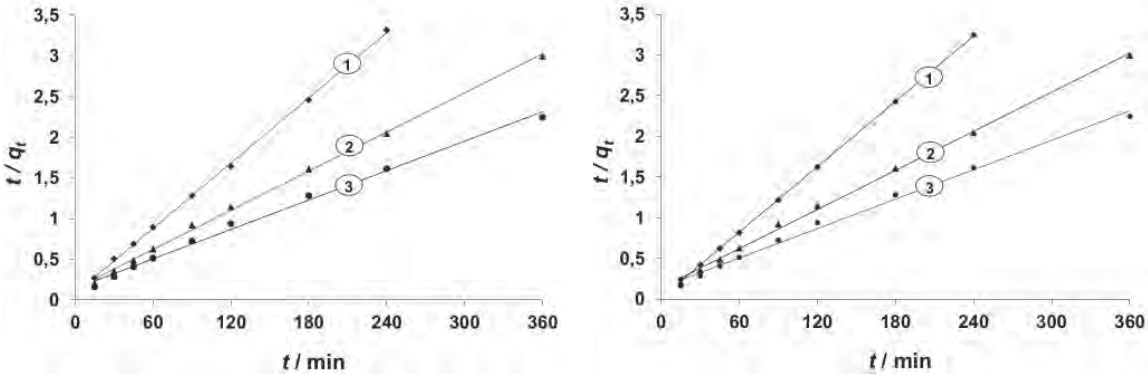

Figure 4: Pseudo-second-order kinetic model for three initial concentrations of RB5 at temperatures of (a) 25 °C and (b) 45 °C (initial concentrations, c_0: ① 300 mg/dm^3, ② 500 mg/dm^3, ③ 700 mg/dm^3)

Table 2: Kinetic parameters for the effect of initial dye concentration on adsorption at temperatures of 25 °C and 45 °C

T (°C)	c_0 (mg/dm^3)	$q_{e,exp}$ (mg/g)	Pseudo-first-order model			Pseudo-second-order model			
			$q_{e,calc}$ (mg/g)	R^2	k_1 (min^{-1})	$q_{e,calc}$ (mg/g)	R^2	k_2 (g mg^{-1} min^{-1})	h (mg g^{-1} min^{-1})
25	300	74.1	14.3	0.7108	0.0129	74.6	0.9995	0.002295	12.77
	500	122.7	48.6	0.9888	0.0085	125.0	0.9983	0.000463	7.23
	700	172.6	79.4	0.9948	0.0052	166.7	0.9944	0.000252	7.00
45	300	74.0	26.1	0.9656	0.0674	74.6	0.9999	0.009075	50.51
	500	124.3	32.5	0.9463	0.0154	128.2	0.9998	0.000935	15.36
	700	173.6	72.9	0.9975	0.0145	178.6	0.9997	0.000437	13.95

If the pseudo-second-order equation is applicable, the plot of t/q_t against time t should give a linear relationship and facilitates the calculation of the amount of adsorbate adsorbed at equilibrium ($q_{e,calc}$) from the slope, and then the rate constant of the pseudo-second-order (k_2) from the intercept. The values are given in Table 2, while linear plots are presented in Figure 4.

Based on this model, calculated q_e values ($q_{e,calc}$) and experimental equilibrium values ($q_{e,exp}$) demonstrate a much better correlation (Table 2). Moreover, the values of correlation coefficients are very close to 1 (higher than 99.4%) for all initial dye concentrations and at both temperatures. Figure 5 shows the good correlation of the data with the pseudo-second-order equation. The experimental points are shown together with the theoretically generated lines, and they fit nicely for all concentrations and at both temperatures, although slightly better for the temperature of 45 °C. The adsorption of RB5 dye on commercial activated carbon is thus kinetically controlled assuming a pseudo-second-order rather than a pseudo-first-order process. The pseudo-second-order model assumes chemical sorption or chemisorption as the rate-limiting process. Maximum k_2 values were obtained for the smallest initial dye concentration (c_0 = 300 mg/dm^3), while values for temperature of 45 °C are approximately 2–4 times higher than those for 25 °C.

Also, as time approaches zero, according to the pseudo-second-order model, the initial adsorption rate h (mg g^{-1} min^{-1}) can be calculated using the following equation [18, 19]:

$$h = k_2 \cdot q_{e,calc}^2 \quad (7).$$

The obtained h values are also presented in Table 2. As for k_2, values of the initial adsorption rate increase with a decrease of initial dye concentration, and increase with an increase in temperature.

Intraparticle diffusion model

We used an intraparticle diffusion model to evaluate the diffusion mechanism for adsorption of RB5 on activated carbon. Most adsorption reactions are carried out using a multistep mechanism and involve several steps:

(i) external mass transfer of the adsorbate from the solution to the adsorbent surface;
(ii) adsorption at a site on the adsorbent surface; and
(iii) intraparticle diffusion of the adsorbate in the pores of the adsorbent and adsorption on the site.

Step (ii) is often assumed to be very fast, and thus cannot be treated as a rate limiting step. Generally, the rate of adsorption is limited by external mass transfer for a system with poor mixing, low adsorbate concentration, its high affinity to the adsorbent and the small adsorbents particles. The adsorption of large molecules, for which longer contact time is needed to reach equilibrium, is always considered to be diffusion controlled by external film resistance and/or internal diffusion mass transport or intraparticle diffusion [20].

Theoretical treatments of intraparticle diffusion yield complex mathematical relationships that differ in form as functions of the geometry of the adsorbent particle. The intraparticle diffusion model is based on the following equation [19, 20]:

$$q_t = k_i \cdot t^{0.5} \quad (8),$$

where k_i represents the intraparticle diffusion rate constant (mg g^{-1} min$^{-0.5}$).

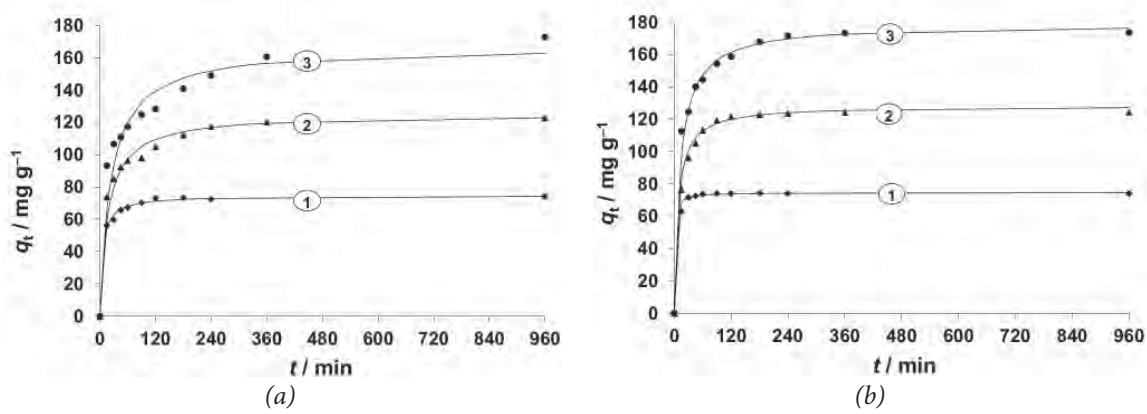

Figure 5: Fitting of pseudo-second-order kinetic model with experimental data at temperatures of (a) 25 °C and (b) 45 °C (initial concentrations, c_0: ① 300 mg/dm^3, ② 500 mg/dm^3, ③ 700 mg/dm^3)

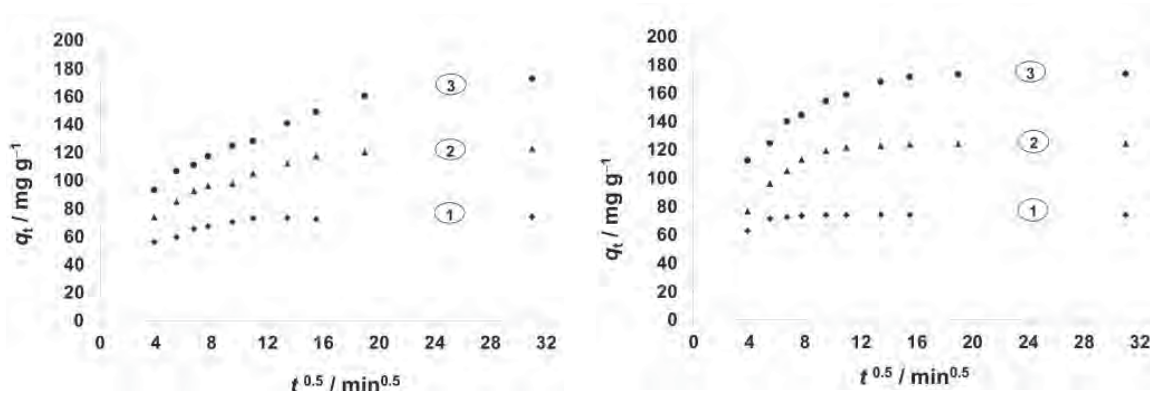

(a) (b)

Figure 6: Root time plots for the adsorption of RB5 for three initial dye concentrations (c_0: ① 300 mg/dm³, ② 500 mg/dm³, ③ 700 mg/dm³) at temperatures of (a) 25 °C and (b) 45 °C

If the intraparticle diffusion is a rate limiting step of adsorption, *i.e.* intraparticle diffusion controls the rate of adsorption, then plot q_t versus $t^{0.5}$ should be linear and pass through the origin. If the plot of q_t versus $t^{0.5}$ exhibit multi-linearity, this indicates that two or more rate controlling steps occur in the adsorption processes [20–22]. Figure 6 shows the root time plots for the adsorption of RB5 onto activated carbon at temperatures of 25 and 45 °C.

It is evident from the above figure that the plots are not linear, *i.e.* that they exhibit multi-linearity with several sections. It can thus be concluded that intraparticle diffusion is not the only process that influences the adsorption rate and that multiple steps took place during the adsorption process. Few stages can be distinguished during the dye adsorption. The adsorption rate is initially higher and corresponds to instantaneous adsorption, probably due to an electrostatic attraction between the dye and the external surface of the adsorbent. The amount of adsorbed substance on the adsorbent and diffusion decreases over time, and represents a gradual adsorption stage where diffusion rates decreased by increasing the contact time. This process usually includes the intraparticle diffusion of the molecules through the pores of the adsorbent. That stage is followed by the equilibrium stage when dye molecules occupy all active sites of the adsorbent [19]. Diffusion in the pores of the adsorbent is usually determined by the fact that there are several different pore sizes in the adsorbent, and that controlling regions correspond to the dye diffusion to the activated carbon pores of different dimensions. Since the dye molecules diffuse into the inner structure of the adsorbents, the pores for diffusion become smaller and thus the free path of the molecules in the pore decreases.

3.3 Thermodynamics

Standard Gibbs free energy (ΔG^0, kJ/mol) values of the adsorption process can be calculated using the equation:

$$\Delta G^0 = -RT \ln (K_c) \quad (9),$$

Table 3: Standard Gibbs free energy changes (ΔG^0, kJ/mol) for the adsorption of Reactive Black 5 on activated carbon

c_0 (mg/dm³)	T (K)	c_e (mg/dm³)	K_c	ΔG^0 (kJ/mol)
300	298	3.7	80.1	−10.86
	318	4.0	74.0	−11.38
500	298	9.2	53.3	−9.86
	318	2.8	177.6	−13.70
700	298	9.6	71.9	−10.60
	318	5.8	119.7	−12.66

where R represents the universal gas constant and T represents temperature. K_c represents the equilibrium constant calculated from the concentration of the dye adsorbed on the solid at equilibrium (c_s / mg/dm^3) and the concentration of the dye when equilibrium is reached in the liquid phase (c_e / mg/dm^3) [23]:

$$K_c = \frac{c_s}{c_e} \quad (10).$$

The negative values of ΔG^0 indicate that the adsorption reaction is spontaneous. Thus, ΔG^0 values given in Table 3 reflect the feasibility of the process, and that the adsorption of RB5 onto activated carbon was a spontaneous process in nature, in which no energy input from outside of the system was required. The higher negative value reflects a more energetically favourable adsorption. It can thus be concluded that adsorption at 45 °C is energetically more favourable than at 25 °C.

3.4 Morphological analysis of the adsorbent and dye-adsorbent samples

In order to perform a morphological analysis of activated carbon before and after adsorption, photographs were taken using scanning electron microscopy (SEM). It is evident from recorded photographs of activated carbon that the particles differ morphologically and have different pore sizes, as assumed by the results of the intraparticle diffusion model (Figure 7).

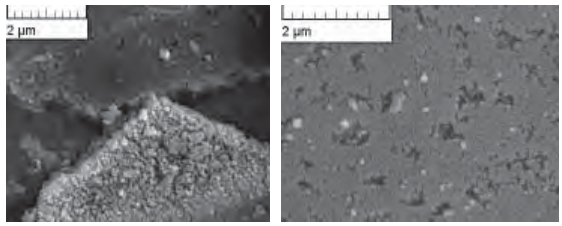

(a) *(b)*

Figure 7: SEM images of activated carbon surface enlarged (a) 15000 x and (b) 20000 x

Figure 8 shows the appearance of activated carbon after the adsorption of RB 5 (adsorption time of 4 hours at a temperature 45 °C) for initial dye concentrations of c_0 = 300 mg/dm^3 (Figure 8a) and c_0 = 700 mg/dm^3 (Figure 8b). It is evident from the images that dye is adsorbed on the surface of activated carbon. For the initial concentration c_0 = 300 mg/dm^3, some parts of the surface are almost completely straight, while the other parts are uneven. The activated carbon surface for the initial dye concentration of c_0 = 700 mg/dm^3 is flatter on most parts, an indication that activated carbon is almost completely covered with dye molecules. From this it can be assumed that, for a higher initial concentration, a certain amount of dye is further adsorbed on activated carbon.

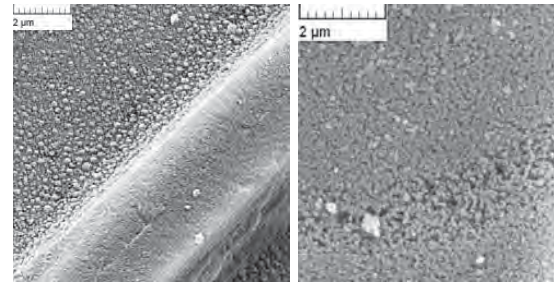

(a) *(b)*

Figure 8: SEM images of activated carbon after the adsorption of dye enlarged 15000 x for initial dye concentrations of (a) c_0 = 300 mg/dm^3, and (b) c_0 = 700 mg/dm^3

4 Conclusion

According to the results achieved, the adsorption of Reactive Black 5 onto activated carbon was very fast. This study also confirmed that activated carbon is a very efficient adsorbent and that adsorption at higher temperature is greater. For all initial concentrations, approximately 90% of RB5 was adsorbed at 25 °C after 1 to 6 hours. On the other hand, these times are significantly shorter at a temperature of 45 °C, with the maximum value of 2 hours for the initial concentration of c_0 = 700 mg/dm^3. Furthermore, the adsorption of RB5 dye on commercial activated carbon was kinetically controlled assuming a pseudo-second-order rather than a pseudo-first-order process. This study also revealed that intraparticle diffusion was not the only process that influenced the adsorption rate and that multiple steps took place during the adsorption process. Finally, the negative values of ΔG^0 indicate that the adsorption reaction was spontaneous in nature and that adsorption at 45 °C was energetically more favourable than at 25 °C. The adsorption of Reactive Black 5 dye on activated carbon was also confirmed by scanning electron microscopy.

Acknowledgements

Authors would like to thank Zorana Kovačević from Faculty of Textile Technology for SEM images recording.

References

1. SAVIN, Irina-Isabella, BUTNARU, Romen. Wastewater characteristics in textile finishing mills. *Environmental Engineering and Management Journal*, 2008, **7**(6), 859–864, doi: 10.30638/eemj.2008.113.
2. BISSCHOPS, I., SPANJERS H. Literature review on textile wastewater characterisation. *Environmental Technology*, 2003, **24**(3), 1399–1411, doi: 10.1080/09593330309385684.
3. EJDER-KORUCU, Mehtap, GÜRSES, Ahmet, DOĞAR, Çetin, SHARMA, Sanjay K., AÇIKYILDIZ, Metin. Removal of organic dyes from industrial Effluents : an overview of physical and biotechnological applications. In *Green chemistry for dyes removal from waste water: research trends and applications*. Edited by S. K. Sharma. New Jersey : John Wiley & Sons, 2015, 1–34.
4. Confidence in textiles. Limit values and fastness [online]. OEKO-TEX® [accessed 28. 2. 2019]. Available on World Wide Web: <www.oeko-tex.com/en/business/certifications_and_services/ots_100/ots_100_limit_values/ots_100_limit_values.xhtml>.
5. VERMA, Akshaya Kumar, DASH, Rajesh Roshan, BHUNIA, Puspendu. Review on chemical coagulation/flocculation technologies for removal of colour from textile wastewaters. *Journal of Environmental Management*, 2012, **93**(1), 154–168, doi: 10.1016/j.jenvman.2011.09.012.
6. HOLKAR, Chandrakant R., JADHAV, Ananda J., PINJARI, Dipak V., MAHAMUNI, Naresh M. and PANDIT, Aniruddha B. A critical review on textile wastewater treatments: Possible approaches. *Journal of Environmental Management*, 2016, **182**, 351–366, doi:10.1016/j.jenvman.2016.07.090.
7. DEPCI, Tolga, ÇELIK, Mehmet S. Dye adsorption on expanding three-layer clays. *In Green chemistry for dyes removal from waste water: research trends and applications*. Edited by S. K. Sharma. New Jersey : John Wiley & Sons, 2015, 331–358.
8. TCHOBANOGLOUS, George et al., *Wastewater engineering : treatment and resource recovery*. Vol. 2. 5th ed. New York : McGraw-Hill Education, 2014, 1224–1245.
9. ALI, Imran. New generation adsorbents for water treatment. *Chemical Reviews*, 2012, **112**(10), 5073–5091, doi: 10.1021/cr300133d.
10. AHMAD, A.A., HAMEED, B.H. Fixed-bed adsorption of reactive azo dye onto granular activated carbon prepared from waste. *Journal of Hazardous Materials*, 2010, **175**(1–3), 298–303, doi: 10.1016/j.jhazmat.2009.10.003.
11. MACHADO, Fernando M., BERGMANN, Carlos P., FERNANDES, Thais H. M., LIMA, Eder C., ROYER, Betina, CALVETE, Tatiana, FAGAN, Solange B. Adsorption of Reactive Red M-2BE dye from water solutions by multi-walled carbon nanotubes and activated carbon. *Journal of Hazardous Materials*, 2011, **192**(3), 1122–1131, doi: 10.1016/j.jhazmat.2011.06.020.
12. SULAYMON, Abbas H., ABOOD, Waleed M. Removal of reactive yellow dye by adsorption onto activated carbon using simulated wastewater. *Desalination and Water Treatment*, 2014, **52**(16–18), 3421–3431, doi: 10.1080/19443994.2013.800341.
13. SULAYMON, Abbas H., ABOOD, Waleed M. Equilibrium and kinetic study of the adsorption of reactive blue, red, and yellow dyes onto activated carbon and barley husk. *Desalination and Water Treatment*, 2014, **52**(28–30), 5485–5493, doi: 10.1080/19443994.2013.814374.
14. GIANNAKOUDAKIS, Dimitrios A., KYZAS, George Z., AVRANAS, Antonis, LAZARIDIS, Nikolaos K. Multi-parametric adsorption effects of the reactive dye removal with commercial activated carbons. *Journal of Molecular Liquids*, 2016, **213**, 381–389, doi: 10.1016/j.molliq.2015.07.010.
15. SILVA, Taís L., RONIX, Amanda, PEZOTI, Osvaldo, SOUZA, Lucas S., LEANDRO, Patricia K. T., BEDIN, Karen C., BELTRAME, Karla K., CAZETTA, André L., ALMEIDA, Vitor C. Mesoporous activated carbon from industrial laundry sewage sludge : adsorption studies of reactive dye Remazol Brilliant Blue R. *Chemical Engineering Journal*, 2016, **303**, 467–476, doi: 10.1016/j.cej.2016.06.009.
16. LAGERGREN, Sten Y. Zur Theorie der Sogenannten Adsorption Geloster Stoffe. Kungliga Sevenska Vetenskapsakademiens, Handlingar, 1898, **24**, 1–39.

17. HO, Y. S., MCKAY G. Pseudo-second order model for sorption processes. *Process Biochemistry*, 1999, **34**(5), 451–465, doi: 10.1016/S0032-9592(98)00112-5.
18. HO, Y. S., MCKAY G. The kinetics of sorption of divalent metal ions onto sphagnum moss peat. *Water Research*, 2000, **34**(3), 735–742, doi: 10.1016/S0043-1354(99)00232-8.
19. DULMAN, Viorica, CUCU-MAN, Simona Maria. Sorption of some textile dyes by beech wood sawdust. *Journal of Hazardous Materials*, 2009, **162**(2–3), 1457–1464, doi: 10.1016/j.jhazmat.2008.06.046.
20. IP, Alvin W. M., BARFORD, John P., MCKAY Gordon. A comparative study on the kinetics and mechanisms of removal of Reactive Black 5 by adsorption onto activated carbons and bone char. *Chemical Engineering Journal*, 2010, **157**(2−3), 434–442, doi: 10.1016/j.cej. 2009. 12.003.
21. BACCAR, R., BLÁNQUEZ, P., BOUZID, J., FEKI, M., SARRÀ, M. Equilibrium, thermodynamic and kinetic studies on adsorption of commercial dye by activated carbon derived from olive-waste cakes. *Chemical Engineering Journal*, 2010, **165**(2), 457–464, doi: 10.1016/j.cej.2010.09.033.
22. ALLEN S. J., MCKAY G., KHADER K. Y. H. Intraparticle diffusion of a basic dye during adsorption onto sphagnum peat. *Environmental Pollution*, 1989, **56**(1), 39–50, doi: 10.1016/0269-7491(89)90120-6.
23. TRAVLOU Nikolina A., KYZAS George Z., LAZARIDIS Nikolaos K., DELIYANNI Eleni A. Graphite oxide/chitosan composite for reactive dye removal. *Chemical Engineering Journal*, 2013, **217**, 256–265, doi: 10.1016/j.cej. 2012. 12.008.

SHORT INSTRUCTIONS FOR AUTHORS OF SCIENTIFIC ARTICLES

Scientific articles categories:

- **Original scientific article** is the first publication of original research results in such a form that the research can be repeated and conclusions verified. Scientific information must be demonstrated in such a way that the results are obtained with the same accuracy or within the limits of experimental errors as stated by the author, and that the accuracy of analyses the results are based on can be verified. An original scientific article is designed according to the IMRAD scheme (Introduction, Methods, Results and Discussion) for experimental research or in a descriptive way for descriptive scientific fields, where observations are given in a simple chronological order.
- **Review article** presents an overview of most recent works in a specific field with the purpose of summarizing, analysing, evaluating or synthesizing information that has already been published. This type of article brings new syntheses, new ideas and theories, and even new scientific examples. No scheme is prescribed for review article.
- **Short scientific article** is original scientific article where some elements of the IMRAD scheme have been omitted. It is a short report about finished original scientific work or work which is still in progress. Letters to the editor of scientific journals and short scientific notes are included in this category as well.

Language: The manuscript of submitted articles should be written in UK English and it is the authors responsibility to ensure the quality of the language.

Manuscript length: The manuscript should not exceed 30,000 characters without spacing.

Article submission: The texts should be submitted only in their electronic form in the format *.doc (or *docx) and in the format *.pdf (made in the computer program Adobe Acrobat) to the address: tekstilec@a.ntf.uni-lj.si. The name of the document should contain the date (year-month-day) and the surname of the corresponding author, e.g. 20140125Novak.docx. The articles proposed for a review need to have their figures and tables included in the text. The article can also be submitted through a cloud-based file transfer service, e.g. "WeTransfer" (www.wetransfer.com).

Publication requirements: All submitted articles are professionally, terminologically and editorially reviewed in accordance with the general professional and journalistic standards of the journal Tekstilec. Articles are reviewed by one or more reviewers and are accepted for publication on the basis of a positive review. If reviewers are not unanimous, the editorial board decides on further proceedings. The authors can propose to the editorial board the names of reviewers, whereas the editorial board then accepts or rejects the proposal. The reviewers' comments are sent to authors for them to complete and correct their manuscripts. The author is held fully responsible for the content of their work. Before the author sends their work for publication, they need to settle the issue on the content publication in line with the rules of the business or institution, respectively, they work at. When submitting the article, the authors have to fill in and sign the Copyright Statement (www.tekstilec.si), and send a copy to the editors by e-mail. They should keep the original for their own personal reference. The author commits themselves in the Copyright Statement that the manuscript they are submitting for publication in Tekstilec was not sent to any other journal for publication. When the work is going to be published depends on whether the manuscript meets the publication requirements and on the time reference the author is going to return the required changes or corrections to the editors.

Copyright corrections: The editors are going to send computer printouts for proofreading and correcting. It is the author's responsibility to proofread the article and send corrections as soon as possible. However, no greater changes or amendments to the text are allowed at this point.

Colour print: Colour print is performed only when this is necessary from the viewpoint of information comprehension, and upon agreement with the author and the editorial board.

More information on: www.tekstilec.si